University of Alberta

Forging a New Chemical Bond: Theory and Experiment

Studies of the

Metal-Alkyne Interaction in $M(CO)_x(\eta^2$-alkyne) (M = Ru, Os, W) Compounds

and

Isotope Effects in Olefin Addition Reactions

by

Joanne L. Gainsforth

©

A thesis submitted to the Faculty of Graduate Studies and Research
in partial fulfillment of the requirements for the degree of Master of Science

Department of Chemistry

Edmonton, Alberta

Fall 1998

National Library of Canada
Acquisitions and Bibliographic Services
395 Wellington Street
Ottawa ON K1A 0N4
Canada

Bibliothèque nationale du Canada
Acquisitions et services bibliographiques
395, rue Wellington
Ottawa ON K1A 0N4
Canada

Your file Votre référence

Our file Notre référence

The author has granted a non-exclusive licence allowing the National Library of Canada to reproduce, loan, distribute or sell copies of this thesis in microform, paper or electronic formats.

The author retains ownership of the copyright in this thesis. Neither the thesis nor substantial extracts from it may be printed or otherwise reproduced without the author's permission.

L'auteur a accordé une licence non exclusive permettant à la Bibliothèque nationale du Canada de reproduire, prêter, distribuer ou vendre des copies de cette thèse sous la forme de microfiche/film, de reproduction sur papier ou sur format électronique.

L'auteur conserve la propriété du droit d'auteur qui protège cette thèse. Ni la thèse ni des extraits substantiels de celle-ci ne doivent être imprimés ou autrement reproduits sans son autorisation.

0-612-34364-2

Canada

University of Alberta

Library Release Form

Name of Author: Joanne L. Gainsforth

Title of Thesis: Forging a New Chemical Bond: Theory and Experiment. Studies of the Metal-Alkyne Interaction in $M(CO)_x(\eta^2$-alkyne) (M = Ru, Os, W) Compounds and Isotope Effects in Olefin Addition Reactions

Degree: Master of Science

Year this Degree Granted: 1998

Permission is hereby granted to the University of Alberta Library to reproduce single copies of this thesis and to lend or sell such copies for private, scholarly, or scientific research purposes only.

The author reserves all other publication and other rights in association with the copyright in the thesis, and except as hereinbefore provided, neither the thesis nor any substantial portion thereof may be printed or otherwise reproduced in any material form whatever without the author's prior written permission.

Joanne Gainsforth

Joanne L. Gainsforth

P. O. Box 484 Station Main
Lloydminster, Saskatchewan
S9V 0Y6

Date: September 15, 1998.

University of Alberta

Faculty of Graduate Studies and Research

The undersigned certify that they have read, and recommend to the Faculty of Graduate Studies and Research for acceptance, a thesis entitled **Forging a New Chemical Bond: Theory and Experiment. Study of the Metal-Alkyne Interaction in $M(CO)_x(\eta^2$-alkyne) (M = Ru, Os, W) Compounds and Investigation of the Isotope Effects in Olefin Addition Reactions** submitted by Joanne L. Gainsforth in partial fulfillment of the requirements for the degree of Master of Science.

M. Klobukowski (co-supervisor)

J. Takats (co-supervisor)

R. B. Jordan

S. Kresta

Date: August 27, 1998

Abstract

The alkyne ligand in group 8 $M(CO)_4(\eta^2\text{-alkyne})$ complexes has a labilizing effect on CO which has been attributed to the alkyne's ability to act as a four electron donor. This attribute of the alkyne is shown to extend to the group six transition metals in a phosphine substitution study of $W(CO)_5$(BTMSA). Molecular orbital pictures show four electron donation from the alkyne ligand upon CO dissociation in both [$Os(CO)_3$(BTMSA)] and [$W(CO)_5$(BTMSA)].

The $M(CO)_4$(alkyne) (M = Fe, Ru, Os) compounds react with saturated 18e$^-$ metal complexes forming bimetallacyclic products. A kinetic study of the reaction of $Ru(CO)_4$(HFB) with $Os(CO)_5$ and $Cp^*M(CO)_2$ (M = Rh, Ir) was carried out. The three reactions yield analogous products, however, rhodium reacts much faster than iridium, which is faster than osmium. It is suggested that $Cp^*Rh(CO)_2$ does not react in a manner similar to $Cp^*Ir(CO)_2$ and $Os(CO)_5$.

Isotope effects for the addition of bromine to cyclohexene and the addition of bromine, sulfur and selenium to ethylene were calculated with Density Functional Theory. The origin of the isotope effects, which could not be resolved by experiment alone, was determined for the ethylene additions.

Acknowledgements

This work was accomplished with the support of many people: a testament to their dedication and areas of expertise.

I am grateful for the opportunity to work under the tutelage of my supervisors Dr. Mariusz Klobukowski and Dr. Josef Takats. Their guidance and support were surpassed only by their friendship, which I will always cherish.

I have enjoyed getting to know and working with the following people: Stephen Decker, Dr. Jason Cooke, Dr. John Washington, Quinn Major, Dr. Guanyang Lin, Dr. Greg Ferrance, and Martin Morissette. Their help, experience, and, most of all, their patience has taught me a great deal and has been greatly appreciated.

Dr. Bob Jordan has given me extensive help and guidance on the $Ru(CO)_4(HFB)$ kinetic work that was carried out, which is gratefully acknowledged. Dr. Margaret Sisley and the other members of Dr. Jordan's group have graciously shared their computer, allowing me to analyze my kinetic data.

I would like to thank the staff of the NMR facility for collecting all of my NMR spectra and taking the time to answer my questions. I am also grateful for all of the work the third floor glass blowers did fixing all of the glassware that I managed to damage or destroy.

My family's support and understanding has been unwavering throughout my education and will not be forgotten. My sister Carin's help has been appreciated and I have enjoyed being roommates with her these past few years.

Finally, I would like to give special thanks to my husband, Boomer, for his encouragement, love, and understanding, all of which have helped me realize this goal.

Table of Contents

Chapter One Introduction

1.1 Chemistry of Transition Metal Alkyne-Carbonyl Complexes 1

1.1.1 Historical Overview 1

1.1.2 Reactivity of $M(CO)_4(\eta^2$-alkyne) Complexes 5

1.1.3 Bonding in $M(CO)_4$(alkyne) and $M(CO)_5$(alkyne) Complexes 6

1.2 Theoretical Studies of Chemical Systems 9

1.2.1 Density Functional Theory 9

1.2.2 Calculations using Statistical Mechanics 17

1.2.3 Equilibrium Constant 19

1.2.4 Rate Constant 21

1.2.5 Isotope Effects 23

1.3 Scope of the Thesis 26

1.4 References 28

Chapter Two Synthesis and Phosphine Substitution of $M(CO)_x$(BTMSA) Compounds (M = Os, x = 4; M = W, x = 5)

2.1 Introduction 31

2.2 Results 32

2.2.1 Attempted Preparation of $W(CO)_5(\eta^2$-$RC_2R)$ (R = H, CH_3, CF_3, CH_2CH_3) 32

2.2.2 Reactions of $Os(CO)_4$(BTMSA) (**1**) with PMe_3 34

2.2.3 Reactions of $W(CO)_5$(BTMSA) (**3**) with PMe_3 36

2.3 Discussion 39

2.4 Conclusions 41

2.5 Experimental Section 41

2.5.1 Solvents and General Techniques 41

2.5.2 Physical Measurements 42

2.5.3 Photochemical Techniques 42
2.5.4 Starting Materials and Reagents 42
2.5.5 Synthetic Procedures 43
2.6 References 46

Chapter Three Theoretical Investigation of the Metal-Alkyne Interaction in $Os(CO)_x(C_2R_2)$ (x = 3,4) and $W(CO)_x(C_2R_2)$ (x = 4,5) Complexes

3.1 Introduction 47
3.2 Computational Details 48
3.3 Results and Discussion 48
3.3.1 Free Alkynes 48
3.3.2 Parent Carbonyls 50
3.3.3 Metal-Alkyne Complexes 50
3.3.4 Molecular Orbitals 54
3.3.5 Fragment Molecular Orbital Analysis 62
3.3.6 Energies Calculated for Alkyne Addition and CO Dissociation in the Metal-Carbonyl Complexes 62
3.4 Conclusions 66
3.5 References 68
3.6 Appendix: Calculated Structural Parameters 70

Chapter Four Mechanistic Insight into the Condensation Reactions of $Ru(CO)_4$(HFB) with Saturated 18 – electron Species

4.1 Introduction 72
4.2 Results 73
4.2.1 Kinetic Model 73
4.2.2 Rate Law 76
4.2.3 Treatment of Data 78

4.2.3.1 CO Dissociation From $Ru(CO)_4$(HFB) in Pentane 79
4.2.3.2 Initial Concentrations of Reactants 81
4.2.3.3 Kinetic Parameters: Values of the Ratio 82
4.3 Discussion 86
4.5 Conclusions 88
4.6 Experimental 88
4.6.1 Solvents and General Techniques 88
4.6.2 Kinetic Measurements 89
4.6.3 Starting Materials and Reagents 89
4.6.4 Kinetic Procedure 90
4.7 References 91

Chapter Five Computational Study of the Reaction of $Ru(CO)_4$(HFB) with $Os(CO)_5$

5.1 Introduction 92
5.2 Results and Discussion 92
5.2.1 Methodology 92
5.2.2 CO Dissociation From $Ru(CO)_4$(HFB) 96
5.2.3 Reaction of $Ru(CO)_4$(HFB) with $Os(CO)_5$ 102
5.3 Conclusions 109
5.4 References 110

Chapter Six Isotope Effects in the Electrophilic Bromination of Cyclohexene

6.1 Introduction 112
6.2 Computational Details 114
6.3 Development of the System to be Studied Computationally 115
6.4 Results 116
6.5 Models of the Origin of Isotope Effects 124
6.6 Conclusions 125

6.7 References 126
6.8 Appendix: Calculated Structural Parameters 128

Chapter Seven Isotope Effects in the Electrophilic Bromination of Ethylene
7.1 Introduction 131
7.2 Computational Methods 131
7.2.1 Methodological Details 131
7.2.2 System Studied 132
7.3 Results and Discussion 134
7.4 Conclusions 141
7.5 References 143

Chapter Eight Isotope Effects in the Addition of Sulfur and Selenium to Ethylene
8.1 Introduction 145
8.2 Computational Details 146
8.3 Results and Discussion 147
8.4 Conclusions 157
8.5 References 159
8.6 Appendix: Complete Basis Set Results 161

Chapter Nine Conclusions
9.1 Metal-Alkyne Chemistry 164
9.2 Isotope Effects 165
9.3 References 167

List of Tables

Table 2-1 Characteristic IR Bands for $W(CO)(alkyne)_3$ Complexes 32

Table 3-1 Polarization Functions Used in the Basis Sets 48
Table 3-2 Bond Lengths (Å) and Angles (°) in the Free Alkynes 49
Table 3-3 Parent Carbonyl Bond Lengths (Å) 50
Table 3-4 Calculated C≡C and M-C Bond Lengths (Å) in the Osmium-Alkyne Complexes 51
Table 3-5 Calculated C≡C and M-C Bond Lengths (Å) in the Tungsten-Alkyne Complexes 52
Table 3-6 M-CO Bond Lengths (Å) in the Metal-Alkyne Complexes 53
Table 3-7 CO Bond Lengths (Å) in the Metal-Alkyne Complexes 54
Table 3-8 $Os(CO)_4$(BTMSA) Calculated and Experimental Geometry 55
Table 3-9 $W(CO)_5$(BTMSA) Calculated and Experimental Geometry 56
Table 3-10 Energetics Calculated for the Reaction Shown in Eq. (3-1) 62
Table 3-11 Energetics Calculated for the Reaction Shown in Eq. (3-2) 65
Table 3-12 Energetics Calculated for the Reaction Shown in Eq. (3-3) 65
Table 3-13 Energetics Calculated for the Reaction Shown in Eq. (3-4) 65
Table 3-A1 Calculated Geometry of $Os(CO)_4$(alkyne) (D1 basis set) 70
Table 3-A2 Calculated Geometry of $Os(CO)_3$(alkyne) (D1 basis set) 70
Table 3-A3 Calculated Geometry of $W(CO)_5$(alkyne) (D1 basis set) 71
Table 3-A4 Calculated Geometry of $W(CO)_4$(alkyne) (D1 basis set) 71

Table 4-1 CO Bands Monitored in the Kinetic Study of the $Ru(CO)_4$(HFB) Condensation Reactions 74
Table 4-2 Kinetic Results for PPh_3 Substitution in $Ru(CO)_4$(HFB) in Pentane 81

Table 4-3 Rates of CO Dissociation From $Ru(CO)_4(HFB)$ in Pentane and CH_2Cl_2 81
Table 4-4 Kinetic Results for the Reaction of $Ru(CO)_4(HFB)$ with $Os(CO)_5$ 83
Table 4-5 Effect of Dead Time, t_o, on Ratio 83
Table 4-6 Kinetic Results for the Reaction of $Ru(CO)_4(HFB)$ with $Cp^*Ir(CO)_2$ 83
Table 4-7 Kinetic Results for the Reaction of $Ru(CO)_4(HFB)$ with $Cp^*Rh(CO)_2$ 85
Table 4-8 Effect of Temperature on Ratio 85

Table 5-1 Basis Set Breakdown 93
Table 5-2 Structural Parameters for $Ru(CO)_4(HFB)$ 94
Table 5-3 Comparison between DFT and HF on $Ru(CO)_4(HFB)$ 95
Table 5-4 Selected Vibrational Modes for $Ru(CO)_4(HFB)$ (cm^{-1}) 96
Table 5-5 Comparison of Structural Parameters for $Ru(CO)_4(HFB)$ and $Ru(CO)_3(HFB)$ 99
Table 5-6 CO Dissociation Energies from $Ru(CO)_4(HFB)$ (kcal/mol) 102
Table 5-7 Bond Lengths (Å) and CO Stretching Frequencies (cm^{-1}) in $Os(CO)_5$ 104
Table 5-8 Structure and Characteristic IR Bands of $RuOs(CO)_8(HFB)$ 106

Table 6-1 Relative Energies (kcal/mol) of the Conformers 116
Table 6-2 Geometry of the Conformers Calculated Using B3LYP 118
Table 6-3 Comparison of Experimental and Calculated Geometry for the Twist Conformer of Cyclohexene 119
Table 6-4 Vibrational Assignment of Cyclohexene's Twist Conformer (cm^{-1}) 120
Table 6-5 Calculated EIE (K_D/K_H) for the Bromination of Cyclohexene 121

Table 6-6 Bending and Stretching Contributions to the BP86 Calculated EIE 123
Table 6-7 Analysis of the BP86 Calculated Stretching Modes (cm^{-1}) in the D_8 Isotopomer 124
Table 6-A1 Structural Parameters for Twist Cyclohexene 128
Table 6-A2 Structural Parameters for Boat Cyclohexene 128
Table 6-A3 Structural Parameters for Twist Cyclohexenyl Bromonium Ion 129
Table 6-A4 Structural Parameters for Boat-down Cyclohexenyl Bromonium Ion 129
Table 6-A5 Structural Parameters for Boat-up Cyclohexenyl Bromonium Ion 130

Table 7-1 Geometry of Ethylene and the Ethylene Bromonium Ion 135
Table 7-2 Assignment of the Harmonic Vibrational Modes of Ethylene 135
Table 7-3 Contributions to the Per-Site Secondary Isotope Effects 137
Table 7-4 Mapping of Calculated Harmonic Frequencies for Ethylene (D_{2h} symmetry) and the Ethylene Bromonium Ion (C_{2v} symmetry) 138
Table 7-5 Contributions of Various Modes to η_{vib} and ζ_{vib} 139
Table 7-6 Bond Lengths (Å) in the CTC 141
Table 7-7 Assignment of Harmonic Vibrational Modes for the CTC (cm^{-1}) 142

Table 8-1 Ethylene Geometry 148
Table 8-2 Thiirane and Selenirane Geometry 149
Table 8-3 Calculated Transition State Geometry 149
Table 8-4 IR Frequencies (in cm^{-1}) of Ethylene 150
Table 8-5 IR Frequencies (in cm^{-1}) of Thiirane and Selenirane 151
Table 8-6 Contributions to the Per-Site Isotope Effect 152
Table 8-7 Mode Mapping for Sulfur Addition to Ethylene (B3PW91/Basis 1 Calculation) 154

Table 8-8 Mode Mapping for Selenium Addition to Ethylene (B3PW91/Basis 2 Calculation) 154
Table 8-9 Individual Mode Contributions for Sulfur Addition to Ethylene (B3PW91/Basis 1) 155
Table 8-10 Individual Mode Contributions for Selenium Addition to Ethylene (B3PW91/Basis 2) 156
Table 8-A1 Thiirane Geometry 161
Table 8-A2 Sulfur Transition State Geometry 161
Table 8-A3 IR Frequencies (in cm^{-1}) of Ethylene 162
Table 8-A4 IR Frequencies (in cm^{-1}) of Thiirane 162
Table 8-A5 Calculated Frequencies (in cm^{-1}) of the C_2H_4 + S Transition State 163

List of Figures

Figure 1-1 X-ray Crystal Structure of $Fe_2(CO)_8(Ph_2PC{\equiv}C^tBu)$ 2

Figure 1-2 Components of the Metal-Alkyne Bond Involving the $\pi_{\parallel}$ Orbital 8

Figure 1-3 Metal-Alkyne Bonding Components Involving the $\pi_{\perp}$ Orbital 9

Figure 1-4 Group 6 and Group 8 Metal-Alkyne Interaction Diagram 10

Figure 1-5 Energy Level Diagram for R⇌P 20

Figure 1-6 Potential Energy Change Along the Reaction Coordinate for R⇌P 22

Figure 1-7 Potential Energy Change Along the Reaction Coordinate for R⇌A 22

Figure 2-1 Geometrical Isomers of $W(CO)_4(PMe_3)$(BTMSA) 37

Figure 2-2 Pathway for the First Phosphine Substitution in $W(CO)_5$(BTMSA) .. 40

Figure 2-3 Pathway for the Second Phosphine Substitution in $W(CO)_5$(BTMSA) 40

Figure 3-1 Bond Definitions for the Metal-Alkyne Species 52

Figure 3-2 Molecular Orbitals of $Os(CO)_5$(BTMSA) and $W(CO)_5$(BTMSA); Donation From Filled Alkyne π Sets 57

Figure 3-3 Molecular Orbitals of $Os(CO)_4$(BTMSA) and $W(CO)_5$(BTMSA); Back Donation From Filled M d_{π} 58

Figure 3-4 Molecular Orbitals of $Os(CO)_3$(BTMSA) and $W(CO)_4$(BTMSA); Donation From Filled Alkyne π Sets 59

Figure 3-5 Molecular Orbitals of $Os(CO)_3$(BTMSA) and $W(CO)_4$(BTMSA); Back Donation From Filled M d_{π} 60

Figure 3-6 Calculated Geometries of $W(CO)_5$(BTMSA) and $W(CO)_4$(BTMSA) 61
Figure 3-7 Calculated Geometries of $Os(CO)_4$(BTMSA) and $Os(CO)_3$(BTMSA) 61
Figure 3-8 Molecular Orbital Interaction Diagram for HFB 63
Figure 3-9 Molecular Orbital Interaction Diagram for BTMSA 64

Figure 4-1 Representative IR Spectra for the Reaction of $Ru(CO)_4$(HFB) ($6.89x10^{-4}$ M) with $Os(CO)_5$ ($9.41x10^{-3}$ M) in Pentane at 22.6 °C 74
Figure 4-2 Absorbance Time Curves for the Reaction of $Ru(CO)_4$(HFB) with $Os(CO)_5$ 75

Figure 5-1 Vibrational Modes of $Ru(CO)_4$(HFB) 97
Figure 5-2 Optimized Geometry of $Ru(CO)_4$(HFB) and $Ru(CO)_3$(HFB) 98
Figure 5-3 Molecular Orbitals for $Ru(CO)_4$(HFB) 100
Figure 5-4 Molecular Orbitals for $Ru(CO)_3$(HFB) 101
Figure 5-5 Nature of the Calculated and Experimental M-CO Dissociation Energies 103
Figure 5-6 Vibrational Modes of $Os(CO)_5$ 105
Figure 5-7 Initial Structure of the Proposed Intermediate $[(CO)_3Ru(HFB)(\mu\text{-}CO)Os(CO)_4]$ 107
Figure 5-8 Vibrational Modes of $RuOs(CO)_8$(HFB) 108

Figure 6-1 Labeling of Cyclohexene 113
Figure 6-2 Structures of the Cyclohexene and Cyclohexenyl Bromonium Ion Conformations 117

Figure 6-3 Calculated (unscaled BP86) and Experimental (neat) IR Spectra of Cyclohexene 119

Figure 7-1 Transition State for the Bromination of Ethylene 132

Figure 7-2 Schematic of a Late Transition State (TS ≈ P) 133

Figure 7-3 Vibrational Mode 15: CH_2 Symmetric Twist 140

List of Schemes

Scheme 1-1 Representative Condensation Reactions of $Os(CO)_4(HC{\equiv}CH)$ 7

Scheme 1-2 Representative Condensation Reactions of $Fe(CO)_4(RC{\equiv}CR)$ 7

Scheme 3-1 Alkynes and Transition Metal Complexes Studied 47

Scheme 4-1 Decomposition of $Ru(CO)_5$ 73

Scheme 4-2 Proposed Mechanism for the Condensation Reactions 76

Scheme 4-3 Phosphine Substitution Mechanism for $Ru(CO)_4(HFB)$ 79

Scheme 4-4 Intermetallic Exchange of ^{13}CO in the Reaction of $Ru(^{13}CO)_4(HFB)$ with $Os(CO)_5$ 87

Scheme 5-1 Reaction of $Ru(CO)_4(HFB)$ with $Os(CO)_5$ 103

Scheme 6-1 Isotopomers of Cyclohexene 121

Scheme 7-1 Deuterated Ethylenes 136

List of Abbreviations

Å	Angström(s)
Anal.	analysis
asym	asymmetric
br	broad
BSA	bis(silyl)acetylene, $C_2(SiH_3)_2$
BTMSA	bis(trimethylsilyl)acetylene, $C_2(SiMe_3)_2$
Bu	butyl, $CH_3CH_2CH_2CH_2$-
c	speed of light, $3x10^8$ m^2
ca.	circa (approximately)
Calcd	calculated
CDA	Charge Decomposition Analysis
CI	configuration interaction
Cp*	pentamethylcyclopentadienyl, η^5-$C_5(CH_3)_5$
CTC	charge-transfer complex
Cy, c-Hex	cyclohexyl, C_6H_{11}-
d	doublet
δ	ppm
DFT	Density Functional Theory
DPA	diphenylacetylene, C_2Ph_2
DZV	double zeta valence
$D^2/DaÅ^2$	$(debye)^2/dalton(Angström)^2$
e^-	electron
ECP	effective core potential
e.g.	exempli gratia (for example)
EIE	equilibrium isotope effects
eq	equatorial
eq.	equation
equiv.	equivalents

Et	ethyl, CH_3CH_2-
et al.	et alii (and others)
eV	electron volts
GWV	Glasswerk Wertheim
h	Planck's constant
HF	Hartree-Fock
HFB	hexafluorobut-2-yne, $C_2(CF_3)_2$
hν	radiation
Hz	hertz
i	imaginary
i.e.	id est (that is)
^{i}Pr	isopropyl, $(CH_3)_2CH$-
IR	infrared
J	coupling constant
λ	wavelength
K	Kelvin
k_B	Boltzmann's constant
KIE	kinetic isotope effect
m	medium (IR)
m	multiplet (NMR)
M	molar, mol/L
Me	methyl, CH_3-
mg	milligrams
MHz	megahertz
mL	milliliters
MP	Mpller-Plesset
N_A	Avagadro's number
nm	nanometers
NMR	nuclear magnetic resonance

ν	frequency
pet. ether	petroleum ether
Ph	phenyl, C_6H_5-
^{n}Pr	propyl, $CH_3CH_2CH_2$-
Q	partition function
QC/MM MD	quantum chemistry/molecular mechanics molecular dynamics
QZV	quadruple zeta valence
RHF	restricted Hartree-Fock
RT	room temperature
rxn	reaction
s	singlet (NMR)
s	strong (IR)
σ	symmetry number
sym	symmetric
symm	symmetry
SZV	single zeta valence
t	triplet
T	temp
^{t}Bu	tertiary-butyl, $(CH_3)_3C$-
TMS	trimethylsilyl, $Si(CH_3)_3$
TS	transition state
TZV	triple zeta valence
vs	very strong
w	weak
W	watts
WFT	wave-function theory
YAeHMOP	Yet Another extended Hückel Molecular Orbital Program
ZPE	zero-point energy
[X]	concentration of species 'X'

Chapter One

Introduction

1.1 Chemistry of Transition Metal Alkyne-Carbonyl Complexes

1.1.1 Historical Overview

Transition metal carbonyl complexes played a central role in the development of organo-transition metal (organometallic) chemistry. Substitution of carbonyls with different types of ligands separated the field into classes of complexes (e.g. metal alkyne-carbonyls). Further chemical modifications to the complexes (for example, migratory insertion, oxidative addition, reductive elimination) increased the variety of compounds observed and the chemistry being investigated. For the purpose of this thesis, the history of the iron and chromium triad alkyne-carbonyl complexes will be briefly reviewed.

The reaction of alkynes with iron carbonyls was first reported almost 40 years ago[1]. An example of the myriad of compounds that were made is shown in equation (1-1).

$$Fe_2(CO)_9 + DPA \xrightarrow[RT]{\text{pet. ether}} Fe(CO)_5 + (DPA)Fe_3(CO)_9 + (DPA)_2Fe_2(CO)_6 + [(DPA)_2CO]Fe_2(CO)_6 \quad (1\text{-}1)$$

DPA = PhC≡CPh

The most common types of products were dinuclear ferroles (**1**) and mononuclear cyclopentadienone complexes (**2**).

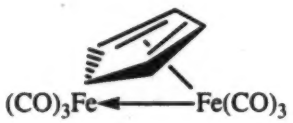

1

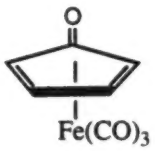

2

It was postulated that alkyne/alkyne and alkyne/CO coupling were mediated by mono-alkyne complexes, $Fe(CO)_4$(alkyne), but such a species, for the most part, remained elusive. However, with the bulky bis(trimethylsilyl)acetylene (BTMSA) ligand, alkyne coupling was not observed[1,2]. The reaction was very clean, producing only $Fe(CO)_4(\eta^2$-BTMSA), one of the much sought-after metal-alkyne complexes. The analogous species was also observed in the reaction with bis(tert-butyl)acetylene[3]. However, $Fe(CO)_4(\eta^2$-$C_2{}^tBu_2)$ was only a minor product, the major being $Fe_2(CO)_6(\mu$-η^2:η^2-$C_2{}^tBu_2)$, and its full characterization has not been reported. Using the unusual alkyne $Ph_2PC{\equiv}C^tBu$, Carty[4] isolated $Fe_2(CO)_8(Ph_2PC{\equiv}C^tBu)$, which contains $Fe(CO)_4(PPh_2R)$ and $Fe(CO)_4$(alkyne) moieties. The solid state structure of the complex, Figure 1-1, showed the expected axial-phosphine and equatorial-alkyne substitution pattern for a five-coordinate trigonal bipyramidal geometry[5]. The crystal parameters showed that

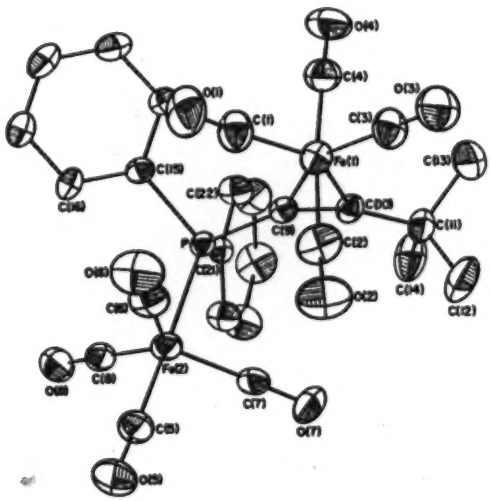

Figure 1-1. X-ray Crystal Structure of $Fe_2(CO)_8(Ph_2PC{\equiv}C^tBu)$[4]

the metal-alkyne bonds were structurally similar to iron-alkene complexes, which have stable metal-olefin interactions. Based on this, Carty concluded that iron-alkyne complexes were "hyper-reactive" towards other alkynes rather than having an unstable metal-alkyne interaction (weak metal-alkyne bonds).

The ability to synthesize group 8 metal alkyne-carbonyl compounds was established in our laboratories first with the isolation of the $M(CO)_4$(BTMSA) (M = Ru, Os) complexes using low temperature photolysis[6] and then with the demonstration that the synthetic method (eq. (1-2))[7,8] was applicable to a variety of alkynes.

$$M(CO)_5 \quad + \quad RC{\equiv}CR \xrightarrow[\text{low temp., alkane}]{h\nu,\ \lambda \geq 370nm} M(CO)_4(\eta^2\text{-}RC{\equiv}CR) \qquad (1\text{-}2)$$
$$\text{- CO}$$

Very recently, this method has been extended to iron[9], requiring only slight modifications: lower temperature and more energetic light (uranium glass cut-off filter) (eq. (1-3)).

$$Fe(CO)_5 \quad + \quad RC{\equiv}CR' \xrightarrow[-70°C < T < -50°C]{h\nu,\ \lambda \geq 330nm,\ \text{pentane}} Fe(CO)_4(\eta^2\text{-}RC{\equiv}CR') \qquad (1\text{-}3)$$
$$\text{- CO}$$

Contrary to the now well-established group 8 $M(CO)_4$(alkyne) complexes, there are only a few scattered reports on the synthesis of group 6 $M(CO)_5$(alkyne) complexes. More than 30 years ago, Stolz[10] observed by IR a variety of photochemically produced metal-alkyne complexes (eq. (1-4)), but they were too unstable to be isolated.

$$M(CO)_6 + RC{\equiv}CR' \xrightarrow{h\nu} M(CO)_5(RC{\equiv}CR') \qquad (1\text{-}4)$$

M = Mo, W

R = H, R' = H, Me

R = Et, R' = Et

In the catalytic polymerization of terminal alkynes with $W(CO)_6$, Geoffroy[11] suggested that polymerization proceeded through a $W(CO)_5$(alkyne) complex which then rearranges to the vinylidene compound, the direct precursor to the catalytically active species (eq. (1-5)).

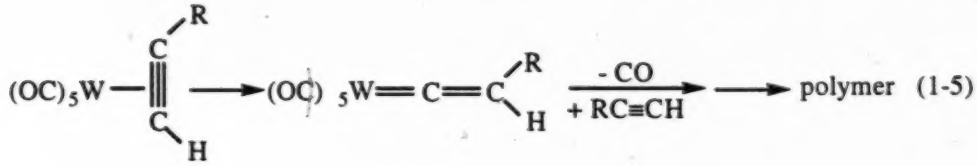

(1-5)

Using low temperature photolysis, Fischer[12] observed a range of terminal alkyne complexes which, upon warming, rearranged to vinylidenes (eq. (1-6)). However, using low temperature chromatography, both $W(CO)_5(HC{\equiv}CPh)$ and

$$W(CO)_6 \xrightarrow[-\,CO]{h\nu/CH_2Cl_2/\,-\,85\,^\circ C} (OC)_5W(CH_2Cl_2) \xrightarrow[+\,HC{\equiv}CR]{-\,85\,^\circ C\ -\,CH_2Cl_2} (OC)_5W(HC{\equiv}CR) \qquad (1\text{-}6)$$

R = Ph, ^{t}Bu, c-Hex, COOMe, $C(=CH_2)Me$, $CH=C(OMe)H$

$W(CO)_5(HC{\equiv}C(COOMe))$ could be isolated in reasonable yields. Besides being able to synthesize these compounds, Fischer also obtained the X-ray crystal structure of $W(CO)_5(HC{\equiv}CPh)$, a major advance in this area.

At about the same time, vinylidene rearrangement with terminal alkynes was also observed in matrix isolation studies[13]. However, rearrangement was not observed with internal alkynes, indicating a possible increased stability. This was substantiated with the room temperature synthesis, isolation and crystal structure determination of $W(CO)_5$(BTMSA)[14].

With these developments, the chemistry of group 6 alkynes is just beginning to emerge and is expected to experience further growth.

1.1.2 Reactivity of $M(CO)_4(\eta^2$-alkyne) Complexes

With respect to the large body of chemistry that had been known, it was of obvious interest to investigate whether the iron triad $M(CO)_4$(alkyne) complexes exhibited unusual reactivity patterns. Indeed, it was discovered very early that the $M(CO)_4$(HFB) (HFB = hexafluorobutyne) complexes underwent ^{13}CO enrichment[7,9], being the most facile with iron. Further investigation with other alkynes showed that CO exchange is a common feature of the $M(CO)_4$(alkyne) species[8]. A study of the CO substitution kinetics[15] established the dissociative nature of the process and provided a quantitative measure of the lability enhancement due to the alkyne ligand; the rate of phosphine substitution increases by 13, 2, and 7 orders of magnitude from $M(CO)_5$ to $M(CO)_4$(HFB) for M = Fe, Ru, and Os, respectively.

Once it was possible to isolate the $Fe(CO)_4$(alkyne) complexes, they were shown to undergo alkyne/CO coupling reactions very readily[9]. This confirmed the earlier idea that the $Fe(CO)_4$(alkyne) species were directly involved in the formation of coupling products. Interestingly, the alkyne coupling reactions were more of a rarity with ruthenium and osmium. Thermally induced coupling has been observed with electron-rich alkynes bearing aliphatic groups, but only cyclopentadienone complexes are formed[16] (eq. (1-7)). The alkyne/CO coupling reactions are initiated by CO insertion into the metal-alkyne bonds. Such species have been observed, in particular, in phosphine substitution reactions of $Os(CO)_4$(alkyne)[17].

$$M(CO)_5 + C_2R_2 \xrightarrow[\text{2. warm to 0 °C}]{\text{1. h}\nu,\ \lambda \geq 370\ \text{nm},\ -60\ °C} (\eta^4\text{-}C_4R_4CO)M(CO)_3 + CO \qquad (1\text{-}7)$$

M = Ru, Os
R = Me, Et, ^{n}Pr

The formally 16e⁻ $M(CO)_3$(alkyne) intermediate is thought to be the reactive species to which phosphine(s) or alkyne(s) are added. Examples of similar species in the literature include $Os(CO)(P^iPr_3)_2(\eta^2\text{-}C_2Ph_2)$[18] and $Fe(CO)_2(PCy_3)(HFB)$[19], the latter more relevant as it differs by only one phosphine ligand from the putative intermediate.

The most unexpected feature of these group 8 metal-alkyne complexes is their reactivity towards other 18e⁻ transition metal species[7,8,20]. This reaction was first discovered with $Ru(CO)_4$(HFB) during its photochemical preparation and was readily extended to other iron triad alkyne-carbonyl species. The condensation reaction produces bimetallacycles, the type of which depends both on the metal and alkyne involved as shown in Schemes 1-1 and 1-2.

1.1.3 Bonding in $M(CO)_4$(alkyne) and $M(CO)_5$(alkyne) Complexes

The bonding in metal-alkyne complexes can be described using the Dewar-Chatt-Duncanson (DCD) model[21], where the interaction is split into donation and back donation components (Figure 1-2). Donation occurs from the alkyne's filled $\pi_\parallel$ orbital into an empty metal orbital resulting in a σ interaction. Back donation (π interaction) from a filled metal d orbital into the antibonding $\pi_\parallel^*$ orbital completes the metal-alkyne bond. Both donation and back donation occur at the same time and in a synergic fashion.

Back donation into the alkyne's $\pi_\parallel^*$ orbital lengthens the carbon-carbon bond, giving the carbons more sp^2 character. The degree of back donation relative to donation determines the extent of the metal-alkyne interaction. When donation dominates (electron rich alkynes), the bonding extreme is represented by **A** (see page 8) and the alkyne bond approximates a triple bond. For the case when back

Scheme 1-1. Representative Condensation Reactions of $Os(CO)_4(HC{\equiv}CH)$

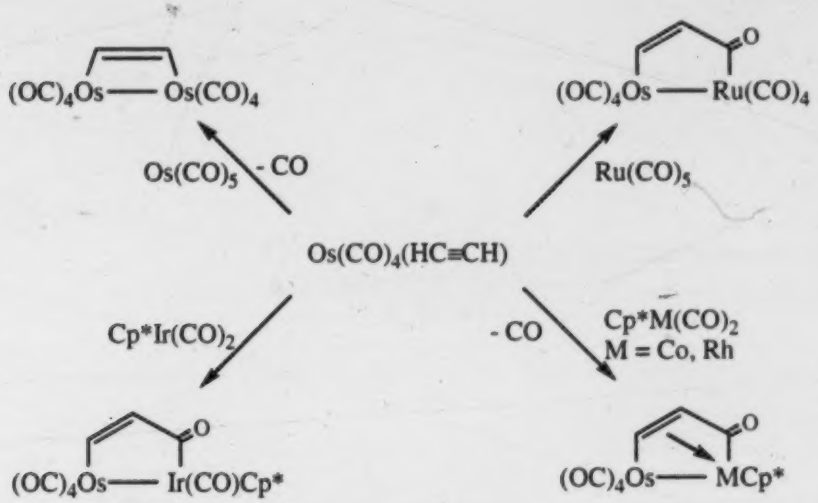

Scheme 1-2. Representative Condensation Reactions of $Fe(CO)_4(RC{\equiv}CR)$

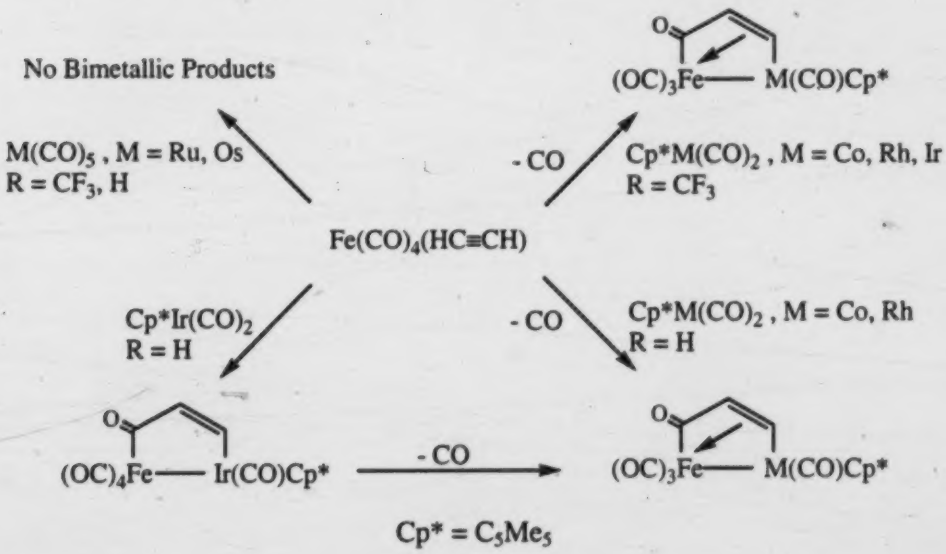

Figure 1-2. Components of the Metal-Alkyne Bond Involving the $\pi_{\parallel}$ Orbital

Donation Back Donation

donation dominates (π-acidic alkynes), the alkyne bond approaches a double bond, with increased metal to carbon interaction, forming the metallacyclopropene extreme (**B**).

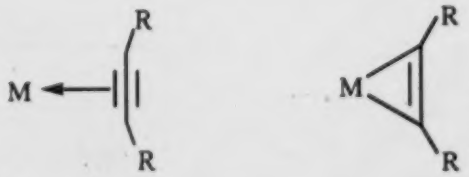

A **B**

The remaining $\pi_{\perp}/\pi_{\perp}$* set of alkyne orbitals can also interact with the metal center, giving the alkyne the ability to donate four electrons (Figure 1-3). The $\pi_{\perp}$ orbital can interact with a suitable metal d orbital of π symmetry resulting in donation if the metal orbital is empty or repulsion when it is full ($4e^-$ destabilization). Again, there is the possibility of back donation from a filled metal d orbital into the $\pi_{\perp}$* orbital, yielding a δ type interaction.

From Hoffmann's fragment approach and associated frontier orbitals[22], the interaction diagrams for the d^6 and d^8 metal-alkyne species are shown in Figure 1-4. The diagrams show the molecular orbitals that are important for the

metal alkyne bonding and the differences (type and relative energy) in the molecular orbitals between the group 6 and group 8 species.

Figure 1-3. Metal-Alkyne Bonding Components Involving the $\pi_\perp$Orbital

Donation/Repulsion Back Donation

1.2 Theoretical Studies of Chemical Systems

Just as experimental chemistry is a useful route to the characterization of chemical species and their reactivity, theoretical calculations on chemical systems can be just as enlightening. From calculations, the species' structure and properties (for example: excitation energy, IR spectra, and bond dissociation energy) can be determined and compared with experiment. In addition, mechanistic aspects of chemical reactions can be explored through the calculation of isotope effects, giving information that is not always accessible via experiment.

1.2.1 Density Functional Theory

The use of computational chemistry in the studies of transition metal systems has dramatically increased in the last 10-15 years. This is due, in part, to major advances in computing power that have shortened the time required for calculations, making it possible to look at these many electron systems. In addition, recent developments in Density Functional Theory (DFT), which performs reasonably well for transition metal systems when non-local functionals

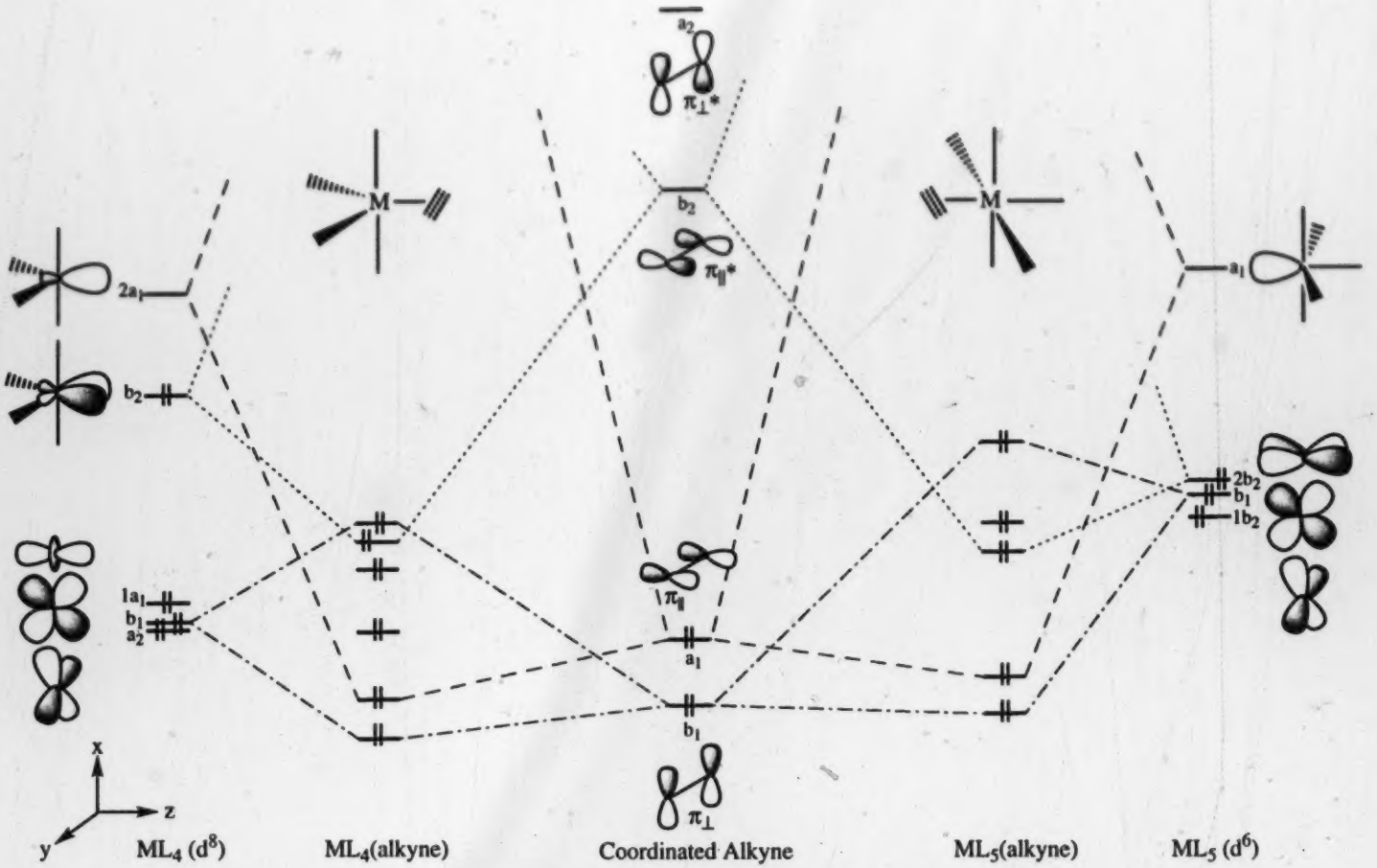

Figure 1-4. Group 6 and Group 8 Metal-Alkyne Interaction Diagram[23]

are employed[25], lead to a better understanding of organometallic chemistry based on sound theoretical foundations.

Ab-initio calculations can be split into two main classes: wave function theory (WFT) and DFT. Both methods are widely used and they both have advantages and disadvantages, depending on the type of system that is being studied.

WFT attempts to solve the Schrödinger equation (eq. 1-8) to get the properties of an n-electron system:

$$(1,2,...,n)\Psi(1,2,...,n) = E(1,2,...,n)\Psi(1,2,...,n) \qquad (1\text{-}8)$$

where is the hamiltonian, Ψ is the n-electron wavefunction (usually built from molecular orbitals, ϕ_i, whose form depends on the WFT method being implemented), and E is the total energy. The wavefunction is antisymmetric as a result of the fact that electrons are fermions, i.e. their spin is ½. The molecular orbitals in the wavefunction are solutions to the Hartree-Fock (HF) equations (eq. (1-9)):

$$h^{HF}\phi_i(\mathbf{r}) = \varepsilon_i\phi_i(\mathbf{r}) \quad i=1, \ldots \qquad (1\text{-}9)$$

where h^{HF} is the effective one-electron HF hamiltonian and ε_i is the energy of the molecular orbital ϕ_i.

For a closed-shell system, the effective HF hamiltonian is defined as:

$$h^{HF} = h + \sum_{j=1}^{n/2}[2J_j - K_j] \qquad (1\text{-}10)$$

where the one-electron operator $h = -\frac{1}{2}\nabla^2 + \sum_{A=1}^{nuclei}\left(-\frac{Z_A}{r_A}\right)$ and consists of kinetic energy and potential energy, J is the classic electronic (Coulomb) repulsion, and K is the exchange correction due to the fermion nature of electrons. The index j runs from 1 to the number of occupied molecular orbitals.

Ultimately, the Hartree-Fock energy can be written as:

$$E_{HF} = 2\sum_{i=1}^{n/2} H_{ii}^{core} + \sum_{i=1}^{n/2}\sum_{j=1}^{n/2}(2J_{ij} - K_{ij}) + V_{NN} \tag{1-11}$$

$$H_{ii}^{core} = \langle \phi_i(\mathbf{r}) | -\tfrac{1}{2}\nabla^2 - \sum_{\alpha}\frac{Z_\alpha}{r_\alpha} | \phi_i(\mathbf{r}) \rangle$$

$$J_{ij} = \left\langle \phi_i(\mathbf{r}_1)\phi_j(\mathbf{r}_2) \left| \frac{1}{r_{12}} \right| \phi_i(\mathbf{r}_1)\phi_j(\mathbf{r}_2) \right\rangle$$

$$K_{ij} = \left\langle \phi_i(\mathbf{r}_1)\phi_j(\mathbf{r}_2) \left| \frac{1}{r_{12}} \right| \phi_j(\mathbf{r}_1)\phi_i(\mathbf{r}_2) \right\rangle$$

with H_{ii}^{core} containing the kinetic and potential energies, J_{ij} representing the Coulomb repulsion energy, K_{ij} the exchange energy, and V_{NN} the nuclear-nuclear repulsion. In equation (1-11), the Dirac notation for integrals is used with $\langle f(\mathbf{r})|\hat{O}(\mathbf{r})|g(\mathbf{r})\rangle = \int f^*(\mathbf{r})\,\hat{O}\,g(\mathbf{r})\,dv$ where $\mathbf{r} = x_i, y_i, z_i$ (the coordinates for electron i), and $dv = dx\,dy\,dz$ is the volume element. Alternatively, the Hartree-Fock energy may be written in terms of the electron density:

$$E_{HF} = 2\sum_{i=1}^{n/2}\langle \phi_i(\mathbf{r}) | -\tfrac{1}{2}\nabla^2 | \phi_i(\mathbf{r}) \rangle - \sum_{\alpha}\int \frac{Z_\alpha \rho(\mathbf{r}_1)}{r_{1\alpha}} dv_1 + \frac{1}{2}\iint \frac{\rho(\mathbf{r}_1)\rho(\mathbf{r}_2)}{r_{12}} dv_1 dv_2 +$$

$$\sum_{i=1}^{n/2}\sum_{j=1}^{n/2}\left\langle \phi_i(\mathbf{r}_1)\phi_j(\mathbf{r}_2) \left| \frac{1}{r_{12}} \right| \phi_j(\mathbf{r}_1)\phi_i(\mathbf{r}_2) \right\rangle + V_{NN} \tag{1-12}$$

where $\rho(\mathbf{r}_1)$ is the electron density, $\rho(\mathbf{r}_1) = 2\sum_{i=1}^{n/2}|\phi_i(\mathbf{r}_1)|^2$. The ϕ_i's are usually expanded in terms of (known) basis set functions $\chi(\mathbf{r})$: $\phi_i(\mathbf{r}) = \sum_l d_{il}\chi_l(\mathbf{r})$.

The effective hamiltonian of equation (1-10) does not account for the instantaneous repulsion between electrons (correlation energy). Instead, the electron-electron repulsions are averaged through the Coulomb term, resulting in an approximate solution to the Schrödinger equation. The Hartree-Fock method works best in small systems where electron correlation does not have a large influence on system properties and where very large basis sets can be used.

Hartree-Fock calculations may be improved by the addition of electron correlation through configuration interaction (CI) or perturbation theory (Møller-Plesset, MP) methods, but these can be very time consuming. Often, the species' geometry is optimized at the HF level and then the fixed HF geometry is used for correlated calculations.

In transition metal compounds, correlated (post-Hartree-Fock) methods are generally not used since the large number of electrons in these systems makes the calculations prohibitively long, even when effective core potentials are used and the core electrons are not explicitly calculated. This leaves HF as an available method. However, it rarely shows reasonable agreement with experiment for transition metals, due to the lack of electron correlation, even though the basis sets used are larger than those that would be used with the correlated methods[25]. The alternative to the WFT approach is offered by DFT[26].

Modern DFT began in 1964 when Hohenberg and Kohn[27] proved that the energy of a chemical system is a unique functional of its electron density, $E[\rho(\mathbf{r})]$. However, the proof did not provide any information about the exact form of this functional. The feasibility of DFT as a computational method was increased dramatically in 1965 when Kohn and Sham derived the (Kohn-Sham) one-electron equations shown in equation (1-13)[28]. With the development of these equations, it was possible to make approximations to the density functional, which could then be used to calculate properties of chemical systems. The Kohn-Sham equations have the following form:

$$h^{KS}\phi_i(\mathbf{r}) = \varepsilon_i\phi_i(\mathbf{r}) \qquad i=1,\ldots \tag{1-13}$$

where h^{KS} is the effective Kohn-Sham hamiltonian expressed as a functional of density, the solutions, $\phi_i(\mathbf{r})$, are the Kohn-Sham orbitals, and ε_i is the energy of the Kohn-Sham orbital $\phi_i(\mathbf{r})$.

The general form of the effective Kohn-Sham hamiltonian is given as:

$$h^{KS} = -\tfrac{1}{2}\nabla^2 - \sum_{\alpha}\frac{Z_\alpha}{r_\alpha} + 2\sum_{j=1}^{n/2} J_j + V_{XC}(\mathbf{r}) \tag{1-14}$$

where $V_{XC}(\mathbf{r})$ is the exchange-correlation potential, defined as

$$V_{XC}(\mathbf{r}) = \frac{\delta E_{XC}[\rho(\mathbf{r})]}{\delta\rho(\mathbf{r})}, \tag{1-15}$$

and $E_{XC}[\rho(\mathbf{r})]$ is the exchange-correlation energy.

Using the Kohn-Sham one-electron orbitals, $\phi_i(\mathbf{r})$, the electron density of the system is calculated:

$$\rho(\mathbf{r}) = 2\sum_{i=1}^{n/2}\left|\phi_i(\mathbf{r})\right|^2 \tag{1-16}$$

from which the total energy, $E[\rho(\mathbf{r})]$, is found via the expression in equation (1-17), similar to the Hartree-Fock energy equation:

$$E[\rho(\mathbf{r})] = 2\sum_{i=1}^{n/2}\left\langle\phi_i(\mathbf{r})\right|-\tfrac{1}{2}\nabla^2\left|\phi_i(\mathbf{r})\right\rangle - \sum_{\alpha}\int\frac{Z_\alpha\rho(\mathbf{r}_1)}{r_{1\alpha}}dv_1 + \frac{1}{2}\iint\frac{\rho(\mathbf{r}_1)\rho(\mathbf{r}_2)}{r_{12}}dv_1dv_2 +$$

$$E_{XC}[\rho(\mathbf{r})] + V_{NN} \tag{1-17}$$

where $E_{XC}[\rho(\mathbf{r})]$ is the exchange-correlation functional of the density which is commonly split into separate exchange and correlation functionals (eq. (1-18)):

$$E_{XC}[\rho(\mathbf{r})] = E_X[\rho(\mathbf{r})] + E_C[\rho(\mathbf{r})] \tag{1-18}$$

The electron correlation and exchange functional forms are approximated using density functionals while the remaining terms are treated in the same manner as in the Hartree-Fock theory.

The various DFT functionals available in the literature differ in the form of the exchange and correlation functionals. The general notation is:

$$E_{X,C}[\rho(\mathbf{r})] = \int f[\rho_\alpha(\mathbf{r}), \rho_\beta(\mathbf{r}), \nabla\rho_\alpha(\mathbf{r}), \nabla\rho_\beta(\mathbf{r})]d\mathbf{r} \tag{1-19}$$

where the function f changes from functional to functional, ρ_σ is the density of the electrons with spin σ ($\sigma = \alpha$ or β), and $\nabla\rho_\sigma(\mathbf{r})$ is the gradient of the density. The earlier functionals were local functionals, depending only on the electron density itself. Non-local functionals include corrections using the gradient of the electron density. These functionals are more complex, requiring somewhat longer calculation times compared to the local functionals, and have been developed more recently.

In order to illustrate the complicated nature of the functionals which were devised by various fitting procedures, several commonly used functionals are given below.

I. Exchange functionals

i. Slater[29] (local)

$$E_X[\rho(\mathbf{r})] = \tfrac{2}{3}[\rho(\mathbf{r})]^{4/3} \tag{1-20}$$

ii. Becke[30] (non-local)

$$E_X[\rho(\mathbf{r})] = E_X^{LDA} - \beta\sum_\alpha \rho_\alpha^{4/3}(\mathbf{r})\frac{x_\alpha^2}{1+6x_\alpha\beta\sinh^{-1}(x_\alpha)} \tag{1-21}$$

where $x_\alpha = \dfrac{|\nabla\rho_\alpha|}{\rho_\alpha}$ and $\beta = 0.0042$.

II. Correlation functionals

i. VWN[31] (local)

$$E_C[\rho(\mathbf{r})] = \frac{A}{2}\left[\ln\frac{x^2}{X(x)} + \frac{2b}{Q}\tan^{-1}\frac{Q}{2x+b} - \frac{bx_o}{X(x_o)}\left(\ln\frac{(x-x_0)^2}{X(x)} + \frac{2(b+2x_o)}{Q}\tan^{-1}\frac{Q}{2x+b}\right)\right] \tag{1-22}$$

where $x = r_s^{\frac{1}{2}}$, $X(x) = x^2 + bx + c$, $Q = (4c-b^2)^{\frac{1}{2}}$, $A = 0.0621814$, $x_o = -0.409286$, $b = 13.0720$, and $c = 42.7189$, and r_s, the Wigner-radius, is defined as $\dfrac{1}{\rho} = \dfrac{4\pi}{3}(r_s)^3$.

ii. PW91[32] (non-local)

$$E_C[\rho(\mathbf{r})] = E_C^{VWN}[\rho(\mathbf{r})] + \rho(\mathbf{r})\frac{\beta}{2\alpha}\ln\left[1+\frac{2\alpha}{\beta}\frac{\beta+At^4}{1+At^2+A^2t^4}\right]+$$

$$C_{c0}[C_c(\rho(\mathbf{r})) - C_{c1}]t^2 e^{-100s^2} \qquad (1\text{-}23)$$

where $A = \frac{2\alpha}{\beta}\left[e^{-2\alpha E_C^{VWN}(\rho)/(\rho\beta^2)} - 1\right]^{-1}$, $t = \frac{\left(\frac{\pi}{3}\right)^{\frac{1}{2}}}{4}\frac{|\nabla\rho|}{\rho^{\frac{7}{6}}}$, $\alpha = 0.09$,

$\beta = 0.0667263212$, $C_{c0} = 15.7559$, $C_{c1} = 0.0035521$,

$C_c(\rho) = c_1 + \frac{c_2 + c_3 r_s + c_4 r_s^2}{1 + c_5 r_s + c_6 r_s^2 + c_7 r_s^3}$, $c_1 = 0.001667$, $c_2 = 0.002568$, $c_3 = 0.023266$,

$c_4 = 7.389$, $c_5 = 8.723$, $c_6 = 0.472$, and $c_7 = 0.07389$.

III. Hybrid functionals

A linear combination of HF exchange with density functional exchange and correlation are known as hybrid functionals. Becke's 3 - parameter hybrid[33] functional has the form:

$$E_{XC}[\rho(\mathbf{r})] = A * E_X^{Slater} + (1-A) * E_X^{HF} + B * \Delta E_X^{Becke} + E_C^{VWN} + C * E_C^{non-local} \qquad (1\text{-}24)$$

The parameters A, B, and C (A=0.80, B=0.72, C=0.81) were determined from fitting the functional to the Gaussian - 1 (G1) database of atoms and molecules of Pople and co-workers using the non-local PW91 correlation functional (B3PW91). The G1 set is comprised of 55 species containing first and second row atoms. In the Gaussian 94 program, changing the non-local correlation contribution changes the overall functional (B3PW88, B3LYP), but the parameter values are not changed.

As mentioned before, the exact form of $E_{XC}[\rho(\mathbf{r})]$ in h^{KS} and $E[\rho(\mathbf{r})]$ is not known in DFT and the approximate forms of the density functionals available will not give the exact electron density; this will only happen when the functional form is exact. This means that the functionals have to be tested on systems of interest,

with the results being compared to experiment. The functional with the best agreement is then used to study the system in more detail. The unpredictability of these functionals and a lack of a methodical approach in the development of these functionals are major drawbacks with this theory.

In transition metal systems, where it is too expensive to use correlated methods such as CI and MPn (n = the order of the perturbation), DFT is the method of choice. While it offers only approximate functionals that must be tested and calibrated, it nevertheless affords an acceptable amount of correlation and it can do calculations in a realistic time frame. Reasonable agreement with experiment is much more likely with DFT than with HF in transition metal systems.

1.2.2 Calculations using Statistical Mechanics

Quantum chemistry of isolated molecules, studied at absolute zero (0 K), provides a wide range of molecular features. From the molecule's energy at an optimized geometry, various energy differences can be calculated, such as bond dissociation energy. The molecule's moments of inertia I_A, I_B, and I_C are available once the geometry has been optimized. A subsequent hessian calculation gives the curvature of the potential energy surface at the optimized geometry. This indicates whether the stationary point is a minimum, maximum, or an n^{th}-order saddle point (where n=1 for a transition state). In addition, harmonic vibrational modes are generated, from which the zero point energy (ZPE) of the molecule is calculated:

$$\mathrm{ZPE} = \tfrac{1}{2}\sum_{i=1}^{M} h\nu_i \qquad (1\text{-}25)$$

where M is the number of vibrational modes and ν_i is the frequency of mode i and h is the Planck constant. Using these frequencies, an IR spectrum can be generated.

When studying an assembly of molecules at temperatures greater than absolute zero statistical mechanics is employed. Starting from the molecular energy levels, the molecular partition function (Q) is calculated which can then be used to find thermodynamic properties such as enthalpy, entropy, and heat capacities.

The molecular partition function is defined as

$$Q = \sum_i \exp(-\varepsilon_i / k_B T) \tag{1-26}$$

where ε_i is the molecular energy level i (in Joules), k_B is the Boltzmann constant, and T is the temperature (in Kelvins).

The molecular energy levels arise from translational, rotational, vibrational, and electronic motion. Usually, it is assumed that translational, rotational, vibrational, and electronic motions are uncoupled. This allows the molar partition function to be separated into four factors:

$$Q = Q_{tr} \bullet Q_{rot} \bullet Q_{vib} \bullet Q_{elec} \tag{1-27}$$

which are simply the partition functions for each mode of motion as defined below:

$$Q_{tr} = (2\pi m k_B T)^{3/2} h^{-3} V \tag{1-28}$$

where m is the mass of the molecule (in kg), k_B is the Boltzmann constant, h is Planck's constant, and V is the volume of a cubic box that would hold the molecules (V=RT/P).

$$Q_{rot} = \frac{8\pi^2}{\sigma h^2} (2\pi k_B T)^{3/2} (I_A I_B I_C) \tag{1-29}$$

where σ is the symmetry number and refers to the number of indistinguishable orientations of the molecule and I_A, I_B, and I_C are the moments of inertia of the molecule.

$$Q_{vib} = \prod_{i}^{M} (1 - e^{-h\nu_i / k_B T})^{-1} \tag{1-30}$$

where ν_i are the vibrational frequencies of the molecule.

$$Q_{elec} = \sum g_i \exp(-\varepsilon_i / k_B T) \tag{1-31}$$

where g is the degeneracy and ε_i is the excitation energy for the electronic state i.

1.2.3 Equilibrium Constant

Besides thermodynamic properties, the partition function Q is also used in the calculation of equilibrium constants. For the equilibrium R ⇌ P corresponding to, for example, isomerization, the population of the energy levels of the two species is dictated by the Boltzmann distribution for a particular temperature. The side of the equilibrium that is favored depends on the relative density of states for both R and P. Figure 1-5 shows this schematically with identical spacings for R and P in **A** and much smaller spacings for P in **B**. In this example, R is the lower energy species but this does not have to be the case.

The molar partition function for both species can be separated into the four modes of motion:

$$Q^R = Q^R_{tr} \cdot Q^R_{rot} \cdot Q^R_{vib} \cdot Q^R_{elec} \tag{1-32}$$

$$Q^P = Q^P_{tr} \cdot Q^P_{rot} \cdot Q^P_{vib} \cdot Q^P_{elec} \tag{1-33}$$

and the equilibrium constant, K, defined as:

$$K = \frac{Q^P}{Q^R} \exp(-\Delta E / k_B T) \tag{1-34}$$

where $\Delta E = E^P_o - E^R_o$ (with E^P_o and E^R_o denoting the zero-point energies of product and reactant molecules) and may be decomposed as

$$K = Q^{P/R}_{tr} \cdot Q^{P/R}_{rot} \cdot Q^{P/R}_{vib} \cdot Q^{P/R}_{elec} \exp(-\Delta E / k_B T) \tag{1-35}$$

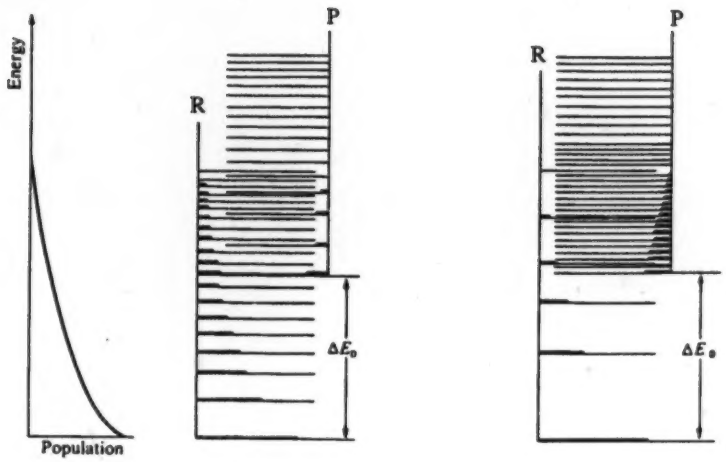

Figure 1-5. Energy Level Diagram for R⇌ P [37];
A : R and P have equal energy spacings,
B: P has smaller energy spacings than R

The contribution from the vibrational partition function can be further separated into components from the individual modes:

$$Q_{vib}^{P/R} = \frac{\prod_{p=1}^{M_P}(1-e^{-h\nu_p^P/k_BT})^{-1}}{\prod_{r=1}^{M_R}(1-e^{-h\nu_r^R/k_BT})^{-1}} = \prod_{i=1}^{M}\frac{(1-e^{-h\nu_i^R/k_BT})}{(1-e^{-h\nu_i^P/k_BT})}, \qquad \text{where } M_R = M_P = M, \tag{1-36}$$

where, for a non-linear molecule, $M_R = 3N_R\text{-}6$, $M_P = 3N_P\text{-}6$, and N_R and N_P are the number of atoms in R and P, respectively.

The exponential factor in the equilibrium constant accounts for the difference in the origin of energy scales in the species R and P (see Figure 1-5). When both species have the same energy spacings and zero of energy, the equilibrium constant simplifies to $K = \frac{Q^P}{Q^R}$. Therefore,

$$\Delta E = E_o^P - E_o^R = E^P + ZPE^P - \left(E^R + ZPE^R\right)$$

$$= \left(E^P - E^R\right) + \left(ZPE^P - ZPE^R\right)$$

$$= \left(E^P - E^R\right) + \tfrac{1}{2}\sum_{p=1}^{M_P} h\nu_p^P - \tfrac{1}{2}\sum_{r=1}^{M_R} h\nu_r^R \qquad (1\text{-}37)$$

$$= \left(E^P - E^R\right) + \tfrac{1}{2}\sum_{i=1}^{M} h(\nu_p^P - \nu_r^R), \qquad \text{where } M_R = M_P = M. \quad (1\text{-}38)$$

As equation (1-38) shows, the exponential factor can be separated into individual vibrational mode components. However, this may be done only when the vibrational modes of R can be mapped (correlated) onto the modes of species P (e.g. in an isomerization reaction).

1.2.4 Rate Constant

For the equilibrium, R⇌P, both R and P are minima on the potential energy surface (Figure 1-6) and are treated in an analogous manner. For reactions that proceed through an activated complex A (i.e. transition state, TS), R⇌A, only R is a minimum, with A being a 1st order saddle point with one imaginary frequency (Figure 1-7). The rate constant for such a reaction is given by:

$$k = \left(\frac{k_B T}{h}\right)\frac{Q^A}{Q^R}\exp\left(-\Delta E / k_B T\right) \qquad (1\text{-}39)$$

which is very similar to the equilibrium constant expression. The reactant, R, is treated just as in the equilibrium constant evaluation, whereas the activated complex must be treated differently. The imaginary frequency, corresponding to the motion along the reaction coordinate as shown in Figure 1-4, is omitted from both the partition function and exponential terms. The term $\frac{k_B T}{h}$ is included, representing the frequency associated with molecules passing through A to form products.

The partition functions can be again separated into the modes of motion to give:

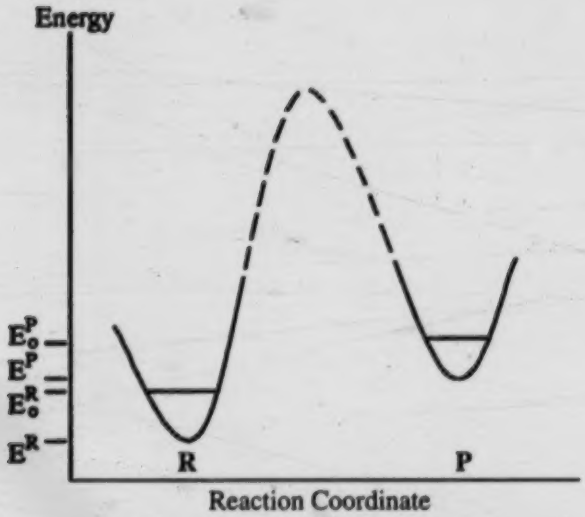

Figure 1-6. Potential Energy Change Along the Reaction Coordinate for R ⇌ P

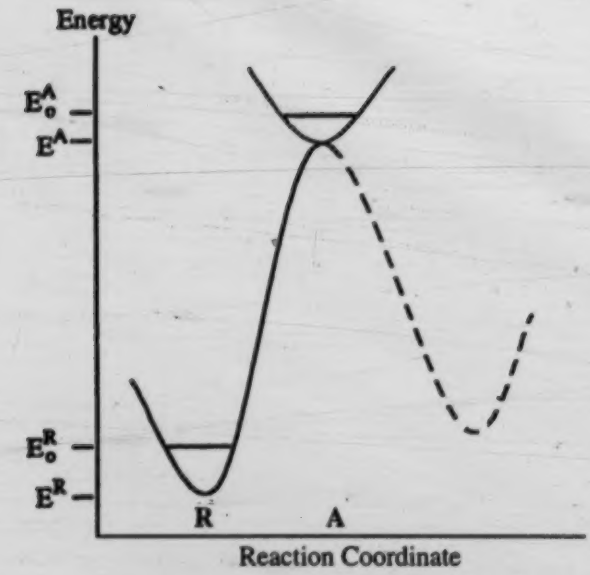

Figure 1-7. Potential Energy Change Along the Reaction Coordinate for R ⇌ A

$$k = \left(\frac{k_B T}{h}\right) Q_{tr}^{A/R} Q_{rot}^{A/R} Q_{vib}^{A/R} Q_{elec}^{A/R} \exp(-\Delta E / k_B T) \tag{1-40}$$

where

$$Q_{vib}^{A/R} = \frac{\prod_{a=1}^{M_A} (1 - e^{-h\nu_a^A / k_B T})^{-1}}{\prod_{r=1}^{M_R} (1 - e^{-h\nu_r^R / k_B T})^{-1}} = \frac{\prod_{r=1}^{M_R} (1 - e^{-h\nu_r^R / k_B T})}{\prod_{a=1}^{M_A} (1 - e^{-h\nu_a^A / k_B T})} \tag{1-41}$$

with $M_A = 3N_A\text{-}7$ (imaginary frequency ignored) and $M_R = 3N_R\text{-}6$ for non-linear systems. The exponential term in equation (1-39) accounts for the energy separation between R and A (see Figure 1-7) and may be separated into contributions due to individual vibrations.

$$\Delta E = E_o^A - E_o^R = E^A - E^R + \tfrac{1}{2}\sum_{a=1}^{M_A} h\nu_a^A - \tfrac{1}{2}\sum_{r=1}^{M_R} h\nu_r^R \tag{1-42}$$

The rate constant can be thought of as a special case of the equilibrium constant with the differences arising solely from the activated complex being a transition state rather than a minimum.

1.2.5 Isotope Effects

The theoretical expressions for the equilibrium and rate constants may be used to develop the theory of isotope effects in chemical reactions. Isotope effects refer to the change in the reaction rate or equilibrium constant when an atom is isotopically substituted (e.g. D for H). They are commonly used in organic chemistry as a tool in the study of reaction mechanisms, with their use growing in organometallic chemistry.

There are two types of isotope effects: equilibrium isotope effects (EIE) and kinetic isotope effects (KIE). EIEs occur in chemical equilibria and are defined as follows (using the H/D isotope pair):

$$EIE = \frac{K_H}{K_D} = \frac{Q_{tr}^{P_H/R_H} Q_{rot}^{P_H/R_H} Q_{vib}^{P_H/R_H} Q_{elec}^{P_H/R_H}}{Q_{tr}^{P_D/R_D} Q_{rot}^{P_D/R_D} Q_{vib}^{P_D/R_D} Q_{elec}^{P_D/R_D}} \frac{\exp(-\Delta E_H / k_B T)}{\exp(-\Delta E_D / k_B T)} \tag{1-43}$$

where

$$\frac{Q_{vib}^{P_H/R_H}}{Q_{vib}^{P_D/R_D}} = \frac{\prod_{r=1}^{M_R}(1-e^{-h\nu_r^{R_H}/k_B T}) \Big/ \prod_{p=1}^{M_P}(1-e^{-h\nu_p^{P_H}/k_B T})}{\prod_{r=1}^{M_R}(1-e^{-h\nu_r^{R_D}/k_B T}) \Big/ \prod_{p=1}^{M_P}(1-e^{-h\nu_p^{P_D}/k_B T})} \tag{1-44}$$

$$\begin{aligned}
\frac{\exp(-\Delta E_H / k_B T)}{\exp(-\Delta E_D / k_B T)} &= \exp\left\{-\left(\left[E^P - E^R + \tfrac{1}{2}\sum_{p=1}^{M_P} h\nu_p^{P_H} - \tfrac{1}{2}\sum_{r=1}^{M_R} h\nu_r^{R_H}\right] - \right.\right. \\
&\qquad \left.\left. \left[E^P - E^R + \tfrac{1}{2}\sum_{p=1}^{M_P} h\nu_p^{P_D} - \tfrac{1}{2}\sum_{r=1}^{M_R} h\nu_r^{R_D}\right]\right) \Big/ k_B T\right\} \\
&= \exp\left\{-\left(\left[\tfrac{1}{2}\sum_{r=1}^{M_P} h(\nu_p^{P_H} - \nu_p^{P_D})\right] - \left[\tfrac{1}{2}\sum_{r=1}^{M_R} h(\nu_r^{R_H} - \nu_r^{R_D})\right]\right) \Big/ k_B T\right\} \\
&= \exp\left\{-\left(\Delta ZPE^P - \Delta ZPE^R\right) \Big/ k_B T\right\}
\end{aligned} \tag{1-45}$$

and the Q_{elec} term is identical for the light and heavy species. Therefore, the EIE expression becomes

$$\begin{aligned}
\frac{K_H}{K_D} &= \frac{Q_{tr}^{P_H/R_H}}{Q_{tr}^{P_D/R_D}} \frac{Q_{rot}^{P_H/R_H}}{Q_{rot}^{P_D/R_D}} \times \\
&\quad \frac{\prod_{r=1}^{M_R}(1-e^{-h\nu_r^{R_H}/k_B T}) \Big/ \prod_{p=1}^{M_P}(1-e^{-h\nu_p^{P_H}/k_B T})}{\prod_{r=1}^{M_R}(1-e^{-h\nu_r^{R_D}/k_B T}) \Big/ \prod_{p=1}^{M_P}(1-e^{-h\nu_p^{P_D}/k_B T})} \exp\left\{-\left(\frac{\Delta ZPE^P - \Delta ZPE^R}{k_B T}\right)\right\}
\end{aligned} \tag{1-46}$$

While the rate constant equation is slightly different from the equilibrium constant, the related KIE expression is similar to EIE:

$$KIE = \frac{k_H}{k_D} = \frac{\frac{k_B T}{h}}{\frac{k_B T}{h}} \frac{Q_{tr}^{A_H/R_H} Q_{rot}^{A_H/R_H} Q_{vib}^{A_H/R_H} Q_{elec}^{A_H/R_H}}{Q_{tr}^{A_D/R_D} Q_{rot}^{A_D/R_D} Q_{vib}^{A_D/R_D} Q_{elec}^{A_D/R_D}} \frac{\exp(-\Delta E_H / k_B T)}{\exp(-\Delta E_D / k_B T)} \tag{1-47}$$

where

$$\frac{Q_{vib}^{A_H/R_H}}{Q_{vib}^{A_D/R_D}} = \frac{\prod_{r=1}^{M_R}(1-e^{-h\nu_r^{R_H}/k_BT}) \Big/ \prod_{a=1}^{M_A}(1-e^{-h\nu_a^{A_H}/k_BT})}{\prod_{r=1}^{M_R}(1-e^{-h\nu_r^{R_D}/k_BT}) \Big/ \prod_{a=1}^{M_A}(1-e^{-h\nu_a^{A_D}/k_BT})} \tag{1-48}$$

$$\frac{\exp(-\Delta E_H/k_BT)}{\exp(-\Delta E_D/k_BT)} = \exp\left\{-\left(\left[E^A - E^R + \tfrac{1}{2}\sum_{a=1}^{M_A} h\nu_a^{A_H} - \tfrac{1}{2}\sum_{r=1}^{M_R} h\nu_r^{R_H}\right] - \left[E^A - E^R + \tfrac{1}{2}\sum_{a=1}^{M_A} h\nu_a^{A_D} - \tfrac{1}{2}\sum_{r=1}^{M_R} h\nu_r^{R_D}\right]\right) \Big/ k_BT\right\}$$

$$= \exp\left\{-\left(\left[\tfrac{1}{2}\sum_{r=1}^{M_R} h(\nu_r^{P_H} - \nu_r^{P_D})\right] - \left[\tfrac{1}{2}\sum_{r=1}^{M_R} h(\nu_r^{R_H} - \nu_r^{R_D})\right]\right) \Big/ k_BT\right\}$$

$$= \exp\left\{-\left(\Delta ZPE^A - \Delta ZPE^R\right) \Big/ k_BT\right\} \tag{1-49}$$

and again Q_{elec} is the same for both the light and heavy species to give (eq. 1-50):

$$\frac{k_H}{k_D} = \frac{\frac{k_BT}{h}\frac{Q_{tr}^{A_H/R_H}}{Q_{tr}^{A_D/R_D}}\frac{Q_{rot}^{A_H/R_H}}{Q_{rot}^{A_D/R_D}}}{\frac{k_BT}{h}} \times \frac{\prod_{r=1}^{M_R}\left(1-e^{-h\nu_r^{R_H}/k_BT}\right) \Big/ \prod_{a=1}^{M_A}\left(1-e^{-h\nu_a^{A_H}/k_BT}\right)}{\prod_{r=1}^{M_R}\left(1-e^{-h\nu_r^{R_D}/k_BT}\right) \Big/ \prod_{a=1}^{M_A}\left(1-e^{-h\nu_a^{A_D}/k_BT}\right)} \exp\left\{-\left(\frac{\Delta ZPE^A - \Delta ZPE^R}{k_BT}\right)\right\} \tag{1-50}$$

Isotope effects can be either normal (>1), inverse (<1), or when $K_H/K_D = 1$ and $k_H/k_D = 1$ there is no change after isotopic substitution. Through the separation of terms in the isotope effect expressions, it may be possible to identify the origin of the effect. For instance, the contribution from each of the separated partition functions is indicative of the role that particular mode of motion has in the overall isotope effect. As well, the individual mode contributions in the partition function and exponential terms can be combined to give the full vibrational contribution to the EIE/KIE from each mode.

1.3 Scope of the Thesis

As implied in the preceding sections, the research presented in this thesis was conducted in two streams: experimental and computational.

In view of the enhanced CO lability of group 8 $M(CO)_4$(alkyne) complexes, it was of interest to investigate whether this was a unique property of the iron triad or whether it extended to the analogous group 6 $M(CO)_5$(alkyne) complexes as well. To this end the synthesis of some $W(CO)_5$(alkyne) complexes was attempted in order to compare their phosphine substitution behavior with their group 8 analogues.

The unusual condensation of $M(CO)_4$(alkyne) (M = Fe, Ru, Os) complexes with saturated, 18e$^-$, group 8 $M(CO)_5$ and group 9 $Cp'M(CO)_2$ ($Cp' = C_5H_5$, C_5Me_5) compounds has been extensively studied with a wide range of bimetallacycle products being isolated. However, the mechanism of the reaction has not been investigated. To gain further insight into the formation of the bimetallic compounds, the kinetics of the condensation reaction of $Ru(CO)_4$(HFB) with $Os(CO)_5$, $Cp^*Rh(CO)_2$, and $Cp^*Ir(CO)_2$ was carried out.

To gain a better understanding of the factors governing the reactivity of these systems and of the anticipated differences between group 8 and 6 transition metal alkyne-carbonyl complexes, DFT calculations were carried out and the performance of density functional theory on these transition metal systems was evaluated.

The calculation of isotope effects is especially useful when experiment alone cannot deduce the origin of the observed effect. With the ability to separate the isotope effect into translational, rotational, vibrational, and electronic excitation terms (in the partition functions), and a zero-point energy contribution

(in the exponential term), the origin of the resultant effect becomes more obvious. Further separation of the total vibrational component allows specific vibrations to be identified as sources of the observed effect.

Isotope effects for simple organic addition reactions were calculated and separated into the above contributions to further study the origin of the experimentally observed effects.

1.4 References

1. Hübel, W. In *Organic Synthesis via Metal Carbonyls Vol. 1*; Wender, I., Pino, P., Eds.; Wiley-Interscience: New York, 1968, p. 273 and references within.
2. Pannell, K. H.; Crawford, G. M. *J. Coord. Chem.* **1973**, *2*, 251.
3. Cotton, F. A.; Jamerson, J. D.; Stults, B. R. *J. Am. Chem. Soc.* **1976**, *98*, 1774.
4. Carty, A. J.; Smith, W. F.; Taylor, N. J. *J. Organomet. Chem.* **1978**, *146*, C1.
5. Rossi, A. R.; Hoffmann, R. *Inorg. Chem.* **1975**, *14*, 365.
6. Ball, R. G.; Burke, M. R.; Takats, J. *Organomet.* **1987**, *6*, 1918.
7. Gagné, M. R.; Takats, J. *Organometal.* **1988**, *7*, 561.
8. Burn, M. J.; Kiel, G.-Y.; Seils, F.; Takats, J.; Washington, J. *J. Am. Chem. Soc.* **1989**, *111*, 6850.
9. Cooke, J.; Takats, J. *J. Am. Chem. Soc.* **1997**, *119*, 11088.
10. Stolz, I. W.; Dobson, G. R.; Sheline, R. K. *Inorg. Chem.* **1963**, *2*, 1264.
11. Landon, S. J.; Shulman, P. M.; Geoffroy, G. L. *J. Am. Chem. Soc.* **1985**, *107*, 6739.
12. Fischer, H.; Volkland, H.-P.; Früh, A.; Stumpf, R. *J. Organomet. Chem.* **1995**, *491*, 267.
13. Szymańska-Buzar, T.; Downs, A. J.; Greene, T. M.; Marshall, A. S. *J. Organomet. Chem.* **1995**, *495*, 163.
14. Jacké, J. PhD. Thesis, Universität-Gesamthochschule-Duisburg, 1989.
15. Pearson, J.; Cooke, J.; Takats, J.; Jordan, R. B. *J. Am. Chem. Soc.* **1998**, *120*, 1434.
16. Washington, J.; McDonald, R.; Takats, J.; Menashe, N.; Reshef, D.; Shvo, Y. *Organometal.* **1995**, *14*, 3996.
17. Mao, T.-F. PhD. Thesis, University of Alberta, 1996.
18. Espuelas, J.; Esteruelas, M. A.; Lahoz, F. J.; López, A. M.; Oro, L. A.; Valero, C. *J. Organomet. Chem.* **1994**, *468*, 223.
19. Cooke, J. PhD. Thesis, University of Alberta, 1998.

20. Takats, J. *J. Cluster Science* **1992**, *3*, 479.

21. (a) Chatt, J.; Duncanson, L. A. *J. Chem. Soc.* **1953**, 2939. (b) Dewar, M. J. S. *J. Am. Chem. Soc.* **1979**, *101*, 783 and references therein.

22. (a) Elian, M.; Hoffmann, R. *Inorg. Chem.* **1975**, *14*, 1058. (b) Hoffmann, R. *Science* **1981**, *211*, 995. (c) Hoffmann, R. *Angnew. Chem. Int. Ed. Engl.* **1982**, *21*, 711.

23. The relative ordering of the molecular orbital energy levels was calculated with the extended Hückel program, YAeHMOP[24], and its associated fragment orbital analysis using the geometry of $Os(CO)_4$(HFB) and $W(CO)_5$(HFB) as discussed in Chapter 3.

24. YAeHMOP (Yet Another extended Hückel Molecular Orbital Program), Version 1.2, Greg Landrum, February 26, 1996.

25. *The Challenge of d and f Electrons Theory and Computation*; Salahub, D. R., Zerner, M. C., Eds.; American Chemical Society: Washington, DC, 1989.

26. *Density Functional Methods in Chemistry*; Andzelm, J. W., Labanowski, J. K., Eds.; Springer-Verlag: New York, 1991.

27. Hohenberg, P.; Kohn, W. *Phys. Rev. B* **1964**, *136*, 864.

28. Kohn, W.; Sham, L. J. *Phys. Rev. A* **1965**, *140*, 1133.

29. Slater, J. C. *Quantum Theory of Molecular Solids Vol. 4: The Self-Consistent Field for Molecules and Solids*; McGraw-Hill: New York, 1974.

30. Becke, A. D. *Phys. Rev. A* **1988**, *38*, 3098.

31. Vosko, S. H.; Wilk, L.; Nusair, M. *Can. J. Phys.* **1980**, *58*, 1200.

32. Perdew, J. P.; Wang, Y. *Phys. Rev. B* **1992**, *45*, 13244.

33. Becke, A. D. *J. Chem. Phys.* **1993**, *98*, 5648.

34. Levine, I. N. *Quantum Chemistry, 4th Ed.*; Prentice-Hall: New Jersey, 1991.

35. Parr, R. G.; Yang, W. *Density-Functional Theory of Atoms and Molecules*; Oxford University Press: New York, 1989.

36. Wiberg, K. B. *Physical Organic Chemistry*; John Wiley & Sons, Inc.: New York, 1964.

37. Atkins, P. W. *Physical Chemistry, 2nd. Ed.*; W. H. Freeman and Company: San Francisco, 1982.

38. *Computational Thermochemistry: Prediction and Estimation of Molecular Thermodynamics*; Irikura, K. K., Frurip, D. J., Eds.; *ACS Symposium Series No. 677*; ACS: Washington, DC, 1997.

Chapter Two

Synthesis and Phosphine Substitution of $M(CO)_x$(BTMSA) Compounds (M = Os, x = 4; M = W, x = 5)

2.1 Introduction

While the group 8 pentacarbonyl complexes are rather inert towards CO dissociation, requiring thermal or photochemical activation, the lability of the CO ligand is enhanced by the presence of an alkyne ligand. Kinetic studies on the phosphine substitution of $M(CO)_5$ (M = Fe, Ru, Os) and $M(CO)_4$(HFB) (M = Fe, Ru, Os) complexes clearly establish this with the substitution rate increasing by 13, 2, and 7 orders of magnitude for the HFB derivative of Fe, Ru, and Os, respectively[1]. The origin of this "alkyne effect" was attributed to the ability of the alkyne ligand to stabilize the dissociative, formally 16 - electron intermediate by π - donation from its $\pi_\perp$ orbital, that is by acting as a 4 - electron donor in the $[M(CO)_3$(alkyne)] intermediate.

During these studies it was also discovered that the $Os(CO)_4$(alkyne) complexes exhibit a wide array of phosphine substitution reactions that are alkyne and phosphine dependent[2]. With the electron-poor alkyne, HFB, single and double CO substitutions were observed, with the phosphines occupying the axial positions of the trigonal bipyramidal coordination geometry. With electron-rich alkynes, e.g. RC≡CR, R = H, Me, in addition to simple CO substitution, insertion of CO into the metal alkyne bond was also observed. Indeed, with the bulky $P(^tBu)_3$ ligand, the doubly CO-inserted product was obtained.

In view of the enhanced reactivity provided by the alkyne ligand in group 8 $M(CO)_4$(alkyne) compounds, it was of particular interest to establish whether this effect occurred with other transition metals as well.

Although, as indicated in Chapter 1, there are scattered reports on the solution IR characterization and recently on the isolation and structure of the group 6 $M(CO)_5$(alkyne) compounds[3,4,5], their substitution chemistry with phosphine ligands has not been investigated. Therefore, it became the goal of this study to synthesize a representative $W(CO)_5$(alkyne) compound and to compare its reactivity toward PMe_3 to the analogous $Os(CO)_4$(alkyne) compound.

2.2 Results

2.2.1 Attempted Preparations of $W(CO)_5(\eta^2\text{-}RC_2R)$ (R = H, CH_3, CF_3, CH_2CH_3)

Since the reactivity of $Os(CO)_4$(alkyne) compounds toward phosphines was mainly studied with HFB, the preparation of the similar tungsten compound was attempted. Using the successful preparation for the group 8 complexes (eq. (2-1)),

$$M(CO)_x + \text{alkyne} \xrightarrow[\text{low temp.}]{h\nu} M(CO)_{x-1}(\text{alkyne}) + CO \qquad (2\text{-}1)$$

the low temperature photolysis of $W(CO)_6$ and HFB was carried out. However, instead of $W(CO)_5$(HFB), the reaction produced $W(CO)(HFB)_3$, identified by IR bands at 2084 cm^{-1} (CO) and 1704 cm^{-1} (C≡C) which can be compared to other well known, analogous complexes first investigated by Tate *et al.*[6] (Table 2-1).

Table 2-1. Characteristic IR Bands for $W(CO)(alkyne)_3$ Complexes

Alkyne	CO (cm^{-1})	C≡C (cm^{-1})
Diphenylacetylene (DPA)	2072	1680
Methylphenyl-acetylene	2057	1731
Hexyne	2034	1702

The presence of other IR bands in the reaction mixture indicated that there were other products formed as well. However, the identification of $W(CO)_5$(HFB) could not be made conclusively.

Apparently $W(CO)_5$(HFB), if formed, underwent further reaction during the photolysis. To prevent further photochemical CO substitution by HFB, advantage was taken of the substitutionally labile $W(CO)_5(CH_2Cl_2)$ reagent. Indeed this species was used successfully by Fischer[4] to prepare a series of $W(CO)_5$(alkyne) compounds, with $W(CO)_5$(HCC(COOMe)) and $W(CO)_5$(DPA) being isolated (eq. (2-2)). Unfortunately, preparation of pure $W(CO)_5(CH_2Cl_2)$ requires -85 °C and, in particular, a falling-film photoreactor that was not available. Less than 50% conversion of $W(CO)_6$ to the CH_2Cl_2 adduct was possible and in the subsequent reaction with HFB the only product observed in the IR was the previously identified $W(CO)(HFB)_3$.

$$W(CO)_6 \xrightarrow[-CO]{h\nu/CH_2Cl_2/\,-85\,^\circ C} (OC)_5W(CH_2Cl_2) \xrightarrow[+\,HC\equiv CR]{-85\,^\circ C \;-\;CH_2Cl_2} (OC)_5W(HC\equiv CR) \quad (2\text{-}2)$$

R = Ph, ^{t}Bu, c-Hex, COOMe, C(=CH_2)Me, CH=C(OMe)H

Similar problems were encountered with acetylene, butyne, and hexyne. With the latter two ligands, conversion to the $W(CO)_5$(alkyne) complex was encouraging (> 80% from $W(CO)_5(CH_2Cl_2)$, judged from IR), but inability to separate the product from the remaining $W(CO)_6$ and the complex nature of subsequent *in situ* PR_3 substitution reactions led to curtailing these attempts.

Finally, it was decided to investigate the analogous group 6 and group 8 BTMSA compounds. Both are known to be stable and are structurally characterized[5,7]. Since the PR_3 substitution reactions of $Os(CO)_4$(BTMSA) had not been studied, this also became part of the project.

2.2.2 Reactions of $Os(CO)_4$(BTMSA) (1) with PMe_3

Reaction of $Os(CO)_4$(BTMSA) (**1**) with one equivalent of PMe_3 gave cleanly the monosubstituted product (**2a**) (eq. (2-3)). The reaction was monitored by IR spectroscopy which showed the disappearance of **1** (ν_{CO} = 2099, 2016, 2003, 1976 cm^{-1}) and formation of a single product (**2a**, ν_{CO} = 2036, 1959, 1933 cm^{-1}).

$$\underset{\mathbf{1}}{Os(CO)_4(BTMSA)} + PMe_3 \xrightarrow[\text{hexane}]{35\ ^\circ C} \underset{\mathbf{2a}}{Os(CO)_3(PMe_3)(BTMSA)} + CO \quad (2\text{-}3)$$

There are two isomers (**A** and **B**) that could form from the phosphine substitution as shown below:

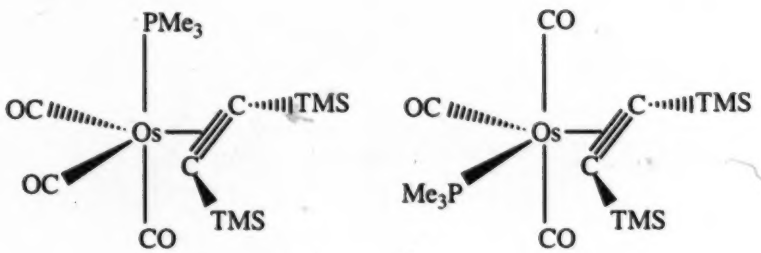

The ^{13}C NMR spectrum of the product has two doublets in the CO region, one at δ = 192.2 ($^2J_{PC}$ = 9.8 Hz) and the other at δ = 180.0 ($^2J_{PC}$ = 107.2 Hz), in an approximate 2:1 ratio. This indicates that one CO is distinct while the remaining two are equivalent. The two-bond coupling to phosphorus is large for the distinct CO, suggesting a trans arrangement. From these NMR data, it was concluded that isomer **A** is formed exclusively in the phosphine substitution. The $Os(CO)_3(PR_3)$(alkyne) complexes studied previously[2] also show the phosphine being in the axial position. This is in accord with the notion that σ - donor ligands, such as phosphines, prefer the axial position in trigonal bipyramidal geometries[8].

The CO trans to the phosphine receives more π - back donation from the metal center, whereas in the isomer with two mutually trans CO ligands, two π-acid ligands would compete for the same metal d_π orbitals.

The disubstituted product (**2b**) was obtained by reacting a small excess (2.2 equiv.) of PMe_3 with $Os(CO)_4BTMSA$ (eq. (2-4)).

$$\underset{\mathbf{1}}{Os(CO)_4(BTMSA)} + 2.2\ PMe_3 \xrightarrow[\text{hexane}]{35\ ^\circ C} \underset{\mathbf{2b}}{Os(CO)_2(PMe_3)_2(BTMSA)} + 2\ CO \quad (2\text{-}4)$$

There are three possible isomers for **2b**, but the NMR data show that only one is formed.

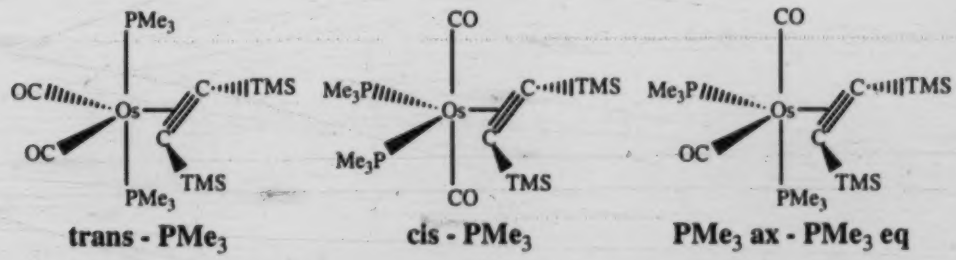

The $^{31}P\{^1H\}$ NMR spectrum shows a singlet at δ = -49.71 indicating that the two phosphorus atoms are equivalent in the molecule. The ^{13}C NMR spectrum has a single triplet at δ = 197.0 ($^2J_{PC}$ = 9.8 Hz) which shows that the two CO's are equivalent as well. The small phosphorus to carbon coupling is indicative of a cis arrangement between the carbonyl and phosphine ligands. Thus far the NMR data are consistent with both the trans - and cis- PMe_3 isomers, with the ^1H NMR spectrum providing the necessary distinction. The appearance of a "triplet" at δ = 1.02 ppm is indicative of the trans arrangement of the PMe_3 ligands[9] and is a manifestation of "virtual coupling". In both isomers the phosphines are not magnetically equivalent, $^2J_{PH} \neq {}^4J_{PH'}$ resulting in a ($X_9AA'X_9'$) spin system. Normally the $^2J_{PP}$ of trans phosphine ligands is large and in such cases the NMR

spectrum simplifies to the limiting case of $^2J_{PP} \gg |^2J_{PH} - {}^4J_{PH}|$. This results in a 1:2:1 triplet with half of the intensity in the outer two lines, separated by $|^2J_{PH} - {}^4J_{PH}|$ (7.0 Hz in the present case). In the cis-PMe_3 isomer, due to the smaller value of $^2J_{PP}$, the center line of the triplet would appear broadened, or split into a number of components. Thus, based on the NMR evidence, only the trans - PMe_3 isomer is formed in the double phosphine substitution reaction.

Both phosphine substitution reactions proceed cleanly. From IR monitoring of the double substitution, it was seen that the second step was slower than the first; practically all of the starting material was converted to the mono phosphine product before the di-substituted derivative appeared.

2.2.3 Reactions of $W(CO)_5$(BTMSA) (3) with PMe_3

$W(CO)_5$BTMSA (**3**) reacts with one equivalent of PMe_3 to give two products whose distribution changes with the reaction temperature.

At room temperature (eq. (2-5)), the reaction produces both the CO substituted **4a**, as the major product, and the alkyne substituted product **4b**.

$$\underset{\mathbf{3}}{W(CO)_5(BTMSA)} + PMe_3 \xrightarrow{RT} \underset{\mathbf{4a}}{W(CO)_4(PMe_3)(BTMSA)} + \underset{\mathbf{4b}}{W(CO)_5(PMe_3)} \quad (2\text{-}5)$$

A dark brown solid was isolated whose IR had the same composition as the final reaction mixture. To study its thermal stability, the isolated solid was dissolved in pentane and then stirred at room temperature overnight. Monitoring by IR, the bands of **4a** completely disappeared while there was an increase in the absorbance of the IR bands of **4b**. Although the solution remained clear during this time, some decomposition cannot be ruled out due to the small amount of solid available.

When the reaction was carried out at - 40 °C (eq. (2-6)), only **4a** was obtained, albeit very slowly (conversion of 35mg of **3** required 2 months). At this temperature, **4a** is stable and the decomposition to form **4b** is slowed down enough (or stopped) that **4a** can be isolated cleanly and characterized.

$$\underset{\mathbf{3}}{W(CO)_5(BMTSA)} + PMe_3 \xrightarrow{-40\,^{\circ}C} \underset{\mathbf{4a}}{W(CO)_4(PMe_3)(BTMSA)} + CO \quad (2\text{-}6)$$

As with the mono-substituted osmium derivative **2a**, **4a** can exist as two isomers (shown below). The PMe_3 ligand can be either cis or trans to the alkyne, creating different CO environments in the two isomers. It would be possible to differentiate between the isomers using ^{13}C NMR, by the number of signals in the CO region and the $^2J_{PC}$ coupling constants for those signals (Figure 2-1).

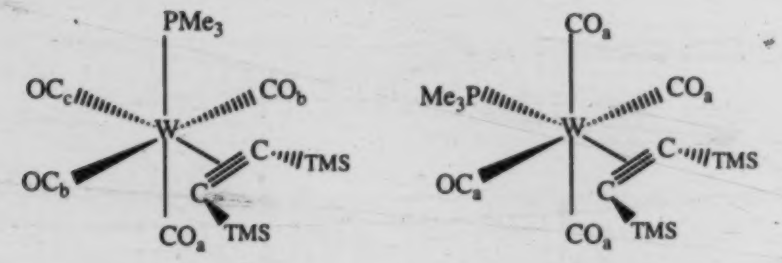

cis

3 doublets
CO_a - large $^2J_{PC}$ (1)
CO_b - small $^2J_{PC}$ (2)
CO_c - small $^2J_{PC}$ (1)

trans

1 doublet
CO_a - small $^2J_{PC}$

Figure 2-1. Geometrical Isomers of $W(CO)_4(PMe_3)(BTMSA)$; the expected number of ^{13}CO resonances and magnitude of $^2J_{PC}$ are shown, relative intensity in parenthesis

Unfortunately, there was not enough **4a** available to allow detection of the CO signals in the NMR and more material was not made due to the very long reaction time required for PMe_3 substitution to take place.

Similarily, there are two products formed when excess PMe_3 was reacted with **3** (eq. (2-7)).

$$W(CO)_5(BTMSA) + \text{excess } PMe_3 \xrightarrow{RT} [W(CO)_4(PMe_3)(BTMSA)] \quad \textbf{4a}$$

$$\longrightarrow W(CO)_4(PMe_3)_2 \; \textbf{4c} + W(CO)_5(PMe_3) \; \textbf{4b} \qquad (2\text{-}7)$$

IR monitoring revealed that, as in the reaction with one equivalent of PMe_3 (eq. (2-6)), the mono-CO substituted compound **4a** forms initially. This compound is thermally labile at room temperature and converts, before all of the starting material has reacted, to **4b** and **4c**. In the presence of excess PMe_3 the major product is **4c**, in fact the amount of **4b** that is formed is small enough (ca. 5-10%) that it does not interfere with characterization of **4c**. Therefore, in both reactions, CO substitution occurs first followed by alkyne displacement by either CO (**4b**) or PMe_3 (**4c**); clearly with excess PMe_3 competition between CO and PMe_3 favors the stronger ligand (PMe_3) and **4c** forms in preference of **4b**. Contrary to the osmium case, neither IR nor NMR showed the presence of the doubly substituted alkyne product, $W(CO)_3(PMe_3)_2(BTMSA)$.

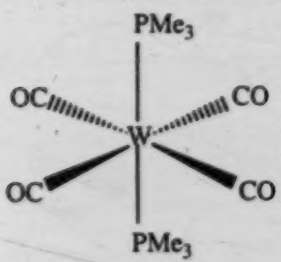

trans

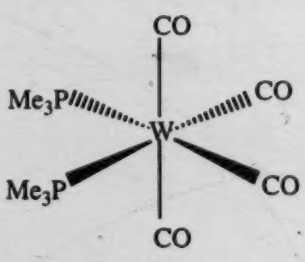

cis

In the bis-PMe_3 product (**4c**) the phosphines can be either cis or trans. The ^1H NMR spectrum shows a doublet at $\delta = 0.98$ ($^2J_{PH}$=7 Hz) due to the PMe_3 hydrogens. The four bond phosphorus-hydrogen coupling is not seen. The simple doublet suggests that the phosphines are cis to one another rather than trans

which is expected to show a virtual triplet like in the osmium system. There are two triplets in the CO region of the ^{13}C NMR spectrum at δ = 206.57 ($^2J_{PC}$ = 7.6 Hz) and δ = 203.51 ($^2J_{PC}$=8.4 Hz) for two different CO environments, which is in accord with the cis isomer. The axial CO's will be split into a triplet because of the chemically equivalent phosphorus atoms. Each equatorial CO is both cis and trans to a phosphine ligand with the expectation of a doublet of doublets splitting pattern. Apparently, the cis and trans carbon-phosphorus couplings are similar and a triplet is seen which is not unusual based on the reported NMR spectra of similar cis-$M(CO)_4(PR_3)_2$ (M = Cr, R = Bu; M = W, R = Et) systems[11].

2.3 Discussion

Based on phosphine substitutions for other group 8 $M(CO)_4$(alkyne) complexes[1], it was expected that only CO ligands would be displaced in $Os(CO)_4$(BTMSA), and this, in fact, was observed. The lack of alkyne displacement shows that BTMSA has a labilizing effect on the CO ligands, much like that observed with other alkynes[1]. While the substitution reaction is similar to that for other alkynes, qualitatively the reaction is much slower. Apparently, the steric bulk of the BTMSA ligand plays a role in the reduced substitutional lability of this compound.

Other osmium-alkyne systems, where the alkyne is electron rich, are known to insert CO into the metal-alkyne bond during the second substitution step[2]. $Os(CO)_4$(BTMSA) does not insert CO which again could be due to the steric bulk of BTMSA.

In contrast to the osmium system, $W(CO)_5$(BTMSA) undergoes both CO and alkyne displacement. At low temperatures, it is possible to isolate the mono CO-substituted product cleanly, albeit slowly. This indicates that the alkyne does have a labilizing influence on the CO ligands with respect to $W(CO)_6$, as observed

with the group 8 metal-alkyne complexes. However, at room temperature, alkyne elimination is also observed and is the major product formed with the second PMe_3 substitution. Therefore, it is evident that 4e⁻ destabilization is more of a problem in the group 6 metal-alkyne compounds, resulting in alkyne lability; this has been noted in previous work done with the chromium triad alkyne species[3,4,12,13].

As a result of the alkyne's labilizing effect, substitution in $W(CO)_5$(BMTSA) is expected to occur cis to the alkyne ligand, and this is indeed

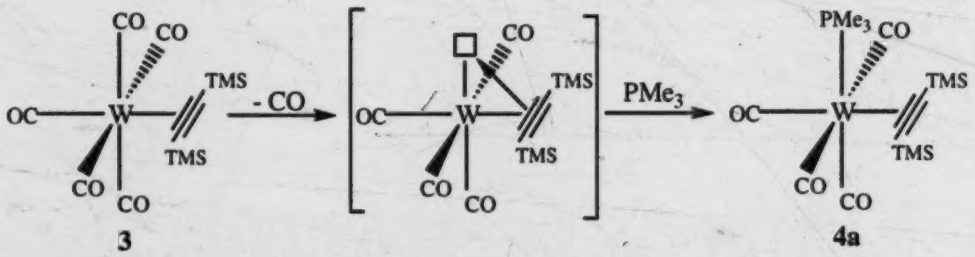

Figure 2-2. Pathway for the First Phosphine Substitution in $W(CO)_5$(BTMSA)

what is observed (Figure 2-2). The increase in 4e⁻ destabilization due to the PMe_3 ligand in **4a** is apparently sufficient in this case to cause BTMSA dissociation and formation of cis-$W(CO)_4(PMe_3)_2$ (Figure 2-3). The formation of **4c** is expected on the basis of the electronic argument, two π-acidic carbonyls trans to PMe_3, although with larger phosphines steric effects will be more important and trans-PR_3 species may be common.

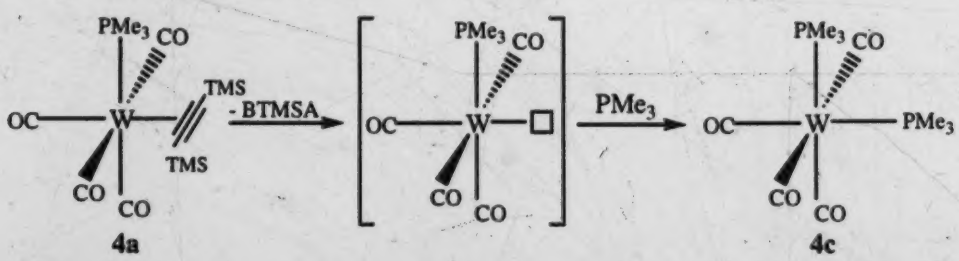

Figure 2-3. Pathway for the Second Phosphine Substitution in $W(CO)_5$(BMTSA)

2.4 Conclusions

CO labilization by the alkyne ligand, BTMSA, is observed in both the d^8 and d^6 systems; in this sense the two metal triads behave in a similar manner. However, in the d^6 complexes, the alkyne ligand is also labile and can be easily substituted, resulting in a more varied product distribution. From the study of $Os(CO)_4$(BTMSA), it is clear that in describing the enhancement in the rate of CO substitution, not only electronic but steric effects of the alkyne ligand must be considered; indeed the compound undergoes substitution more slowly than other $Os(CO)_4$(alkyne) complexes. Not surprisingly, this decrease in substitution lability is accompanied by an increase in the thermal stability of the compound.

2.5 Experimental Section

2.5.1 Solvents and General Techniques

Pentane and hexane were pretreated sequentially with sulfuric acid, aqueous solution of sodium bicarbonate, and distilled water before being dried over magnesium sulfate and distilled from calcium hydride. Benzene was dried and distilled from potassium metal. The deuterated solvents used for NMR were degassed by freeze-pump-thaw cycles and stored over molecular sieves under nitrogen.

Glassware was pretreated with a KOH/ethanol (95%) solution followed by a dilute HCl solution and then rinsed in distilled water and dried at 300 °C overnight. All reactions were carried out under a nitrogen atmosphere using standard Schlenk techniques. The nitrogen was purified by passing it through a heated (100 °C) column of BASF Cu catalyst (R3-11) to remove trace oxygen and a column of Mallinkrodt Aquasorb (P_2O_5 on an inert support) to remove traces of water.

2.5.2 Physical Measurements

Infrared spectra were recorded on a Bomem MB-100 Fourier transform spectrometer over the range 1600 - 2200 cm^{-1} using a 0.5 mm solution cell with KCl plates. The ^{1}H, ^{13}C, and ^{31}P NMR spectra were recorded on a Bruker AM-400 and a Bruker AM-300 spectrometer using toluene – d_8 for the solvent.

2.5.3 Photochemical Techniques

The photolysis reaction for $W(CO)_5$(BTMSA) was carried out in an immersion well that had an outside cooling jacket and a cooling insert for the lamp. The light source used was a Phillips HPK 125W mercury vapor lamp, which was cooled with water running through the immersion well. A pyrex filter ($\lambda \geq 300$ nm) was used to control the radiation wavelength.

The photochemical preparation of $Os(CO)_4$(BTMSA) used an immersion well that had a cooling insert to cool the lamp, but the sample was not cooled. The same radiation source was used in conjunction with a GWV (Glasswerk Wertheim) filter to cut off the light at $\lambda \leq 370$ nm.

More details on the immersion well apparatus can be found in reference 14.

2.5.4 Starting Materials and Reagents

PMe_3 was purchased from Aldrich Chemical Co., BTMSA from Strem Chemicals Inc., $W(CO)_6$ from Climax Molybdenum Company, and $Os_3(CO)_{12}$ from PGM Chemicals (Pty) Ltd. . All compounds were used without further purification.

2.5.5 Synthetic Procedures

Synthesis of $Os(CO)_4(BTMSA)$ (**1**)

BTMSA (5mL, $2.21x10^{-2}$ mol) was added to a solution of $Os_3(CO)_{12}$ (1.450g, $1.60x10^{-3}$ mol) in 120 mL of benzene in the immersion well. The solution was irradiated for 32 hours while stirring and maintaining a slow nitrogen purge. The solution was transferred from the well via cannula and the solvent was then removed under vacuum; the excess $Os_3(CO)_{12}$ was recovered (0.845g). The remaining brown solid was sublimed at 40 °C onto a dry ice probe. The yellow solid collected from the probe was dissolved in a minimal amount of pentane and recrystallized (0.169g, 18%).

IR (pentane, cm^{-1}) ν_{CO}: 2099(w), 2016(vs), 2003(m), 1976(s); $\nu_{C\equiv C}$: 1809(w)

Reaction of $Os(CO)_4(BTMSA)$ of PMe_3

In a 3-neck, 100mL, round-bottom flask equipped with a reflux condenser, $Os(CO)_4(BTMSA)$ (43mg, $9.14x10^{-5}$ mol) was dissolved in 30 mL of hexane. One equivalent (**2a**) or 2.2 equivalents (**2b**) of PMe_3 were added. The solution was stirred while being heated at 35 °C. Once the reaction was complete (by IR) the solvent was removed under vacuum to produce a cream-yellow solid (**2a** or **2b**). The solid was dried under vacuum and not purified further.

2a:

Yield: (0.023g, 34%)

Anal. Calcd for $C_{14}H_{27}O_3OsPSi_2$: C, 32.29; H, 5.23. Found: C, 32.47; H, 5.37.

IR (pentane, cm^{-1}) ν_{CO} : 2036(m), 1959(m), 1933(m); $\nu_{C\equiv C}$: not observed

^1H NMR: 0.79 (d, $^2J_{PH}$ = 9.5 Hz, PMe_3), 0.29 (s, TMS)

$^{31}P\{^1H\}$ NMR: -53.17 (s)

$^{13}C\{^1H\}$ NMR: 192.16 (d, $^2J_{PC}$ = 9.8 Hz, 2 CO), 180.34 (d, $^2J_{PC}$ = 107.2 Hz, 1 CO), 109.0 (s, C≡C), 16.8 (d, $^1J_{CP}$ = 35.0 Hz, PMe_3), 0.57 (s, TMS)

2b:

Yield: (0.021g, 26%)

Anal. Calcd for $C_{16}H_{36}O_2OsP_2Si_2$: C, 33.79; H, 6.38. Found: C, 33.75; H, 6.68.

IR (pentane, cm^{-1}) ν_{CO}: 1947(s), 1888(s); $\nu_{C\equiv C}$: not observed

^1H NMR: 1.02 (t, $^2J_{PH}$= 3.5 Hz, PMe_3), 0.33 (s, TMS)

$^{13}P\{^1H\}$ NMR: -49.71 (s)

$^{13}C\{^1H\}$ NMR: 197.0 (t, $^2J_{PC}$ = 9.8 Hz, 2 CO), 124.6 (s, C≡C), 18.7 (t, $^1J_{PC}$ = 17 Hz, PMe_3), 1.81 (s, TMS)

Synthesis of $W(CO)_5$(BMTSA) (**3**)

BTMSA (4mL, $1.77x10^{-2}$ mol) was added to a solution of $W(CO)_6$ (417 mg, $1.19x10^{-3}$ mol) in 90 mL of pentane in the immersion well. The solution was irradiated for 3-4 hours (until most of the $W(CO)_6$ had reacted), while maintaining a slow nitrogen purge. The solution was transferred via cannula and the solvent was removed under vacuum to leave a flaky yellow solid. The excess BTMSA and remaining $W(CO)_6$ were sublimed at 30 - 40 °C and the solid dissolved in pentane and recrystallized at -80 °C. Yellow crystals of **3** were isolated (0.363 g, 62% yield).

IR (pentane, cm^{-1}) ν_{CO}: 2079.9, 1960.6, 1953.6, 1938.9; $\nu_{C\equiv C}$: not observed

Reaction of $W(CO)_5$(BMTSA) with PMe_3

To a solution of $W(CO)_5$(BTMSA) (35.2 mg, $7.12x10^{-5}$ mol) in 30 mL of pentane PMe_3 (8 μL) was added. The reaction mixture was left at -40 °C until only a minor amount of starting material was left (2 months). After removing the

solvent under vacuum, the solid was dissolved in a minimal amount of pentane and recrystallized at -80 °C. Yellow blocks of **4a** were recovered.

IR (pentane, cm^{-1}) ν_{CO}: 2024.6(m), 1932.3(m), 1914.97(s), 1886(m)
^{1}H NMR: 0.72 (d, $^{2}J_{PH}$ = 7.5 Hz, PMe_3), 0.30 (s, TMS)
$^{31}P\{^{1}H\}$ NMR: -36.99 (s, $^{1}J_{PW}$ = 226.8 Hz)
$^{13}C\{^{1}H\}$ NMR: not enough sample available

Characterization of $W(CO)_5(PMe_3)$(**4b**)

IR (pentane, cm^{-1}) ν_{CO}: 2070.7(w), 1948.9(m), 1939(s)
literature values (hexane, cm^{-1})[15] ν_{CO}: 2066, 1943, 1933

Reaction of $W(CO)_5$(BTMSA) with Excess PMe_3

To a solution of $W(CO)_5$(BTMSA) (35.4 mg, $7.16x10^{-5}$ mol) in 30 mL of pentane PMe_3 (30 µL, $2.90x10^{-4}$ mol) was added. The solution was stirred at room temperature for 8 hours, maintaining a slow nitrogen purge. A cream-colored solid (**4c**) was recovered after removing the solvent under vacuum and drying the residue under vacuum.

IR (pentane, cm^{-1}) ν_{CO}: 2015.4(s), 1916(s), 1895(vs)
^{1}H NMR: 0.98 (d, $^{2}J_{PH}$ = 7 Hz, PMe_3)
$^{31}P\{^{1}H\}$ NMR: -39.71 (s, $^{1}J_{PW}$ = 222.2 Hz)
$^{13}C\{^{1}H\}$ NMR: 206.57 (t, $^{2}J_{CP}$ = 7.6 Hz, 2 CO), 203.5 (t, $^{2}J_{CP}$ = 8.4 Hz, 2 CO),
21.7 (m, $^{1}J_{CP}$ = 15.2 Hz, $^{3}J_{CP}$ = 12.7 Hz, $^{2}J_{CW}$ = 12.6 Hz, $P(CH_3)_3$)

2.6 References

1. Pearson, J.; Cooke, J.; Takats, J.; Jordan, R. B. *J. Am. Chem. Soc.* **1998**, *120*, 1434 and references therein.

2. Mao, T. -F. Ph.D. Thesis, University of Alberta., 1996.

3. Stolz, J. W.; Dobson, G. R.; Sheline, R. K. *Inorg. Chem.* **1963**, *2*, 1264.

4. Fischer, H.; Volkland, H.-P.; Früh, A.; Stumpf, R. *J. Organomet. Chem.* **1995**, *491*, 269.

5. Jacké, J. PhD. Thesis, Universität-Gesamthochschule-Duisburg, 1989.

6. Tate, D. P.; Augl, J. M.; Ritchey, W. M.; Ross, B. L.; Grasselli, J. G. *J. Am. Chem. Soc.* **1964**, *86*, 3261.

7. Ball, R. G.; Burke, M. R.; Takats, J. *Organometal.* **1987**, *6*, 1918.

8. Rossi, A. R.; Hoffmann, R. *Inorg. Chem.* **1975**, *14*, 365.

9. Harris, R. K. *Can. J. Chem.* **1964**, *42*, 2275.

10. Koemm, U.; Kreifer, C. G.; Strack, H. *J. Organomet. Chem.* **1978**, *148*, 179.

11. Bodner, G. M. *Inorg. Chem.* **1975**, *14*, 2694.

12. Landon, S. J.; Shulman, P. M.; Geoffroy, G. L. *J. Am. Chem. Soc.* **1985**, *107*, 6739.

13. Birdwhistell, K. R.; Tonker, T. L.; Templeton, T. L. *J. Am. Chem. Soc.* **1987**, *109*, 1401.

14. Grevels, F. –W.; Reuvers, J. G. A.; Takats, J. In *Inorg. Syn.* **1986**, *24*, 176.

15. Koemm, U.; Kreiter, C. G.; Strack, H. *J. Organomet. Chem.* **1978**, *148*, 179.

Chapter Three

Theoretical Investigation of the Metal-Alkyne Interaction in $Os(CO)_x(C_2R_2)$ (x = 3,4) and $W(CO)_x(C_2R_2)$ (x = 4,5) Complexes

3.1 Introduction

With modern developments in theory and computational models, and with increased computing power it is not unusual in the literature for an experimental study to include a theoretical component in the research. The calculations are used to help elucidate the experimental observations and to supply the conceptual framework for the analysis of such results. In addition, calculations allow for probing the facets of the chemical process inaccessible to experiment, for example, the structure of the transition state in a reaction.

To complement the phosphine substitution study on the tungsten and osmium BTMSA systems, the geometry and electronic structure of a series of alkynes and metal-alkynes were calculated (Scheme 3-1). Due to the large number of atoms involved, phosphine substituted derivatives were not studied. Rather, the focus was on comparing the metal-alkyne interaction between the tungsten and osmium complexes.

Scheme 3-1. Alkynes and Transition Metal Complexes Studied

	$Os(CO)_5$		$W(CO)_6$	
Butyne	$Os(CO)_4$(butyne)	$Os(CO)_3$(butyne)	$W(CO)_5$(butyne)	$W(CO)_4$(butyne)
HFB	$Os(CO)_4$(HFB)	$Os(CO)_3$(HFB)	$W(CO)_5$(HFB)	$W(CO)_4$(HFB)
BSA	$Os(CO)_4$(BSA)	$Os(CO)_3$(BSA)	$W(CO)_5$(BSA)	$W(CO)_4$(BSA)
BTMSA	$Os(CO)_4$(BTMSA)	$Os(CO)_3$(BTMSA)	$W(CO)_5$(BTMSA)	$W(CO)_4$(BTMSA)

3.2 Computational Details

All of the complexes were studied with Density Functional Theory (DFT) as found in the Gaussian 94 program[1]. The B3LYP functional was used, which is comprised of Becke's 3-parameter exchange functional (B3)[2] and the correlation functional of Lee, Yang, and Parr (LYP)[3]. The compact effective core potentials (ECP) of Stevens *et al.*[4] were used to help minimize the computational effort required. The mixed valence basis was used without additional polarization functions for both W and Os since it effectively has two p-type polarization functions inherent in the p space for both metals. For hydrogen, Huzinaga's uncontracted (3s) basis set[5] was used while the DZV basis provided with the ECP was contracted to give a SZV basis for fluorine. Both the DZV basis (4-1) and a TZV basis (3-11) uncontracted from the DZV basis were used for C, O, and Si. Table 3-1 lists the polarization functions that were used in the basis sets.

Table 3-1. Polarization Functions Used in the Basis Sets

Basis Set	Polarization Function Exponents[6]				Description
	Carbon	Oxygen	Silicon	Fluorine	C,O,Si/H,F
D1	0.6	1.154	0.262	---	DZV/SZV
D2	0.288 1.335	0.535 2.704	0.118 0.424	1.496	DZV/SZV
T1	0.6	1.154	0.262	---	TZV/SZV
T2	0.288 1.335	0.535 2.704	0.118 0.424	1.496	TZV/SZV

As the main focus of this study was the metal-alkyne interaction, it was possible to use a minimal description (basis) for hydrogen and fluorine since they are not directly involved in the bonding.

3.3 Results and Discussion

3.3.1 Free Alkynes

The geometries of the alkynes were calculated with all four basis sets and compared to experiment (Table 3-2). The X-R bonds do not agree very well with experiment, which is to be expected since small basis sets were used for fluorine and hydrogen. For all of the alkynes, the C≡C bond shortens as the basis set is changed (i.e. D1 to T2) and ultimately is smaller than experiment (BSA is slightly longer). The alkyne-silicon bond length in BSA and BTMSA is longer than experiment with the D2 basis set giving the best agreement (shortest bond length).

Table 3-2. Bond Lengths (Å) and Angles (°) in the Free Alkynes

	C≡C	C-X	X-R	C-X-R	Rel. Energy (kcal/mol)
Butyne		X=C	R=H		
D1	1.253	1.487	1.110	111.8	46.1
D2	1.228	1.481	1.106	111.7	38.7
T1	1.210	1.467	1.105	111.1	0.4
T2	1.207	1.466	1.103	111.0	0
Expt.[7] (r_a)[a]	1.2135(13)	1.4675(13)	1.1160(6)	110.7(4)	---
HFB		X=C	R=F		
D1	1.244	1.475	1.399	111.6	79.8
D2	1.221	1.476	1.377	111.3	28.2
T1	1.201	1.458	1.390	111.5	49.5
T2	1.198	1.468	1.360	111.1	0
Expt.[8] (r_g)[a]	1.204(4)	1.478(4)	1.334(2)	110.7(1)	---
BSA		X=Si	R=H		
D1	1.264	1.849	1.535	109.7	40.5
D2	1.238	1.837	1.514	109.4	15.8
T1	1.223	1.846	1.524	109.5	20.7
T2	1.220	1.840	1.497	109.2	0
Expt.[9] (r_α°)[a]	1.2160(13)	1.8077(8)	1.4834(17)	109.65(39)	---
BTMSA		X=Si	R=C		
D1	1.263	1.866	1.898	108.9	36.9
D2	1.238	1.851	1.889	108.4	16.2
T1	1.226	1.862	1.892	108.6	15.1
T2	1.221	1.852	1.883	108.5	0
Expt.[10] (r_α)[a]	1.233(3)	1.813(3)	1.852(1)	108.6(3)	---
Expt.[11] (x-ray)	1.208(3)	1.844(1)	1.856(2)	108.2(6)	---

[a] electron diffraction; r_a derived directly from experiment, r_g is the thermal average value of internuclear distance (real average), r_α° is the distance between average nuclear positions (ground vibrational state), and r_α is the distance between average nuclear positions (thermal equilibrium) (projected average)

The use of larger basis sets and all-electron calculations would produce more accurate calculated geometries, but because of their size and lack of

relativistic effects, these basis sets can not realistically be used with the large metal-alkyne systems. However, the relatively good agreement with experiment observed with these basis sets (D1, D2, T1, and T2) is still an indicator of how reliable the metal-alkyne geometries are.

3.3.2 Parent Carbonyls

The geometries of the parent carbonyls, $Os(CO)_5$ and $W(CO)_6$, were also fully optimized using the four basis sets (Table 3-3). For both species, the CO bond length shortens going from D1 to T2, with the largest difference being between the D2 and T2 basis sets. The CO distance in $W(CO)_6$ agrees quite well with experiment, whereas the osmium-CO bonds are still too long. The metal-carbonyl bonds are too long in both complexes and, interestingly, with $Os(CO)_5$, the axial M-CO bond shows good agreement while the equatorial bond is substantially longer. Overall, basis T2 gives the best agreement. For a comparison of calculated $M(CO)_x$ geometries refer to references 12 and 13.

Table 3-3. Parent Carbonyl Bond Lengths (Å)

$Os(CO)_5$	D1	D2	T1	T2	Expt.[14,15] $(r_a)^a$
$M\text{-}CO_{ax}$	1.982	1.982	1.983	1.985	1.982(20)
$M\text{-}CO_{eq}$	1.971	1.969	1.973	1.973	1.937(19)
CO_{ax}	1.159	1.158	1.147	1.143	1.130(4)
CO_{eq}	1.166	1.164	1.153	1.149	1.130(4)
Rel. Energy[b]	37.5	34.7	9.1	0	----
$W(CO)_6$					
M-CO	2.076	2.075	2.078	2.077	2.058(3)
CO	1.163	1.162	1.151	1.147	1.148(3)
Rel. Energy[b]	44.9	41.3	11.6	0	----

[a] distance between nuclear positions (thermal equilibrium)

[b] in kcal/mol

3.3.3 Metal-Alkyne Complexes

All of the metal-alkyne complexes (Scheme 3-1) were optimized using the D1 basis set with the alkyne occupying an equatorial site. An axial CO was

removed from the saturated metal-alkyne complex and the remaining structure was reoptimized to obtain the CO dissociated product.

Tables 3-4 and 3-5 list the C≡C and M-C bond lengths calculated for the osmium and tungsten complexes, respectively*. For all of the alkynes studied, the bond lengthens upon coordination to the metal, indicating that electron density has been removed from the π orbital to the metal, coupled with π-back donation into the π* orbital from the metal. HFB stands out from the other alkynes with the largest increase in the C≡C bond which can be attributed to its strong π-acidity and, therefore, receives a larger amount of metal d_π electrons through π-back donation than the other alkynes. There is further lengthening of the bond in the CO dissociated, formally 16e⁻ intermediate, suggesting that there is an even stronger interaction between the alkyne and the metal. This is consistent with the notion that the alkyne acts as a 4e⁻ donor ligand, utilizing both sets of π orbitals, and it is further corroborated by the shorter, stronger metal-alkyne bond upon dissociation of CO. It is interesting to note that although the metal-HFB bond is stronger than the other alkynes in the 18e⁻ complexes, the increase in the interaction when going to the CO dissociated intermediate is the smallest for HFB. This is expected from the poorer electron-donating ability of HFB compared to the other alkynes.

Table 3-4. Calculated C≡C and M-C Bond Lengths (Å) in the Osmium-Alkyne Complexes

Alkyne	C≡C Bond Length					M-C Bond Length		
	Free	$Os(CO)_4(\equiv)$	Δ_1	$Os(CO)_3(\equiv)$	Δ_2	$Os(CO)_4(\equiv)$	$Os(CO)_3(\equiv)$	Δ
Butyne	1.253	1.302	**0.049**	1.365	**0.063**	2.230	2.022	**0.208**
HFB	1.244	1.315	**0.071**	1.356	**0.041**	2.162	2.029	**0.133**
BSA	1.264	1.308	**0.044**	1.360	**0.052**	2.257	2.056	**0.201**
BTMSA	1.263	1.301	**0.038**	1.354	**0.053**	2.288	2.066	**0.222**

$\Delta_1 = Os(CO)_4(\equiv) - Free$; $\Delta_2 = Os(CO)_3(\equiv) - Os(CO)_4(\equiv)$; $\Delta = Os(CO)_4(\equiv) - Os(CO)_3(\equiv)$

* Complete geometry of the metal-alkyne complexes is given in the Appendix.

Table 3-5. Calculated C≡C and M-C Bond Lengths (Å) in the Tungsten-Alkyne Complexes

Alkyne	C≡C Bond Length					M-C Bond Length		
	Free	$W(CO)_5(\equiv)$	Δ_1	$W(CO)_4(\equiv)$	Δ_2	$W(CO)_5(\equiv)$	$W(CO)_4(\equiv)$	Δ
Butyne	1.253	1.270	0.017	1.330	0.060	2.435	2.119	0.316
HFB	1.244	1.297	0.053	1.337	0.040	2.251	2.091	0.160
BSA	1.264	1.282	0.018	1.328	0.046	2.429	2.163	0.266
BTMSA	1.263	1.280	0.017	1.321	0.041	2.460	2.192	0.268

Δ_1 = $W(CO)_5(\equiv)$ – Free; Δ_2 = $W(CO)_4(\equiv)$ – $W(CO)_5(\equiv)$; Δ = $W(CO)_5(\equiv)$ – $W(CO)_4(\equiv)$

The M-CO distances are listed in Table 3-6. It can be seen that substitution of a CO by electron rich alkynes shortens the metal-CO bond since there is more electron density at the metal available for back donation to the carbonyls. However, with electron-poor HFB, the metal-CO bond actually lengthens, showing that HFB is effective in competing with the carbonyls for electron density. The CO distances, listed in Table 3-7, show the same trend with shorter CO bonds for the HFB complex and longer CO bonds for the other alkynes; π-back donation into the CO π* orbital decreases its triple bond character and

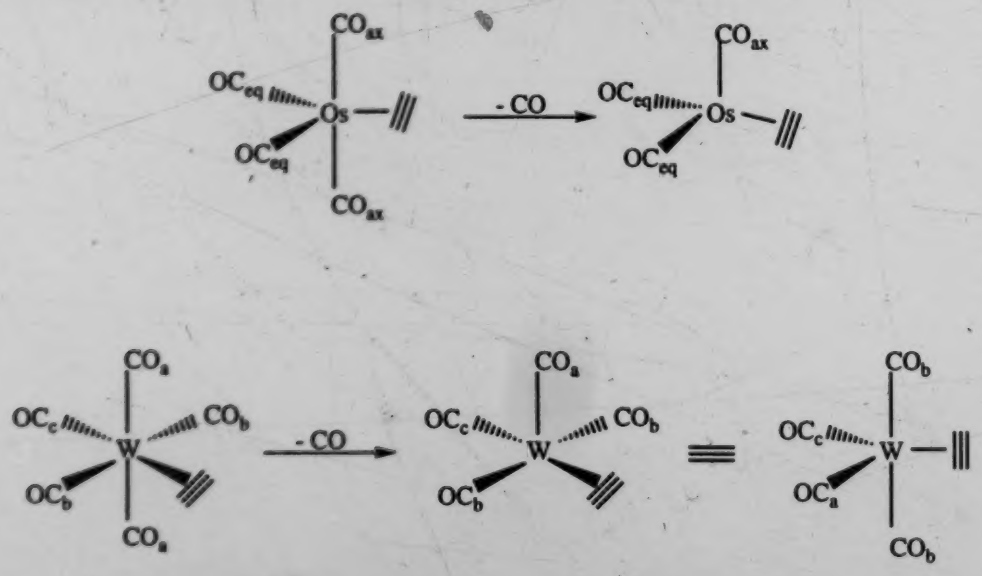

Figure 3-1. Bond Definitions for the Metal-Alkyne Species

lengthens the bond, while conversely, less π-back donation shortens the bond.

Interestingly, upon CO dissociation the axial CO bond length in the osmium systems increases for all of the alkynes while in the tungsten system (CO_b in Table 3-7) it increases minimally for HFB and decreases for the donor alkynes. The equatorial CO's in the osmium systems remain relatively constant, which is not the case for tungsten. There is a significant increase in the CO_a distance whereas the CO_c bond increases marginally. Similarly, there is a large decrease in the axial M-CO distance as CO is removed in the osmium compound and again there are only small changes in the equatorial M-CO distances. With the tungsten systems, the M-CO_b bond shortens for all of the alkynes except butyne, which lengthens by a similar amount. Both the M-CO_a and M-CO_c bonds decrease again with the largest difference being with the CO_a carbonyl. Therefore, it seems that there is more electron donation from the alkyne to the metal center in the 16e$^-$ intermediate and it is donated in such a manner that only the axial CO's (Os), CO_a and CO_c (W) benefit from the increased electron density.

Table 3-6. M-CO Bond Lengths (Å)[a] in the Metal-Alkyne Complexes

Alkyne	CO Bond	$Os(CO)_4(\equiv)$	$Os(CO)_3(\equiv)$	$W(CO)_5(\equiv)$	$W(CO)_4(\equiv)$
Butyne	(ax/a)	1.977	1.899	2.069	2.018
	(eq/b)	1.960	1.958	2.066	2.069
	(c)			2.023	
HFB	(ax/a)	1.995	1.890	2.083	2.022
	(eq/b)	1.973	1.965	2.096	2.089
	(c)			2.064	
BSA	(ax/a)	1.980	1.893	2.072	2.008
	(eq/b)	1.956	1.954	2.071	2.070
	(c)			2.021	
BTMSA	(ax/a)	1.975	1.893	2.070	2.003
	(eq/b)	1.949	1.949	2.065	2.062
	(c)			2.014	
Parent	(ax)	1.982		2.076	
Carbonyls	(eq)	1.971		2.076	

[a] bond definitions shown in Figure 3-1

Table 3-7. CO Bond Lengths (Å)[a] in the Metal-Alkyne Complexes

Alkyne	CO Bond	$Os(CO)_4(\equiv)$	$Os(CO)_3(\equiv)$	$W(CO)_5(\equiv)$	$W(CO)_4(\equiv)$
Butyne	(ax/a)	1.160	1.170	1.166	1.171
	(eq/b)	1.167	1.167	1.165	1.164
	(c)			1.170	
HFB	(ax/a)	1.153	1.165	1.160	1.166
	(eq/b)	1.160	1.160	1.156	1.157
	(c)			1.163	
BSA	(ax/a)	1.159	1.170	1.164	1.171
	(eq/b)	1.166	1.166	1.164	1.164
	(c)			1.170	
BTMSA	(ax/a)	1.161	1.171	1.165	1.173
	(eq/b)	1.168	1.168	1.164	1.162
	(c)			1.171	
Parent	(ax)	1.159		1.163	
Carbonyls	(eq)	1.166		1.163	

[a] bond definitions shown in Figure 3-1

3.3.4 Molecular Orbitals

To gain a better insight into the metal-alkyne interactions, the molecular orbitals of $M(CO)_x$BTMSA (M = Os, W) were visualized using MOLDEN[16]. It was hoped that these molecular orbital diagrams would reveal the source of the extra electron donation from the alkyne in the CO dissociated intermediate. However, even though the D1 basis set is not very large, the molecular orbitals had extensive orbital mixing and were very complex, making it difficult to isolate specific metal-alkyne interactions.

Fortunately, X-ray structure data were available for both $Os(CO)_4$(BTMSA)[17] and $W(CO)_5$(BTMSA)[18] complexes, allowing a basis set comparison with experiment. From the comparison, the best geometry could then be used in a minimal basis set single point calculation (MINI basis set[19]) to obtain much simpler molecular orbital pictures.

With both tungsten and osmium, the T2 basis gave the best overall geometry (Tables 3-8 and 3-9) which was then used in the single point calculations. Again, MOLDEN[16] was used to visualize the molecular orbitals, which are shown in Figures 3-2 to 3-5. For the 18-electron $Os(CO)_4$(BTMSA) and $W(CO)_5$(BTMSA) compounds the molecular orbital pictures provide a nice corroboration of the expectations from the Dewar-Chatt-Duncanson bonding model. Forward donation from the filled $\pi_{\parallel}$ orbital to the empty metal d_{π} can easily be seen in Figure 3-2(a), back bonding into the empty alkyne $\pi_{\parallel}^*$ orbital is shown in Figure 3-3(a). Although there is proper symmetry for overlap between the alkyne's filled $\pi_{\perp}$ orbital and the metal d_{π}, Figure 3-2(b), the metal d_{π} is also fully occupied and there are the accompanying antibonding molecular orbitals representing the $4e^-$ destabilization in these metal-alkyne systems. Finally, Figure 3-3(b) shows the metal $d_{\pi} \rightarrow \pi_{\perp}^*$ back bonding component, where the δ symmetry is evident as is the minor importance of this interaction.

Table 3-8. $Os(CO)_4$(BTMSA) Calculated and Experimental Geometry

	D1	D2	T1	T2	Experiment[17]
Bond Length (Å)					
$M\text{-}CO_{ax}$	1.975	1.975	1.976	1.979	1.93(1)
$M\text{-}CO_{eq}$	1.949	1.947	1.950	1.952	1.895(1)
CO_{ax}	1.161	1.160	1.149	1.144	1.165(1)
CO_{eq}	1.168	1.167	1.156	1.151	1.145(1)
M-C	2.288	2.289	2.297	2.286	2.259(9)
C≡C	1.301	1.287	1.275	1.273	1.28(1)
C-X	1.880	1.865	1.875	1.864	1.836(9)
X-R	1.90	1.89	1.89	1.89/1.88	1.86(1)
Angle (°)					
$C_{ax}\text{-}M\text{-}C_{ax}$	171.2	171.6	171.8	171.9	172.9(4)
$C_{eq}\text{-}M\text{-}C_{eq}$	106.9	106.8	107.5	106.5	108.6(4)
C-M-C	33.0	32.6	32.2	32.3	32.9(3)
C-C-X	153.6	153.1	154.2	152.3	---
C-X-R	108.4/108.1	108.0/107.9	108.2/108.0	108.1/108.0	---
Energy (kcal/mol)	61.7	41.4	23.9	0	---

Table 3-9. $W(CO)_5$(BTMSA) Calculated and Experimental Geometry

	D1	D2	T1	T2	Experiment[18]
Bond Length (Å)					
$M\text{-}CO_{ax}$	2.070	2.069	2.072	2.073	2.046(4)
$M\text{-}CO_{eq1}$	2.065	2.064	2.068	2.068	2.042(4)
$M\text{-}CO_{eq2}$	2.014	2.011	2.013	2.014	1.967(4)
CO_{ax}	1.165	1.164	1.153	1.149	1.136(5)
CO_{eq1}	1.164	1.165	1.154	1.150	1.142(5)
CO_{eq2}	1.171	1.170	1.159	1.155	1.162(5)
M-C	2.460	2.470	2.484	2.475	2.433(4)
C≡C	1.280	1.265	1.253	1.250	1.239(5)
C-X	1.891	1.875	1.885	1.874	1.864(4)
X-R	1.90/1.89	1.89/1.88	1.89	1.88	----
Angle (°)					
$C_{eq}\text{-}M\text{-}C_{eq}$	174.7	175.8	175.3	176.7	175.6(2)
$C_{eq}\text{-}M\text{-}C_{eq}$	165.7	166.1	166.1	166.5	164.4(2)
C-M-C	30.2	29.7	29.2	29.3	----
C-C-X	152.2	152.4	152.8	152.0	153.7(3)
C-X-R	106.2/109.0	105.7/109.0	105.9/109.0	105.8/109.0	----
Energy (kcal/mol)	69.6	43.4	26.5	0	----

The molecular orbital pictures of $W(CO)_4$(alkyne) also clearly show the $4e^-$ donor alkyne moiety. As mentioned in Chapter One, the bonding capabilities of $M(CO)_x$ fragments have been analyzed by Hoffmann, where the d^6 C_{2v} $M(CO)_4$ fragment has two empty orbitals having proper symmetry to accept two electrons each from the alkyne's $\pi_{\parallel}$ and $\pi_{\perp}$ molecular orbitals, respectively. To accomplish this the alkyne should occupy an equatorial position of a trigonal bipyramid but instead of being in-plane, as in the d^8 $Os(CO)_4$(BTMSA) complex, it will lie perpendicular to it. Indeed, this is seen in Figure 3-4; the back bonding components are shown in Figure 3-5. A similar conclusion has been reached by Wink[20] on the basis of extended Hückel calculations. Wink also found that the molecular structure of $Cr(CO)_2(P(OMe_3))_2(\eta^2$ - PhC≡CPh) conforms to the above prediction: axial $P(OMe_3)$ ligands with the alkyne ligand lying almost in the P-Cr-P plane, perpendicular to the equatorial plane of the trigonal bipyramid which contains the two CO ligands. The current calculations mirror these findings, as shown in Figure 3-6.

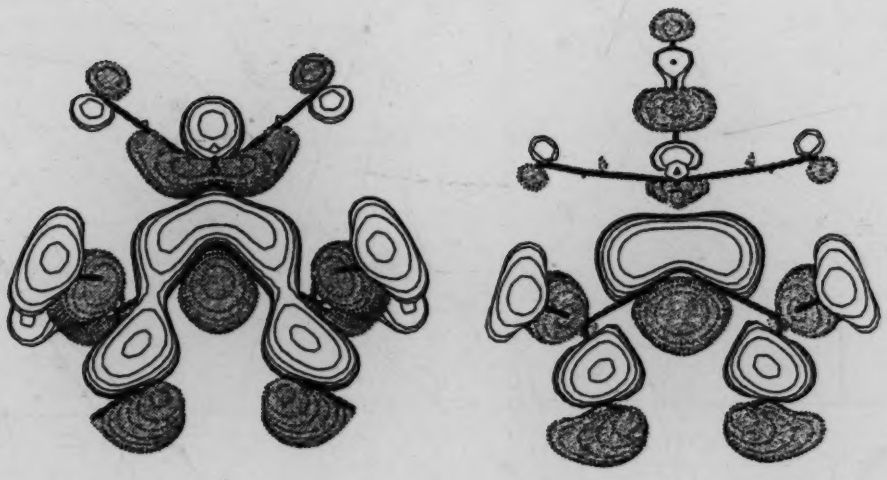

(a)

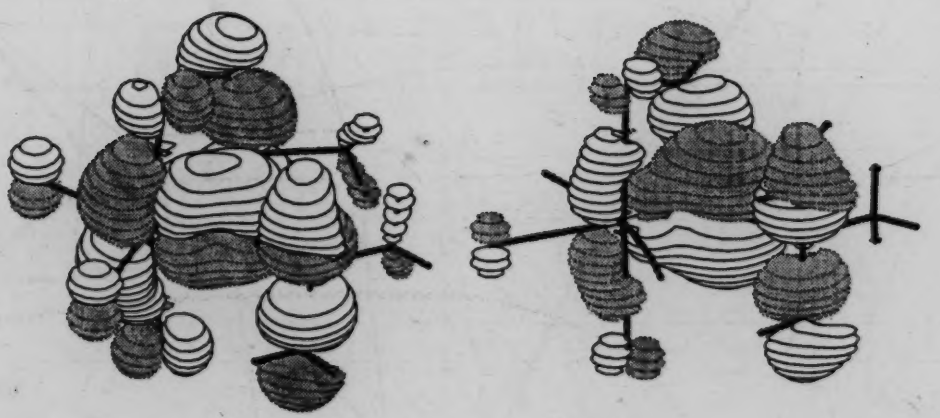

(b)

$Os(CO)_4(BTMSA)$ $W(CO)_5(BTMSA)$

Figure 3-2. Molecular Orbitals of $Os(CO)_5(BTMSA)$ and $W(CO)_5(BTMSA)$; Donation From Filled Alkyne π Sets (a) $\pi_{\parallel} \rightarrow M\, d_{\pi}$, (b) $\pi_{\perp} \rightarrow M\, d_{\pi}$

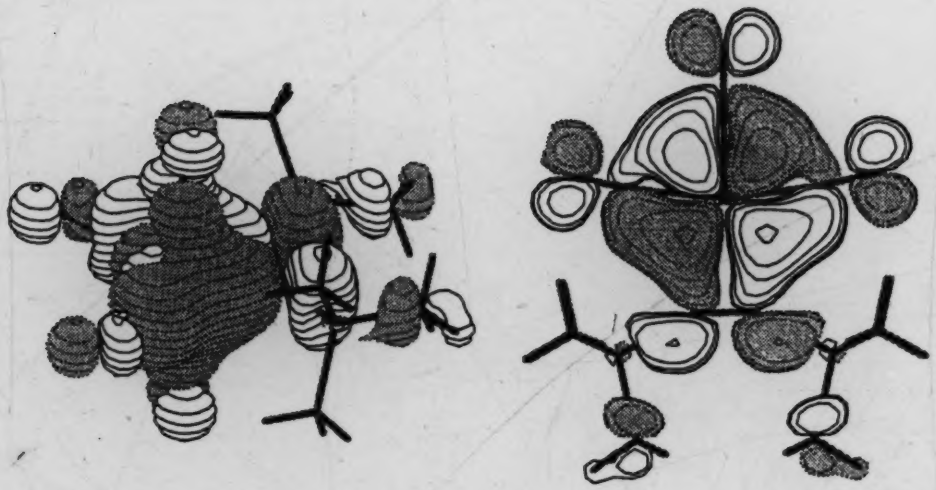

(a)

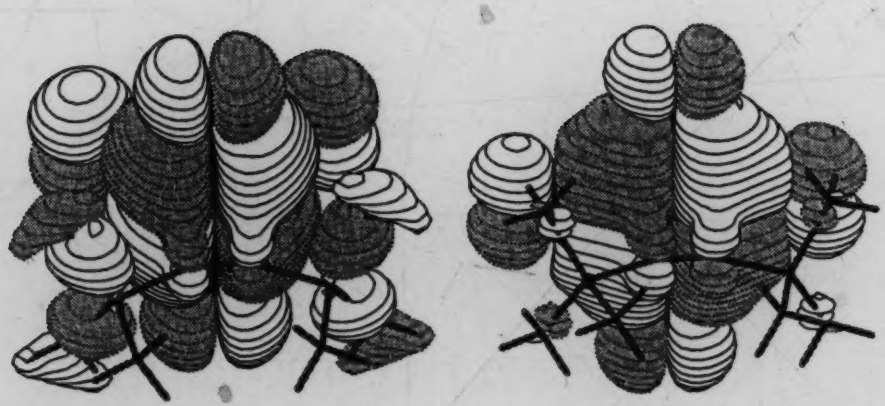

(b)

$Os(CO)_4(BTMSA)$ $W(CO)_5(BTMSA)$

Figure 3-3. Molecular Orbitals of $Os(CO)_4(BTMSA)$ and $W(CO)_5(BTMSA)$; Bac

Donation From Filled M d_π (a) M $d_\pi \rightarrow \pi_\parallel^*$, (b) M $d_\pi \rightarrow \pi_\perp^*$

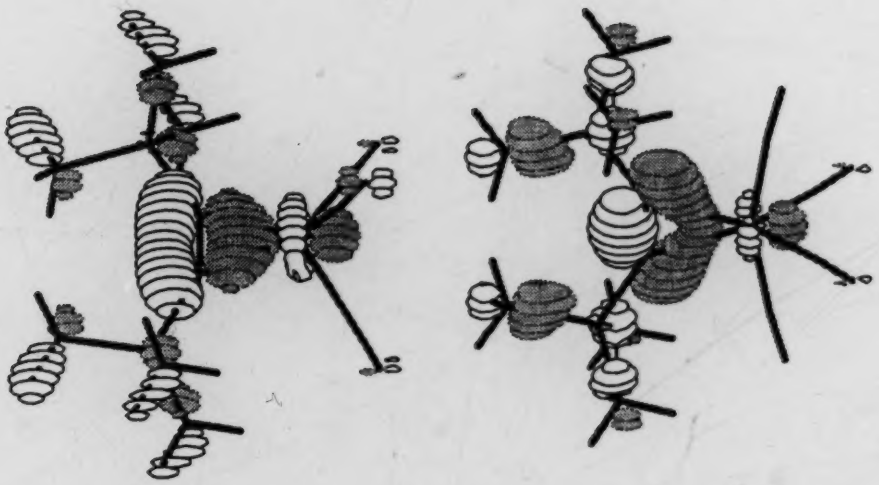

(a)

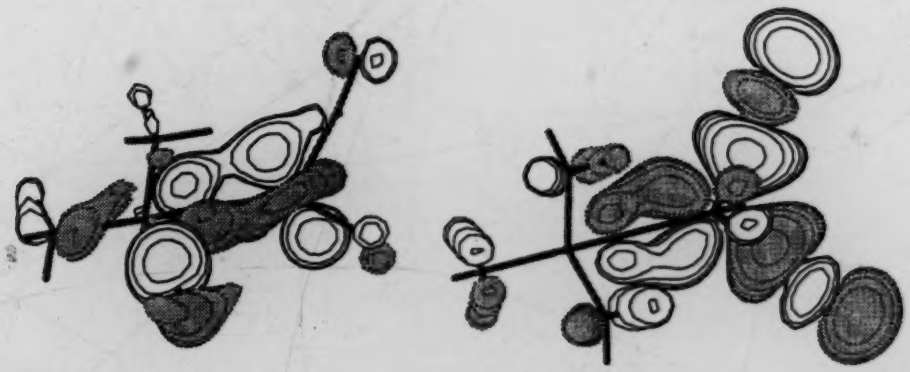

(b)

$Os(CO)_3(BTMSA)$ $W(CO)_4(BTMSA)$

Figure 3-4. Molecular Orbitals of $Os(CO)_3(BTMSA)$ and $W(CO)_4(BTMSA)$; Donation From Filled Alkyne π Sets (a) $\pi_{\parallel} \rightarrow M\, d_{\pi}$, (b) $\pi_{\perp} \rightarrow M\, d_{\pi}$

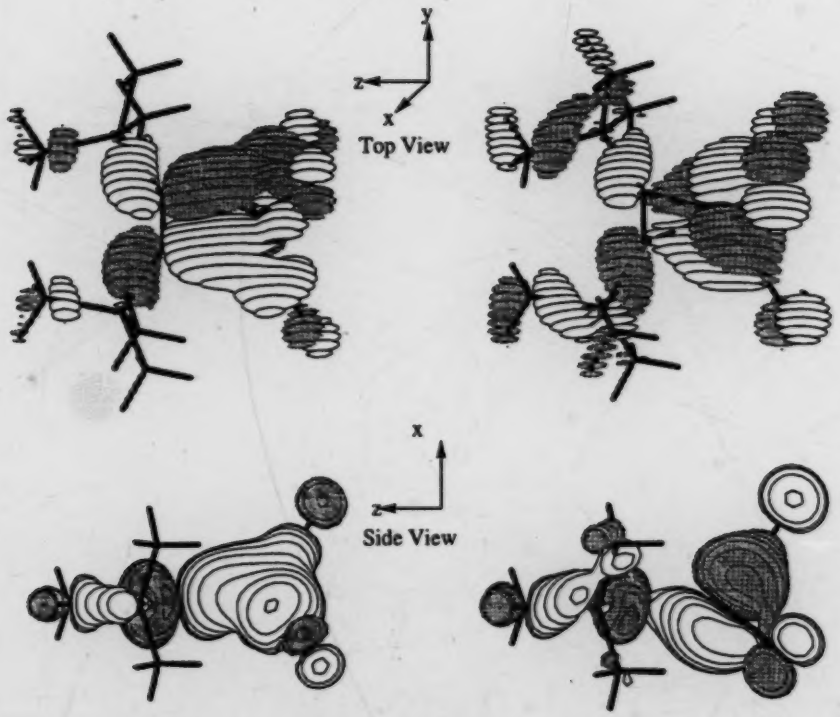

$Os(CO)_3(BTMSA)$

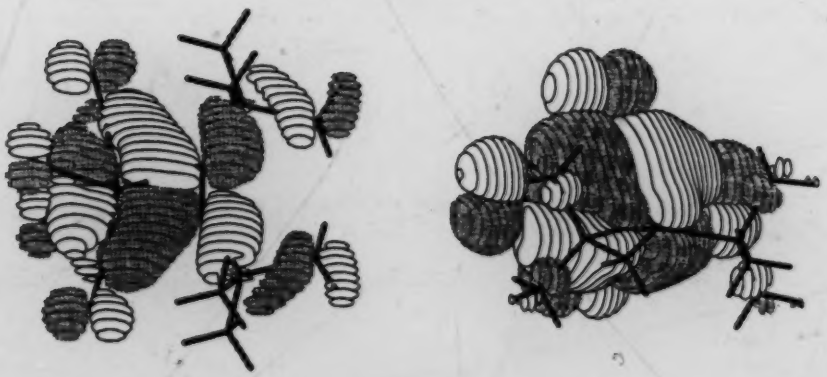

$W(CO)_4(BTMSA)$

(a) (b)

Figure 3-5. Molecular Orbitals of $Os(CO)_3(BTMSA)$ and $W(CO)_4(BTMSA)$; Bacl

Donation From Filled M d_π (a) M $d_\pi \rightarrow \pi_\parallel^*$, (b) M $d_\pi \rightarrow \pi_\perp^*$

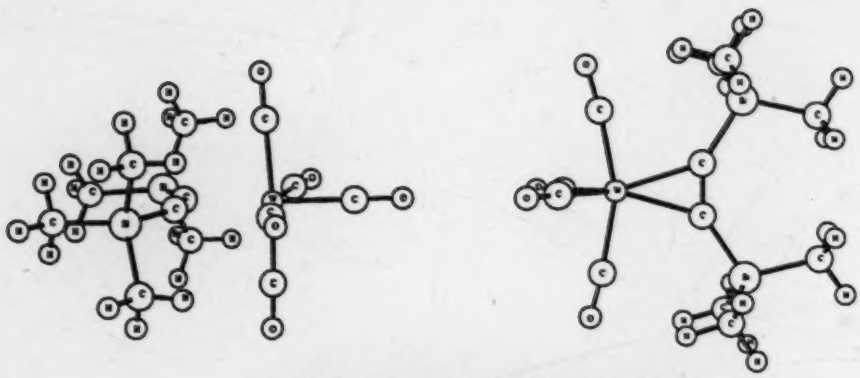

Figure 3-6. Calculated Geometries of $W(CO)_5$(BTMSA) and $W(CO)_4$(BTMSA)

The bonding interactions are more difficult to visualize in the $Os(CO)_3$(BTMSA) compound due to the extensive mixing of orbitals. Nevertheless, the alkyne is again clearly acting as a 4e⁻ donor. As shown in Figure 3-7, loss of a CO ligand from $Os(CO)_4$(BTMSA) results in a "bending down" of the alkyne ligand from the equatorial plane of the trigonal bipyramid towards the site vacated by the dissociated CO ligand. Forward donation (Figure 3-4) is into the approximate metal d_{z^2} orbital from the alkyne $\pi_{\parallel}$ orbital, whereas $\pi_{\perp}$ orbital donates into a metal orbital which has undergone substantial mixing. Using the coordinate system provided, the metal d_{xy} orbital π-back donates into $\pi_{\perp}^*$ with the majority of the overlap involving the lower orbital lobes on BTMSA. Similarly, back donation into $\pi_{\parallel}^*$ originates from the d_{yz} orbital. With $Os(CO)_3$(BTMSA),

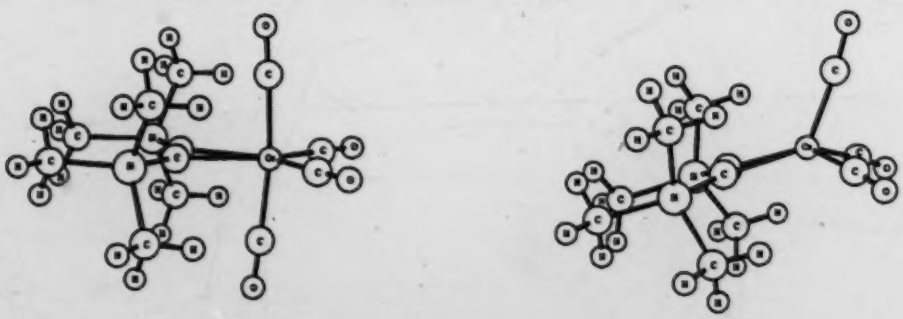

Figure 3-7. Calculated Geometries of $Os(CO)_4$(BTMSA) and $Os(CO)_3$(BTMSA)

the π-back donation into the $\pi_{\parallel}^*$ and $\pi_{\perp}^*$ orbitals is analogous to that observed in $M(CO)_3(C_2H_2)$ (M = Fe, Ru, and Os)[12] and $Ru(CO)_4(HFB)$[21].

3.3.5 Fragment Molecular Orbital Analysis

Using the program YAeHMOP[22], fragment molecular orbital analyses using optimized geometries were carried out. The effect of the alkyne on the metal-alkyne interaction was assessed; Figures 3-8 and 3-9 show the interaction diagrams for the HFB and BTMSA species, representatives of π-acidic and π-donor alkynes. HFB has a larger π-back donation interaction with osmium and tungsten than BTMSA does, which is expected based on the nature of the two alkynes. As for donation from the $\pi_{\parallel}$ orbital, it appears that HFB is the better donor, contradictory to its π-acidic nature. There is a smaller energy difference between the alkyne's $\pi_{\perp}$ orbital and the metal's a_1 orbital for BTMSA, but the resultant stabilization in the metal-alkyne complex orbital is larger for HFB. However, in both of the species, BTMSA is farther from the metal center than HFB is, which will result in a weaker metal-alkyne interaction due to the smaller amount of orbital overlap.

3.3.6 Energies Calculated for Alkyne Addition and CO Dissociation in the Metal-Carbonyl Complexes

Using the molecular energies obtained from the calculated geometries with the D1 basis set, ΔE for the following reactions was calculated.

$$Os(CO)_5 + \text{alkyne} \longrightarrow Os(CO)_4(\text{alkyne}) + CO \qquad (3\text{-}1)$$

Table 3-10. Energetics Calculated for the Reaction Shown in Eq. (3-1)

Alkyne	ΔE (rxn) basis D1 (kcal/mol)	ΔE (rxn) basis T2 (kcal/mol)
Butyne	0.16	31.07
HFB	-18.70	---
BSA	0.63	---
BTMSA	2.42	5.86

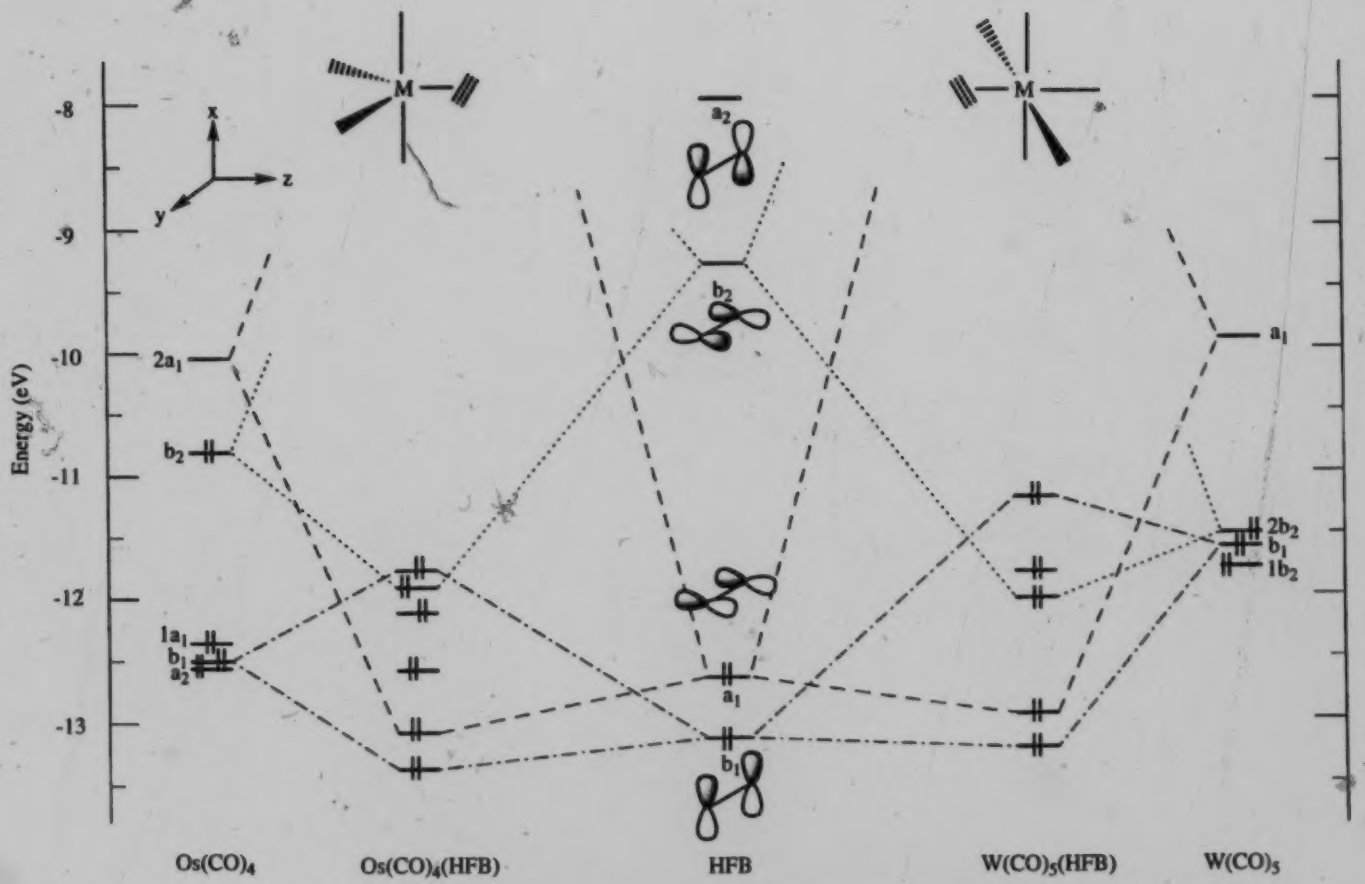

Figure 3-8. Molecular Orbital Interaction Diagram for HFB

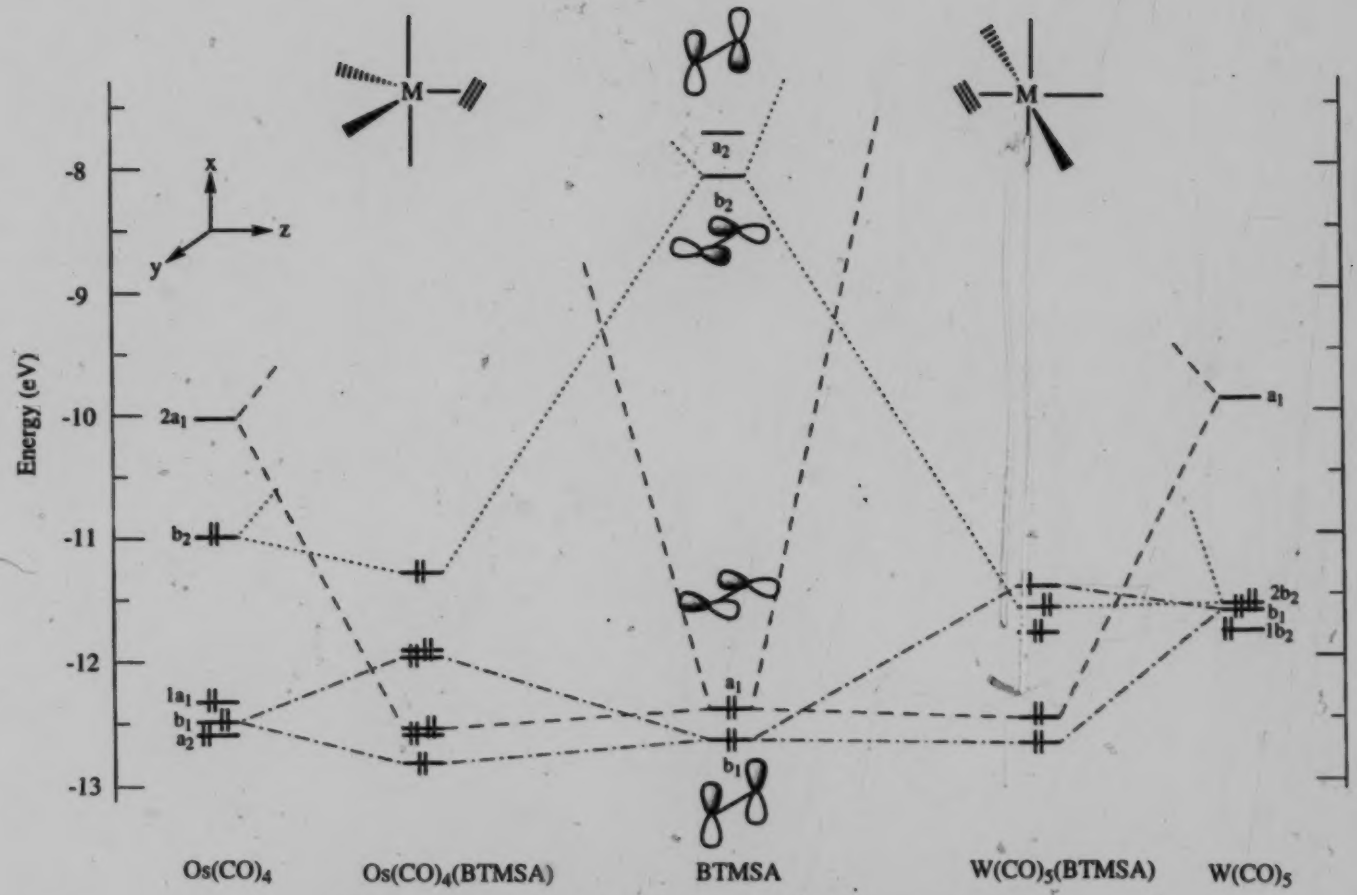

Figure 3-9. Molecular Orbital Interaction Diagram for BTMSA

$$W(CO)_6 + \text{alkyne} \longrightarrow W(CO)_5(\text{alkyne}) + CO \qquad (3\text{-}2)$$

Table 3-11. Energetics Calculated for the Reaction Shown in Eq. (3-2)

Alkyne	ΔE (rxn) basis D1 (kcal/mol)	ΔE (rxn) basis T2 (kcal/mol)
Butyne	11.58	41.30
HFB	1.73	---
BSA	12.17	---
BTMSA	13.49	16.35

$$Os(CO)_4(\text{alkyne}) \longrightarrow Os(CO)_3(\text{alkyne}) + CO \qquad (3\text{-}3)$$

Table 3-12. Energetics Calculated for the Reaction Shown in Eq. (3-3)

Alkyne	ΔE (CO dissociation) basis D1 (kcal/mol)	ΔE (CO dissociation) basis T2 (kcal/mol)
Butyne	14.02	14.46
HFB	21.69	---
BSA	21.81	---
BTMSA	22.22	22.53

$$W(CO)_5(\text{alkyne}) \longrightarrow W(CO)_4(\text{alkyne}) + CO \qquad (3\text{-}4)$$

Table 3-13. Energetics Calculated for the Reaction Shown in Eq. (3-4)

Alkyne	ΔE (CO dissociation) basis D1 (kcal/mol)	ΔE (CO dissociation) basis T2 (kcal/mol)
Butyne	16.96	17.81
HFB	15.71	---
BSA	21.24	---
BTMSA	21.98	21.62

In the reactions that produce the metal-alkyne species (eqs. (3-1) and (3-2)), HFB again stands out having a much smaller ΔE. Only the $Os(CO)_4$(HFB) reaction is exothermic, with the tungsten reactions being more endothermic than the osmium ones. It is interesting to note that the better basis T2 gives more positive ΔE values with a very large increase (~30 kcal/mol) for butyne.

In equations (3-3) and (3-4), CO dissociation from the metal-alkyne compounds is endothermic in all cases, which is expected since a formally

unsaturated intermediate is being formed. For osmium, the ΔE for butyne is ~ 2/3 of that for the other alkynes, while both butyne and HFB show similar results in the tungsten complexes.

Previous calculations on the iron triad acetylene systems show that the CO dissociated intermediate is very close in energy to the CO dissociated transition state[12]; it is assumed that this holds for the alkynes in this study as well. From the calculated CO dissociation energies, the butyne compound will lose CO a lot easier than the remaining metal-alkyne complexes. A kinetic study on the CO dissociation from $Os(CO)_4(HFB)$[23] gives $\Delta H^* = 23.5$ kcal/mol which shows good agreement with the ΔE calculated above, which is equal to 21.69 kcal/mol. Unlike the alkyne reaction, basis T2 does not change the dissociation energies dramatically for butyne or BTMSA in either the tungsten or osmium systems.

3.4 Conclusions

It is reassuring that DFT can reproduce the differences observed experimentally between the π-acidic and π-donor alkynes even when the fluorine and hydrogen atoms are not described that well. These differences between alkyne ligands are also observed in the extended Hückel fragment orbital analysis.

Changing the basis set has a larger effect on the calculated geometry of the free alkynes with smaller changes being seen in the metal-alkyne species. However, the calculated ΔE is more basis set dependent for the reactions producing the $M(CO)_x$(alkyne) species (eqs. (3-1) and (3-2)) than for dissociation of CO from the 18 electron species (eqs. (3-3) and (3-4)).

From the computed structures it appears that all of the metal-alkyne complexes have an increased metal-alkyne interaction upon CO dissociation. This is borne out by the molecular orbital pictures, which show the classical 4e⁻

interaction between the alkyne and the d^6 C_{2v} symmetric $W(CO)_4$ fragment. The molecular orbital pictures are less clear in the $Os(CO)_3$(BTMSA) complex due to orbital mixing. Nevertheless, the alkyne is a $4e^-$ donor, which has also been shown to be true for the Fe, Ru, and Os acetylene systems[12].

3.5 References

1. Gaussian 94, Revision D.3, Frisch, M. J.; Trucks, J. W.; Schlegel, H. B.; Gill, P. M. W.; Johnson, B. G.; Robb, M. A.; Cheeseman, J. R.; Keith, T.; Petersson, G. A.; Montgomery, J. A.; Raghavachari, K.; Al-Laham, M. A.; Zakrzewski, V. G.; Ortiz, J. V.; Foresman, J. B.; Cioslowski, J.; Stefanov, B. B.; Nanayakkara, A., Challacombe, M.; Peng, C. Y.; Ayala, P. Y.; Chen, W.; Wong, M. W.; Andres, J. L.; Replogle, E. S.; Gomperts, R.; Martin, R. L.; Fox, D. J.; Binkley, J. S.; Defrees, D. J.; Baker, J.; Stewart, J. P.; Head-Gordon, M.; Gonzalez, C.; and Pople, J. A. Gaussian, Inc., Pittsburgh PA, 1995.

2. Becke, A. D. *J. Chem. Phys.* **1993**, *98*, 5648.

3. Lee, C.; Yang, W.; Parr, R. G. *Phys. Rev. B* **1988**, *37*, 785.

4. (a) Stevens, W. J.; Basch, H.; Krauss, M. *J. Chem. Phys.* **1984**, *81*, 6026. (b) Stevens, W. J.; Krauss, M.; Basch, H.; Jasien, P. G. *Can. J. Chem.* **1992**, *70*, 612.

5. Huzinaga, S. *J. Chem. Phys.* **1965**, *42*, 1293.

6. Andzelm, J.; Klobukowski, M.; Radzio-Andzelm, E.; Sakai, Y.; Huzinaga, S. (Ed.); Tatewaki, H. *Gaussian Basis Sets for Molecular Calculations*; Elsevier: Amsterdam, 1984.

7. Tanimoto, M.; Kuchitsu, K.; Morino, Y. *Bull. Chem. Soc. Japan* **1969**, *42*, 2519.

8. Chang, C. H.; Andreassen, A. L.; Bauer, S. H. *J. Org. Chem.* **1971**, *36*, 920.

9. Cradock, S.; Nicoll, K. A. S.; Rankin, W. H. *J. Mol. Struct.* **1990**, *216*, 213.

10. Trætteberg, M.; Bakken, P.; Liebman, J. F.; Hulce, M. *J. Mol. Struct.* **1995**, *346*, 101.

11. Bruckmann, J.; Krüger, C. *Acta Cryst.* **1997**, *C53*, 1845.

12. Decker, S. A.; Klobukowski, M. *J. Am. Chem. Soc.* in press.

13. (a) Sosa, C.; Andzelm, J.; Elkin, B. C.; Wimmer, E.; Dobbs, K. D.; Dixon, D. *J. Phys. Chem.* **1992**, *96*, 6630. (b) Delley, B.; Wrinn, M.; Lüthi, H. P. *J. Chem. Phys.* **1994**, *100*, 5785. (c) Li, J.; Schreckenbach, G.; Ziegler, T. *J. Am. Chem. Soc.* **1995**, *117*, 486.

14. Huang, J.; Hedberg, K.; Pomeroy, R. K. *Organometal.* **1988**, *7*, 2049.

15. Arnesen, S. P.; Seip, H. M. *Acta. Chem. Scand.* **1966**, *20*, 2711.

16. Schaftenaar, G. *QCPE Bulletin* **1992**, *12*, 3 (available from http://www.caos.kun.nl/~schaft/molden).

17. Ball, R. G.; Burke, M. R.; Takats, J. *Organometal.* **1987**, *6*, 1918.

18. Jacké, J. Ph.D. Thesis, Universität-Gesamthochschule-Duisburg, 1989.

19. Sakai, Y.; Tatewaki, H.; Huzinaga, S. *J. Comput. Chem.* **1982**, *3*, 6.

20. Wink, D. J.; Creagan, B. T. *J. Am. Chem. Soc.* **1990**, *112*, 8585.

21. Chapter Five

22. YAeHMOP (Yet Another extended Hückel Molecular Orbital Program), Version 1.2, Greg Landrum, February 26, 1996.

23. Pearson, J.; Cooke, J.; Takats, J.; Jordan, R. B. *J. Am. Chem. Soc.* **1998**, *120*, 1434.

3.6 Appendix: Calculated Structural Parameters

Table 3-A1. Calculated Geometry of $Os(CO)_4$(alkyne) (D1 basis set)

	Butyne	HFB	BSA	BTMSA
Bond Length (Å)				
M-CO_{ax}	1.977	1.995	1.980	1.975
M-CO_{eq}	1.960	1.973	1.956	1.949
CO_{ax}	1.160	1.153	1.159	1.161
CO_{eq}	1.167	1.160	1.166	1.168
M-C	2.230	2.162	2.257	2.288
C≡C	1.302	1.315	1.308	1.301
C-X	1.503	1.483	1.863	1.880
X-R	1.11	1.41/1.40	1.53/1.54	1.90
Angle (°)				
C_{ax}-M-C_{ax}	169.6	173.9	171.5	171.2
C_{eq}-M-C_{eq}	104.7	100.4	104.7	106.9
C-M-C	33.9	35.4	33.7	33.0
C-C-X	148.5	143.4	151.7	153.6
C-X-R	111.3/111.6	114.2/111.5	111.2/109.2	108.1/108.4

Table 3-A2. Calculated Geometry of $Os(CO)_3$(alkyne) (D1 basis set)

	Butyne	HFB	BSA	BTMSA
Bond Length (Å)				
M-CO_{ax}	1.899	1.890	1.893	1.893
M-CO_{eq}	1.958	1.965	1.954	1.949
CO_{ax}	1.170	1.165	1.170	1.171
CO_{eq}	1.167	1.160	1.166	1.168
M-C	2.022	2.029	2.056	2.066
C≡C	1.365	1.356	1.360	1.354
C-X	1.507	1.495	1.881	1.894
X-R	1.11	1.40	1.53/1.54	1.90
Angle (°)				
C_{ax}-M-C_{eq}	91.8	90.3	90.6	90.6
C_{eq}-M-C_{eq}	101.9	99.4	103.4	105.1
C-M-C	39.5	39.0	38.6	38.2
C-C-X	139.1	139.3	143.6	147.5
C-X-R	113.0/109.4/112.4	114.2/110.1/111.6	112.0/108.0/109.0	111.0/106.7/107.2

Table 3-A3. Calculated Geometry of $W(CO)_5$(alkyne) (D1 basis set)

	Butyne	HFB	BSA	BTMSA
Bond Length (Å)				
$M\text{-}CO_{ax}$	2.069	2.083	2.072	2.070
$M\text{-}CO_{eq1}$	2.066	2.096	2.071	2.065
$M\text{-}CO_{eq2}$	2.023	2.064	2.021	2.014
CO_{ax}	1.166	1.160	1.164	1.165
CO_{eq1}	1.165	1.156	1.164	1.164
CO_{eq2}	1.170	1.163	1.170	1.171
M-C	2.435	2.251	2.429	2.460
C≡C	1.270	1.296	1.282	1.280
C-X	1.497	1.482	1.867	1.891
X-R	1.11	1.40/1.41	1.53	1.90/1.89
Angle (°)				
C_{ax}-M-Cax	176.1	176.2	175.7	174.7
C_{eq}-M-C_{eq}	172.1	164.6	168.1	165.7
C-M-C	30.2	33.5	30.6	30.2
C-C-X	156.5	144.6	155.1	152.2
C-X-R	110.3/111.9	110.3/111.9	108.6/109.4	106.2/109.0

Table 3-A4. Calculated Geometry of $W(CO)_4$(alkyne) (D1 basis set)

	Butyne	HFB	BSA	BTMSA
Bond Length (Å)				
$M\text{-}CO_{ax}$	2.018	2.022	2.008	2.003
$M\text{-}CO_{eq}$	2.069	2.089	2.070	2.062
CO_{ax}	1.171	1.166	1.171	1.173
CO_{eq}	1.164	1.157	1.164	1.166
M-C	2.119	2.091	2.163	2.192
C≡C	1.330	1.337	1.328	1.321
C-X	1.509	1.494	1.879	1.900
X-R	1.11	1.40	1.53	1.90
Angle (°)				
C_{ax}-M-C_{eq}	101.5	103.8	98.9	98.4
C_{eq}-M-C_{eq}	163.8	153.4	161.9	159.4
C-M-C	36.6	37.3	35.7	35.1
C-C-X	142.1	140.4	145.0	147.3
C-X-R	112.5/111.1	114.7/110.9/110.7	110.5/108.8	109.7/107.8

Chapter Four

Mechanistic Insight into the Condensation Reactions of $Ru(CO)_4$(HFB) with Saturated 18 - electron Species

4.1 Introduction

$M(CO)_4$(alkyne) complexes undergo ready substitution by phosphine ligands. Kinetic studies carried out on the phosphine substitution of $M(CO)_4$(HFB) (M = Fe, Ru, Os) complexes show that CO dissociation is the rate limiting step and that the dissociation is greatly enhanced by the alkyne ligand[1].

In addition to phosphines, the complexes will also react with $18e^-$ metal complexes (e.g. $M(CO)_5$, M = Ru, Os) to form stable bimetallic compounds with the alkyne bridging the transition metals in some fashion[2]. The resulting ring structure in the bimetallic complex depends both on the metal and the alkyne ligand. Examples of the observed variety are shown in equations (4-1) to (4-4).

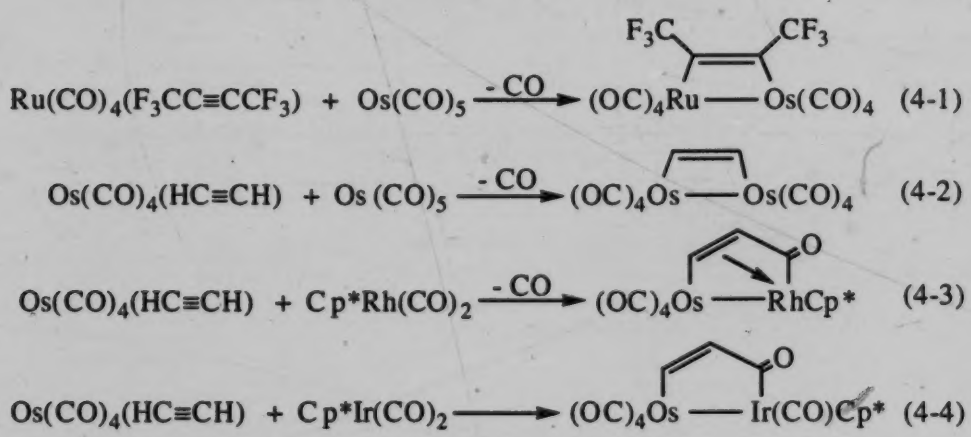
Ru(CO)4(F3CC≡CCF3) + Os(CO)5 - CO (OC)4Ru Os(CO)4 (4-1)
Os(CO)4(HC≡CH) + Os(CO)5 - CO (OC)4Os Os(CO)4 (4-2)
Os(CO)4(HC≡CH) + Cp*Rh(CO)2 - CO (OC)4Os RhCp* (4-3)
Os(CO)4(HC≡CH) + Cp*Ir(CO)2 (OC)4Os Ir(CO)Cp* (4-4)

In the specific case of $Ru(CO)_4$(HFB), the condensation reactions with $Ru(CO)_5$, $Os(CO)_5$ and $Cp^*M(CO)_2$ (M = Rh, Ir) complexes were shown to give only bimetallacyclobutenes (eq. 4-5).

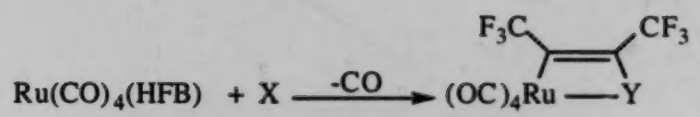

X = $Os(CO)_5$, $Cp^*Rh(CO)_2$, $Cp^*Ir(CO)_2$
Y = $Os(CO)_4$, $Cp^*Rh(CO)$, $Cp^*Ir(CO)$ (4-5)

The products of these reactions have been previously characterized by IR[3], NMR[3], and X-ray crystallographic studies[4,5]. While the reaction with $Ru(CO)_5$ does produce the analogous bimetallacycle, the $Ru(CO)_5$ decomposition product, $Ru_3(CO)_{12}$, is also formed (Scheme 4-1) as indicated by its IR spectrum[6]. Due to this complication, the present study focused solely on the kinetics of the condensation reaction of $Ru(CO)_4$(HFB) with $Os(CO)_5$ and $Cp^*M(CO)_2$ (M = Rh, Ir) to learn more about the reaction mechanism.

Scheme 4-1. Decomposition of $Ru(CO)_5$

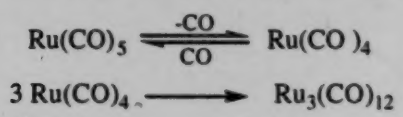

4.2 Results

4.2.1 Kinetic Model

The kinetics of the reaction were monitored by IR spectroscopy, with the CO stretching bands used for $Ru(CO)_4$(HFB) and the bimetallacyclic products listed in Table 4-1. A representative example of the $Ru(CO)_4$(HFB)/$Os(CO)_5$ reaction as monitored by IR is shown in Figure 4-1. Both the appearance of product peaks and disappearance of the reactant were analyzed to serve as a check on the model; Figure 4-2 shows absorbance-time curves for the Ru/Os reaction at different concentrations of $Os(CO)_5$.

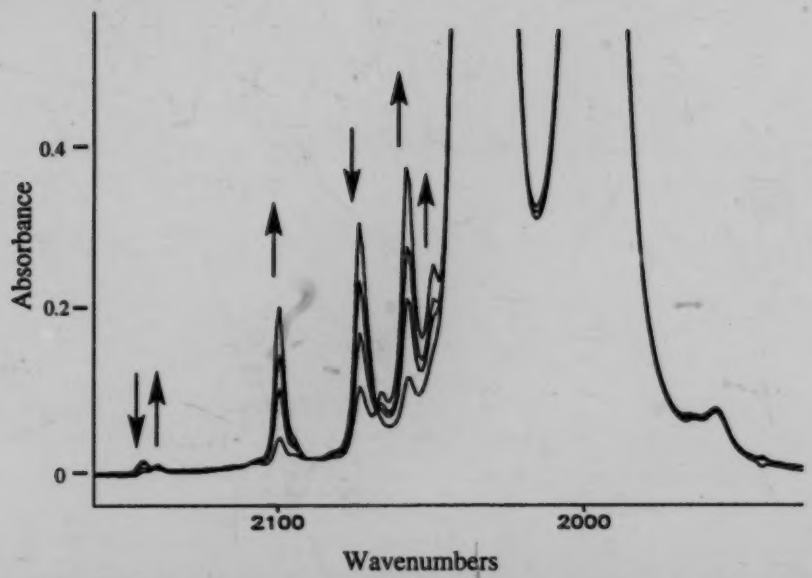

Figure 4-1. Representative IR Spectra for the Reaction of $Ru(CO)_4(HFB)$ ($6.89x10^{-4}$ M) with $Os(CO)_5$ ($9.41x10^{-3}$ M) in Pentane at 22.6 °C. The up arrows indicate product appearance while $Ru(CO)_4(HFB)$ disappearance is shown with the down arrows. The wide bands close to 2000 cm^{-1} are $Os(CO)_5$.

Table 4-1. CO Bands Monitored in the Kinetic Study of the $Ru(CO)_4(HFB)$ Condensation Reactions

Species	CO Bands (cm^{-1})	
$Ru(CO)_4(HFB)$	2073	2042
$RuOs(CO)_8(HFB)$	2099	2058
$Cp^*IrRu(CO)_5(HFB)$	2110	2051
$Cp^*RhRu(CO)_5(HFB)$	2109	2050

As can be seen from Figure 4-2, the reactions do not give simple first order curves; there appears to be a fast initial stage to the reaction, especially at lower temperatures. It is also apparent from Figure 4-2 that the overall rate seems to increase with increasing concentration of $Os(CO)_5$. This concentration

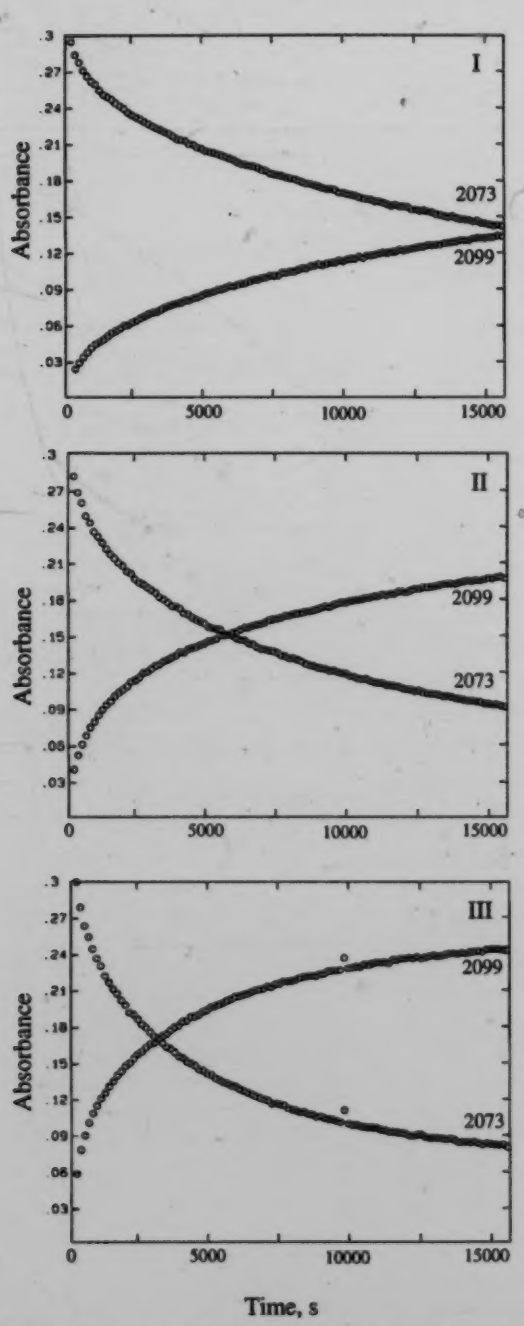

Figure 4-2. Absorbance Time Curves for the Reaction of $Ru(CO)_4(HFB)$ with $Os(CO)_5$ at Different Concentrations of $Os(CO)_5$; I: 2.19 x 10^{-3} M, II: 9.41 x 10^{-3} M, III: 17.4 x 10^{-3} M.

dependence indicates that a simple rate limiting CO dissociation had to be abandoned and the more complex mechanism, Scheme 4-2, was devised. This mechanism takes into account the experimental observation that, for the reaction with $Os(CO)_5$, intermetallic CO exchange was observed prior to product formation in ^{13}CO labeling studies[3]. The observations for $Cp^*Ir(CO)_2$ are quite similar to those with $Os(CO)_5$. However, the reaction with $Cp^*Rh(CO)_2$ is much closer to simple first-order behaviour. The general order of reactivity is Rh >> Ir > Os.

Scheme 4-2. Proposed Mechanism for the Condensation Reactions

$$Ru(CO)_4(HFB) \underset{k_{-1}}{\overset{k_1}{\rightleftharpoons}} \{Ru(CO)_3(HFB)\} + CO$$

$$\{Ru(CO)_3(HFB)\} + X \underset{k_{-2}}{\overset{k_2}{\rightleftharpoons}} \{Ru(CO)_3(HFB)(\mu\text{-}CO)Y\}$$

$$\{Ru(CO)_3(HFB)(\mu\text{-}CO)Y\} \xrightarrow{k_3} \text{bimetallacyclobutene}$$

$X = Os(CO)_5, Cp^*Rh(CO)_2, Cp^*Ir(CO)_2$

$Y = Os(CO)_4, Cp^*Rh(CO), Cp^*Ir(CO)$

4.2.2 Rate Law

Assuming steady states for both intermediates (species in curly brackets in Scheme 4-2), the following rate law can be derived:

$$\begin{aligned} Rate &= \frac{k_1 k_2 k_3 [Ru(CO)_4(HFB)][X]}{(k_{-2}+k_3)k_{-1}[CO]+k_2 k_3[X]} \\ &= \frac{k_1 \frac{k_2 k_3}{k_{-1}(k_{-2}+k_3)}[Ru(CO)_4(HFB)][X]}{[CO]+\frac{k_2 k_3}{k_{-1}(k_{-2}+k_3)}[X]} \\ &= \frac{k_1 Ratio\,[Ru(CO)_4(HFB)][X]}{[CO]+Ratio\,[X]} \end{aligned} \qquad (4\text{-}6)$$

where $Ratio = \dfrac{k_2 k_3}{k_{-1}(k_{-2}+k_3)}$ and $X = Os(CO)_5$, $Cp^*Rh(CO)_2$, and $Cp^*Ir(CO)_2$.

The general form (eq. (4-16)) is rearranged and the integral is taken.

$$\int \frac{c+dx}{ax+bx^2}\,dx = -\int dt \tag{4-17}$$

$$\int \left(\frac{c}{x(a+bx)} + \frac{d}{a+bx} \right) dx = -\int dt \tag{4-18}$$

From standard tables, the integral is evaluated as:

$$-\frac{c}{a}\ln\left(\frac{a+bx}{x}\right) + \frac{d}{b}\ln(a+bx) = -t + C \tag{4-19}$$

$$\left(\frac{d}{b} - \frac{c}{a}\right)\ln(a+bx) + \frac{c}{a}\ln x = -t + C \tag{4-20}$$

At t = 0, x = x_o = Ru_o, which, when substituted into the above equation, can be used to solve for the integration constant C (equation (4-21)):

$$C = \left(\frac{d}{b} - \frac{c}{a}\right)\ln(a+bx_o) + \frac{c}{a}\ln x_o \tag{4-21}$$

Substitution back into equation (4-20) with rearrangement gives the integrated form of the rate law.

$$\left(\frac{d}{b} - \frac{c}{a}\right)\{\ln(a+bx) - \ln(a+bx_o)\} + \frac{c}{a}\{\ln x - \ln x_o\} + t = 0 \tag{4-22}$$

Normal, unweighted least squares fitting was used for the analysis in which larger absorbances (and therefore larger concentrations) have a proportionately greater weight in the fitting process. This minimizes the influence on the fits of small absorbances that have larger percentage errors due to baseline variations.

4.2.3 Treatment of the Data

To perform a fit of the experimental data to this model the initial $Ru(CO)_4$(HFB), X, and CO concentrations were required. The CO dissociation rate, k_1, obtained from phosphine substitution kinetics was used in the fitting and *Ratio* was determined from the best fit of the data to the rate law.

Using a Newton-Raphson iteration algorithm, the integrated rate law was solved for x at the experimental t values which correspond to when the IR spectra were recorded. The initial reactant concentrations were fixed along with the CO dissociation rate (k_1) and the dead time (t_o), which is the difference between the true time zero and the time the first point was measured. Only *Ratio* with the reactant and product extinction coefficients (eqs. (4-23a) and (4-23b)) were evaluated using one reactant and one product IR band. The expressions for the extinction coefficients are:

$$A_{reactant} = \varepsilon_{Ru}[Ru] \times b + blank \qquad (4\text{-}23a)$$

$$A_{product} = \varepsilon_{RuM}[Ru_o - Ru] \times b + blank \qquad (4\text{-}23b)$$

where b is the path length (0.0475 cm) and *blank* is the baseline absorbance.

Attempts to fit the experimental data met with difficulties. In assessing potential reasons for the difficulties it was noticed that the phosphine substitution kinetics, whose k_1 values were used in the fitting procedure, and the condensation reactions were run in different solvents, CH_2Cl_2 and pentane, respectively. It was assumed that k_1 varied little with the nature of the solvent, based on the kinetic studies on the $Os(CO)_4(HFB)$ system[1]. However, in view of the difficulties, it was decided to determine the value of k_1 in pentane.

4.2.3.1 CO Dissociation From $Ru(CO)_4(HFB)$ in Pentane

Using PPh_3, phosphine substitution in $Ru(CO)_4(HFB)$ was followed by IR. The reaction proceeds to the doubly substituted $Ru(CO)_2(PPh_3)_2(HFB)$ via sequential CO substitution (Scheme 4-3).

Scheme 4-3. Phosphine Substitution Mechanism for $Ru(CO)_4(HFB)$

$$Ru(CO)_4(HFB) + PPh_3 \xrightarrow{k_1} Ru(CO)_3(HFB)(PPh_3) + CO$$

$$Ru(CO)_3(HFB)(PPh_3) + PPh_3 \xrightarrow{k_2} Ru(CO)_2(HFB)(PPh_3)_2 + CO$$

The rate of the second substitution (k_2) was too large to be determined in the kinetic analysis. The disappearance of the $Ru(CO)_4$(HFB) peaks at 2073 and 2042 cm^{-1} was monitored and a least-squares fit of the data to a monophasic model (one rate constant) was used to determine k_1. If k_2 had been small enough to be determined, the data would fit a biphasic model that has two rate constants. The data fits were analogous to those for the reaction in CH_2Cl_2, making k_1 independent of the concentration of PPh_3. The rate law for CO dissociation is given by:

$$Rate = k_1[Ru(CO)_4(HFB)] \qquad (4\text{-}24)$$

Table 4-2 lists the CO dissociation rate constants, k_1, obtained from the reactant's (2073 cm^{-1}) and product's (2042 cm^{-1}) IR absorbances for the various temperatures monitored. The activation parameters ΔH^* and ΔS^* were calculated from the k_1 values using the Eyring equation[7]:

$$k_1 = \frac{k_B T}{h} e^{-\Delta H^*/RT} e^{-\Delta S^*/R} \qquad (4\text{-}25)$$

Because of the faster rate in pentane, PPh_3 substitution could only be monitored up to 11 °C, but having the activation parameters allowed for extrapolation to the higher temperatures that were used in the condensation reaction of $Ru(CO)_4$(HFB) with $Os(CO)_5$ (Section 4.2.3.4). As expected, the positive value for ΔS^* (52.3 J/mol·K) is consistent with a dissociative mechanism.

Comparing k_1 in pentane to those in CH_2Cl_2 (Table 4-3), there is an approximate 2.5 - fold rate increase as the solvent is changed. Obviously the assumption of the absence of a solvent effect on the CO dissociation rate constant in $Ru(CO)_4$(HFB) was not valid. Interestingly, there is a large solvent effect for ruthenium, a situation that was not observed for osmium[1].

With the proper CO dissociation rates available, the data on formation of bimetallacyclic compounds could be reanalyzed.

4.2.3.2 Initial Concentrations of Reactants

The concentration of $Ru(CO)_4(HFB)$ was determined from the absorbance values in the first IR spectrum recorded in each run, using the absorbance-concentration calibration curve determined for $Ru(CO)_4(HFB)$. To get the concentration at time zero, the $Ru(CO)_4(HFB)$ concentration from the first spectrum was used to calculate an extinction coefficient and the reactant disappearance data was refit to determine the initial $Ru(CO)_4(HFB)$ concentration.

Table 4-2. Kinetic Results for PPh_3 Substitution in $Ru(CO)_4(HFB)$ in Pentane

Temperature[a] (°C)	$[Ru(CO)_4HFB]$ (x 10^4M)	$[PPh_3]$ (x 10^3M)	k_1 (2073) (x 10^3 s^{-1})	k_1 (2042) (x 10^3 s^{-1})	ΔH^* (kJ/mol)	ΔS^* (J/mol·K)
-8.6	7.00	7.0	0.165	0.163		
-8.5	7.53	7.0	0.163	0.166		
2.8	6.55	7.0	1.05	1.06	97.6±1.8	52.3±6.5
4.3	6.31	7.0	1.31	1.31	(103.6±7.1)[b]	(66.0±2.5)[b]
6.6	5.05	7.0	1.89	1.81		
10.8	4.64	7.0	3.72	3.72		

[a] average temperature for the kinetic run

[b] values in CH_2Cl_2

Table 4-3. Rates of CO Dissociation From $Ru(CO)_4(HFB)$ in Pentane and CH_2Cl_2

Temperature (°C)	k_1 (CH_2Cl_2) (x 10^3 s^{-1})	k_1 (pentane) (x 10^3 s^{-1})
-8.5	0.0556	0.163
3.0	0.412	1.08
10.0	1.29	3.17

This was done using the integrated rate law where the parameter Ru_o is evaluated rather than being fixed. Since the majority of the incoming metal carbonyl species' concentrations were also obtained from the first IR spectrum of the kinetic run, the concentration change in $Ru(CO)_4(HFB)$ was used to correct the $18e^-$

transition metal complex concentration as well, assuming a 1:1 stoichiometry. The corrected concentrations were used in all further kinetic analysis.

Relying on one absorbance reading to calculate the corrected concentration can introduce large errors. As well, the magnitude of the concentration correction is directly related to the dead time used in the fitting. However, the associated error can be judged by the constancy of the extinction coefficient in the product kinetic runs.

4.2.3.3 Kinetic Parameters: Values of the Ratio

The experimental data were treated using the corrected initial concentrations of the reactants and the newly obtained CO dissociation rates in pentane; the latter were extrapolated, when needed, to the temperatures of the condensation reactions using the activation parameters ΔH^* and ΔS^* (eq. (4-6)). As indicated before, the results of the fitting procedure are values for the *Ratio* and the extinction coefficients of the reactant and product.

The kinetic results for the reaction with $Os(CO)_5$ are listed in Table 4-4. The value of *Ratio* is in the 2 to $4x10^{-4}$ range, much smaller than unity (the implication of the *Ratio* value will be addressed in the Discussion section). Although it is expected that the value of the *Ratio* will be the same for both reactant and product analysis, this is only true for the first two kinetic runs having large $Os(CO)_5$ concentrations. Furthermore, the value of the reactant *Ratio* for the second run is significantly different from the other values and, therefore, the effect of varying k_1 was investigated. Modifying the value of k_1 for the kinetic run and refitting the kinetic data adjusted the reactant *Ratio* value by a similar amount. For example, a 13% increase in k_1 ($2.20x10^{-2}$ s^{-1}) results in a 13% decrease in Ratio ($3.75x10^{-4}$). The effect of the dead time, t_o, was also explored, as shown in

Table 4-4. Kinetic Results for the Reaction of $Ru(CO)_4(HFB)$ with $Os(CO)_5$[a]

[Ru] x10³ (M)	[Os] x10³ (M)	Temp.[c] (°C)	Dead Time (s)	k_1 x10² (s^{-1})	Reactant (2073 cm^{-1})		Product (2099 cm^{-1})	
					Ratio[b] x10⁴	ε x10⁻³ ($cm^{-1}M^{-1}$)	Ratio[b] x10⁴	ε x10⁻³ ($cm^{-1}M^{-1}$)
.752	17.4	22.8	200	1.97	2.97±0.11	8.66	3.12±0.13	7.22
.697	15.0	22.8	200	1.97	4.22±0.13	8.80	4.14±0.22	7.54
.689	9.41	22.6	200	1.92	2.44±0.13	8.77	4.14±0.14	7.54
.799	2.19	22.8	200	1.97	2.65±0.45	8.77	4.83±0.67	6.06

[a] standard error in the least squares fit is ~1x10⁻³

[b] Ratio error limits are 95% confidence limits (~ 3σ)

[c] average temperature for the kinetic run

Table 4-5. Effect of Dead Time, t_o, on Ratio[a]

t_o (s)	[Ru] x10³M	[Os] x10³M	Reactant		Product	
			Ratio[b] x10⁴	ε x10⁻³ ($cm^{-1}M^{-1}$)	Ratio[b] x10⁴	ε x10⁻³ ($cm^{-1}M^{-1}$)
140	.822	2.21	2.94±0.42	8.77	4.43±0.58	5.99
200	.799	2.19	2.65±0.45	8.77	4.83±0.67	6.06
260	.782	2.17	3.60±0.55	8.77	5.23±0.75	6.11

[a] $k_1 = 1.97x10^{-2}$, temperature = 22.8°C

[b] Ratio error limits are 95% confidence limits (~ 3σ)

Table 4-6. Kinetic Results for the Reaction of $Ru(CO)_4(HFB)$ with $Cp^*Ir(CO)_2$[a]

[Ru] x10³ (M)	[Ir] x10³ (M)	Temp.[c] (°C)	Dead Time (s)	k_1 x10³ (s^{-1})	Reactant (2073 cm^{-1})		Product (2110 cm^{-1})	
					Ratio[b] x10³	ε x10⁻³ ($cm^{-1}M^{-1}$)	Ratio[b] x10³	ε x10⁻³ ($cm^{-1}M^{-1}$)
.748	11.09	4.5	200	1.37	5.08±0.26	8.89	5.53±0.39	3.19
.852	7.65	3.5	200	1.16	4.84±0.22	8.76	5.75±0.50	3.16
.785	4.98	4.3	180	1.32	5.06±0.27	8.93	5.70±0.71	3.03
.904	2.42	4.0	180	1.25	4.53±0.40	8.84	5.72±1.1	3.00

[a] standard error in the least squares fit is ~1x10⁻³

[b] Ratio error limits are 95% confidence limits (~ 3σ)

[c] average temperature for the kinetic run

Table 4-5. Varying the dead time between fits affects the initial reactant concentrations, but has a very small effect on the extinction coefficients. The *Ratio* values are affected more so, but the changes are not at all predictable.

In Table 4-6 the kinetic results are shown for $Cp^*Ir(CO)_2$. The value of the *Ratio* is around $5x10^{-3}$, an order of magnitude larger than that for the $Os(CO)_5$ system, but it is still substantially smaller than one. The agreement between reactant and product, and for the different kinetic runs where the concentration of $Cp^*Ir(CO)_2$ is varied is better than for $Os(CO)_5$. The extinction coefficient for $Ru(CO)_4$(HFB) is very similar to the one found in the osmium system, showing a comparable variation between runs and, thus, indicates that the corrected concentrations are accurate.

For $Cp^*Rh(CO)_2$, the kinetics results are shown in Table 4-7. The value of the *Ratio* is about 1, a lot larger than for the osmium and iridium systems. The reactant and product results agree within error, but some of the associated errors are an order of magnitude larger. The large uncertainty and variation in *Ratio* can be understood in terms of equation (4-6). Since $[X] >> [CO]$, when $Ratio \approx 1$ then $Ratio \cdot [X] >> [CO]$ and the rate is nearly simple first order and independent of *Ratio*. As a result, uncertainties in temperature or concentrations, and systematic errors in the data can have a large effect on *Ratio*. This is illustrated by the small changes in k_1 (via temperature adjustments) that result in dramatic changes in the value of the Ratio (Table 4-8). This was not the case for $Os(CO)_5$ and shows how sensitive the data collection process is for the rhodium system.

Table 4-7. Kinetic Results for the Reaction of $Ru(CO)_4(HFB)$ with $Cp^*Rh(CO)_2$[a]

[Ru] x10^3 (M)	[Rh] x10^3 (M)	Temp.[c] (°C)	Dead Time (s)	k_1 x10^3 (s^{-1})	Reactant (2073 cm^{-1})		Product (2109 cm^{-1})	
					Ratio[b]	ε x10^{-3} ($cm^{-1}M^{-1}$)	Ratio[b]	ε x10^{-3} ($cm^{-1}M^{-1}$)
1.02	7.30	2.7	180	1.03	1.43±0.22	7.44	1.44±2.1	3.09
.925	5.07	2.8	200	1.05	6.42±2.7	8.46	5.49±2.8	3.45
.849	4.97	2.6	200	1.01	3.94±1.5	8.61	5.53±2.8	3.59
.891	2.48	2.6	200	1.01	1.25±0.07	8.71	1.31±0.14	3.60
.844	2.16	2.9	180	1.06	1.24±0.09	8.70	1.41±0.20	3.60

[a] standard error in the least squares fit is ~1x10^{-3}

[b] Ratio error limits are 95% confidence limits (~ 3σ)

[c] average temperature for the kinetic run

Table 4-8. Effect of Temperature on Ratio

[Ru] x10^3M	[Rh] x10^3M	Temp.(°C)	k_1 x10^3 (s^{-1})	Reactant (2073 cm^{-1})		Product (2109 cm^{-1})	
				Ratio[a]	ε x10^{-3} ($cm^{-1}M^{-1}$)	Ratio[a]	ε x10^{-3} ($cm^{-1}M^{-1}$)
.925	5.07	2.8[b]	1.05	6.42±2.7	8.46	5.49±2.8	3.45
		3.3	1.12[d]	1.33±0.10	8.92	1.25[c]	3.64
.849	4.97	2.6[b]	1.01	3.94±1.5	8.61	5.53±2.8	3.59
		3.0	1.07[d]	1.19±0.2	8.80	1.25[c]	3.67

[a] Ratio error limits are 95% confidence limits (~ 3σ); [b] average temperature for the kinetic run

[c] value fixed and product formation refitted to get k_1 which corresponds to the temperature shown

[d] value fixed and reactant disappearance refitted to get new Ratio value

Overall, the $Cp^*Ir(CO)_2$ system appears to be the best behaved showing good agreement between runs and between reactant/product analysis. Errors introduced through the concentration correction have the largest effect with the $Cp^*Rh(CO)_2$ system, which has the largest variation in extinction coefficients between runs.

4.3 Discussion

Although the kinetic analysis does not allow for assignment of the individual rate constants within the *Ratio* term, the magnitude of the *Ratio* does give some insight into the mechanism of the condensation reaction. There are two cases to consider.

(i) When $k_3 >> k_{-2}$, the Ratio term simplifies to:

$$Ratio = \frac{k_2 k_3}{k_{-1} k_3} = \frac{k_2}{k_{-1}} \qquad (4\text{-}26)$$

This suggests that there is a competition between $Ru(CO)_3(HFB)$ reacting with X and recoordination of CO to form $Ru(CO)_4(HFB)$. In this case, the value of *Ratio* is expected to be close to unity, in the range 0.1 - 10, based on the idea that the proposed $16e^-$ intermediate is very reactive and indiscriminate towards available nucleophiles. This is consistent with the observations made on competition ratios for coordinatively unsaturated intermediates, where the nucleophiles are CO and phosphines[8], CO and piperidine[9], or alkenes and phosphines[10].

(ii) When $k_{-2} >> k_3$, the Ratio term can be written as:

$$Ratio = \frac{k_2 k_3}{k_{-1} k_{-2}} \qquad (4\text{-}27)$$

In this case, the $[Ru(CO)_3(HFB)(\mu\text{-}CO)Y]$ intermediate does not immediately collapse to the bimetallacycle product but it is in rapid equilibrium with $Ru(CO)_3(HFB)$ and X. Since $k_3/k_{-2} < 1$ and $k_2/k_{-1} \sim 1$, the value of the *Ratio* is less than one, with k_3 being the rate controlling step.

Both $Os(CO)_5$ and $Cp^*Ir(CO)_2$ appear to follow this second limiting condition. A ^{13}CO labeling experiment confirmed that $k_{-2} >> k_3$ for the reaction with $Os(CO)_5$. The reaction of ^{13}CO enriched $Ru(^{13}CO)_4(HFB)$ with unenriched $Os(CO)_5$ was monitored by variable temperature ^{13}C NMR spectroscopy. It was

observed that, prior to product formation, intermetallic ^{13}CO exchange occurred and that $Os(CO)_5$ was enriched in ^{13}CO. Scheme 4-4 accounts for these observations.

Scheme 4-4. Intermetallic Exchange of ^{13}CO in the Reaction of $Ru(^{13}CO)_4(HFB)$ with $Os(CO)_5$

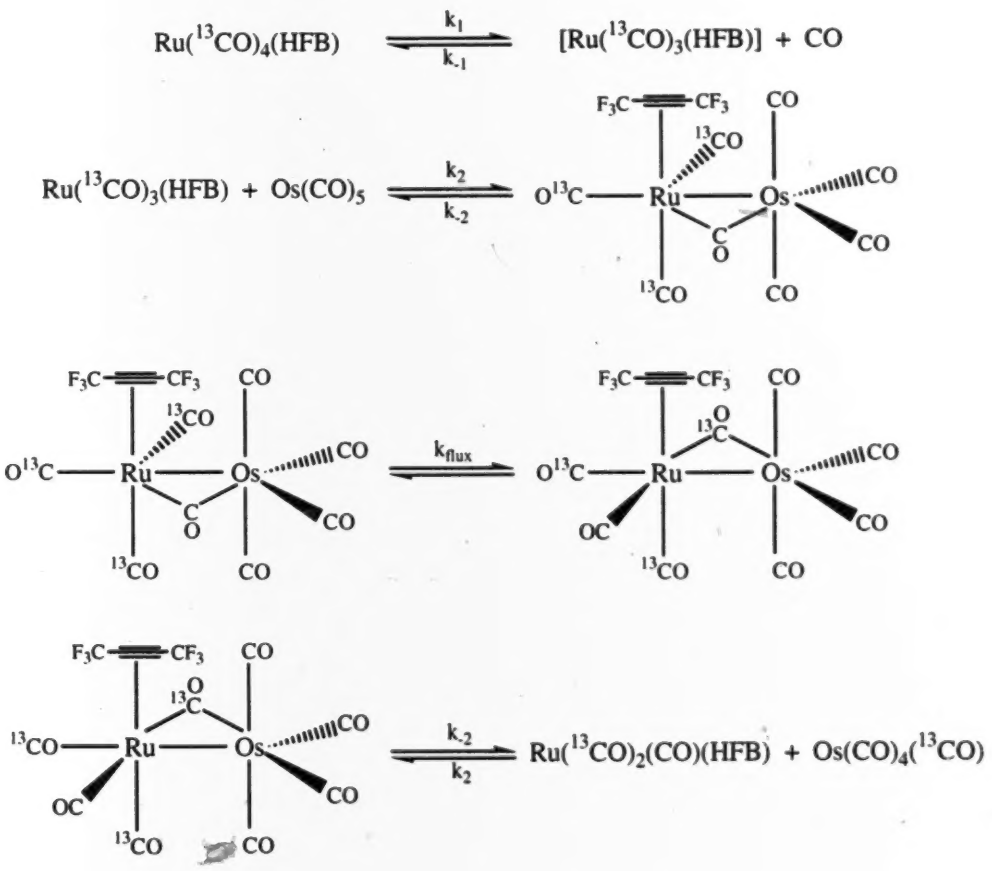

Interestingly, the kinetic results for $Cp^*Rh(CO)_2$ indicate that product formation is much faster than the break up of the intermediate, $k_3 >> k_{-2}$. It is not obvious why this should be the case but perhaps the more favorable formation of

bridging carbonyls with the second-row rhodium impedes the break up of the intermediate and promotes formation of the bimetallacyclic product (eq. (4-28)).

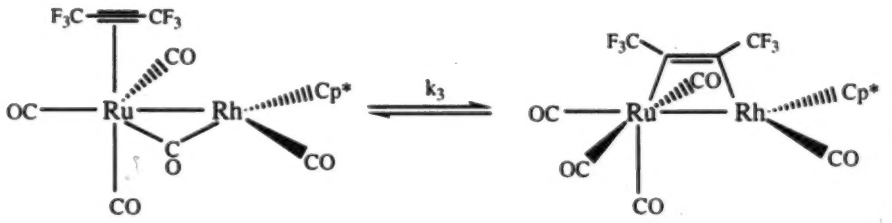

(4-28)

4.5 Conclusions

Qualitatively, the group 9 Cp*-carbonyls react a lot faster with $Ru(CO)_4$(HFB) than does $Os(CO)_5$, in the order Rh >> Ir > Os. Despite this, the limiting conditions for the Ratio term separates out $Cp^*Rh(CO)_2$, leaving $Cp^*Ir(CO)_2$ and $Os(CO)_5$ with apparently comparable reaction mechanisms. This study indicates that ^{13}CO enrichment studies on the condensation reaction with $Cp^*M(CO)_2$ (M = Rh, Ir) would be advantageous to further refine an understanding of the mechanism in these reactions.

4.6 Experimental

4.6.1 Solvents and General Techniques

Pentane was pretreated sequentially with sulfuric acid, aqueous solution of sodium bicarbonate, and distilled water before being dried over magnesium sulfate and distilled from calcium hydride.

Glassware was pretreated with a KOH/ethanol (95%) solution followed by a dilute HCl solution and then rinsed in distilled water and dried at 300°C overnight. All reactions were set up under a nitrogen atmosphere using standard Schlenk techniques. The nitrogen was purified by passing it through a heated (100°C) column of BASF Cu catalyst (R3-11) to remove trace oxygen and a

column of Mallinkrodt Aquasorb (P_2O_5 on an inert support) to remove traces of water.

4.6.2 Kinetic Measurements

Infrared spectra were recorded on a BOMEM MB-100 Fourier transform spectrometer over the range 1600 to 2200 cm^{-1} using a Graseby Specac gas-tight 0.475mm solution cell with CaF_2 windows, amalgamated foil spacer, gaskets, and a stainless steel body. The cell was placed into a double walled cell holder, which was cooled by isopropanol from a Haake Q circulating bath. The temperature of the cell was monitored continuously with a Doric copper-constantan digital thermometer.

The infrared spectrophotometer was used with the program SpectraCalc running on an IBM type 486 computer. It used specially developed programs to control the timing and to display the spectra during the kinetic run. Each spectrum was normalized to the absorbance of the initial spectrum in a spectral region where reactants and products did not absorb. The SpectraCalc data file was converted to ASCII (x,y) format so that parameters could be determined by least-squares analysis. This analysis was done by a program written in BASIC using an iterative least-squares procedure with the Marquardt algorithm.

4.6.3 Starting Materials and Reagents

PPh_3 was obtained from BDH Limited and used without further purification. $Ru(CO)_4(HFB)$[3], $Os(CO)_5$[14], $Cp^*Ir(CO)_2$[15], and $Cp^*Rh(CO)_2$[16] were all prepared using published procedures.

4.6.4 Kinetic Procedure

Stock solutions of all starting materials were prepared in flasks under nitrogen. Prior to the kinetic run, IR's of both reagent stock solutions were taken to determine concentration and volumes to be used in the kinetic run sample.

A 2mL vial with septum was put under a nitrogen atmosphere and then cooled to a temperature below the kinetic monitoring temperature using a dry ice/acetone bath. Reagents were added to the vial sequentially with the same syringe in the order: pentane, $Ru(CO)_4(HFB)$, nucleophile, to give a total volume of 1 ml. The solution was mixed and the IR sample was removed with a cold syringe to prevent reaction. A pentane reference was taken before each kinetic run at the monitoring temperature and the IR cell was at the monitoring temperature when the sample was added. Once the sample was in the cell, collection of the IR spectra began.

4.7 References

1. Pearson, J.; Cooke, J.; Takats, J.; Jordan, R. B. *J. Am. Chem. Soc.* **1998**, *120*, 1434.

2. Takats, J. *J. Cluster Science* **1992**, *3*, 479 and references therein.

3. Gagné, M. R.; Takats, J. *Organometal.* **1988**, *7*, 561.

4. Gagné, M. R.; Takats, J.; Day, V. M. unpublished results.

5. Jacké, J.; Ball, R.; Takats, J. unpublished results.

6. Bruce, M. I.; Jensen, C. M.; Jones, N. L. *Inorg. Synth.* **1989**, *26*, 259.

7. Wiberg, K. B *Physical Organic Chemistry* John Wiley & Sons, New York:1964.

8. (a) Basato, M.; Poë, A. *J. Chem. Soc. Dalton Trans.* **1974**, 456. (b) Huq, R.; Poë, A. J.; Chacola, S. *Inorg. Chim. Acta* **1980**, *38*, 121.

9. (a) Covey, W. D.; Brown, T. L. *Inorg. Chem.* **1973**, *12*, 2820. (b) Hyde, C.; Rarensbourg, D. J. *Inorg. Chem.* **1973**, *12*, 1286.

10. (a) Cardaci, G. *Inorg, Chem.* **1974**, *13*, 368. (b) Chen, L.; Poë, A. J. *Inorg. Chim. Acta* **1995**, *240*, 399. (c) Huber, B. J.; Poë, A. J. *Inorg. Chim. Acta* **1994**, *227*, 215.

11. (a) Riesen, A.; Einstein, F. W. B.; Ma, A. K.; Pomeroy, R. K.; Shipley, J. A. *Organometal.* **1991**, *10*, 3629. (b) Bond, E.; Muetterties, E. L. *Chem. Rev.* **1978**, *78*, 639. (c) Mann, B. E. In *Comprehensive Organometallic Chemistry, Volume 3*; Wilkinson, G.; Stone, F. G. A.; Abel, E. W., Eds.; Pergamon: New York, 1982, p. 89.

12. Washington, J. S. PhD. Thesis, University of Alberta, 1994.

13. Cooke, J. PhD. Thesis, University of Alberta, 1998.

14. Rushman, P.; van Buuren, G. N.; Shirallan, M.; Pomeroy, R. K. *Organometal.* **1983**, *2*, 693.

15. Ball, R. G.; Graham, W. A. G.; Heinekey, D. M.; Hoyano, J. K.; McMaster, A. D.; Mattson, B. M.; Michel, S. T. *Inorg. Chem.* **1990**, *29*, 2023.

16. Kang, J. W.; Maitlis, P. M. *J. Organometal. Chem.* **1971**, *26*, 393.

Chapter Five

Computational Study of the Reaction of $Ru(CO)_4(HFB)$ with $Os(CO)_5$

5.1 Introduction

The elucidation of reaction mechanisms through experiment can be hindered when proposed intermediates cannot be seen, much less characterized. Usually only rationalizations and precedents are given in support of the mechanism when spectroscopic evidence is not available (which is not uncommon). Through the use of calculations, elusive intermediates can be studied with the ability to differentiate between possible structures, giving support to the proposed mechanism.

To provide computational support for the condensation reactions examined in Chapter 4, calculations were performed on the reaction

$$Os(CO)_5 + Ru(CO)_4(HFB) \longrightarrow RuOs(CO)_8(HFB) + CO.$$

It was of particular interest to probe the nature of the intermediate to support the mechanistic model used to fit the collected kinetic data. The effects of basis sets and functionals on this system were also investigated.

5.2 Results and Discussion

5.2.1 Methodology

Density Functional Theory (DFT), the main method used in these calculations, has been shown to work well on transition metal systems[1,2]. Using the Gaussian 94[3] progam, Becke's 3 parameter exchange functional (B3)[4] was combined with the correlation functionals of Lee, Yang, and Parr (LYP)[5] and Perdew and Wang (PW91)[6] to give two functionals: B3LYP and B3PW91. The effective core potential (ECP) of Stevens *et al.*[7] was used to reduce the number of electrons in this system. The core electrons were replaced by the ECP and the

remaining electrons were treated explicitly in the calculations. The double zeta valence (DZV) basis set was modified to build three basis sets:

Basis 1: DZV + d polarization on carbon (ζ_d=0.6) and oxygen (ζ_d=1.154)

Basis 2: DZV + d polarization on carbon and oxygen; SZV on fluorine

Basis 3: SZV on CF_3 groups; DZV + d polarization on the remaining carbons and oxygen

where a quadruple zeta valence (QZV) basis set was used to describe the transition metals in all three basis sets.

With Basis 1, the required calculation time was very long and the remaining basis sets were used to test if a more manageable calculation time could be achieved while keeping the geometry reasonably accurate. As shown in Table 5-1, decreasing the number of basis functions used to describe the system reduces the calculation time.

Table 5-1. Basis Set Breakdown

Basis	No. of Basis Functions	No. of Electrons	Calculation Time[a] (s)	
			B3LYP	B3PW91
1	235	114	217	210
2	211	114	186	---
3	193	114	151	111

[a] time required to complete the Link 502/SCF cycle for the first optimization cycle

Table 5-2 shows the geometry changes in $Ru(CO)_4$(HFB) for the different basis sets and functionals. Even though the C-F distances are very long compared to experiment, this was expected because of the minimal description for F (Basis 2) and the CF_3 groups (Basis 3). The metal-carbonyl and metal-alkyne bonds were more important factors in choosing the basis set and show much better agreement. Basis 3 was chosen since the geometry does not differ much from Basis 1 and the calculation time was much shorter, as shown in Table 5-1. Both

B3LYP and B3PW91 functionals were used for the calculations on the mono-metallic complexes, but only B3LYP was used in the bimetallic system.

Table 5-2. Structural Parameters for $Ru(CO)_4(HFB)$

Parameter	Experiment[a]	Basis 1		Basis 2	Basis 3	
		B3PW91	B3LYP[a]	B3LYP[a]	B3LYP[a]	B3PW91[a]
Bond Length (Å)						
M-C_{ax}	1.967(5)	1.984	0.018	0.021	0.022	0.004
M-C_{eq}	1.966(5)	1.981	0.023	0.024	0.026	0.003
M-C	2.125(4)	2.148	0.014	0.008	-0.027	-0.040
C≡C	1.276(6)	1.308	0.000	0.001	-0.006	-0.006
CO_{ax}	1.130(6)	1.151	0.001	0.000	-0.001	-0.002
CO_{eq}	1.129(6)	1.156	0.001	0.000	-0.001	-0.002
C-CF_3	1.469(6)	1.495	0.002	-0.013	-0.055	-0.058
C-F	1.321(5)	1.371	0.007	0.035	0.133	0.125
C-F[b]	1.331(5)	1.364	0.014	0.039	0.122	0.115
Angle (°)						
C_{ax}-M-C_{ax}	172.7(19)	174.2	-0.1	0.2	0.7	0.9
C_{eq}-M-C_{eq}	98.7(18)	102.1	-0.1	-0.5	-1.3	-1.2
C-M-C	35.0(16)	35.5	-0.2	-0.1	0.3	0.5
M-C-CF_3	145.4(3)	142.9	0.5	0.3	-1.3	-1.2
C_{ax}-M-C	86.5(17)	87.2	0.0	0.1	0.3	0.4
C_{eq}-M-C	113.2(17)	111.2	0.2	0.3	0.5	0.4
Rel. Energy (kcal/mol)		0	0	35.6	214.2	218.6

[a] difference from Basis 1/B3PW91: positive value indicates larger than Basis 1/B3PW91

[b] bond is in the plane of the acetylinic carbons and ruthenium (eclipsed geometry)

While the Hartree-Fock (HF) method does not treat electron correlation and therefore requires less computing time, it usually does not give adequate geometries for transition metal complexes and is not the method of choice for transition metals. However, since the HF calculations on $(\eta^3\text{-}C_7H_7)M(CO)_3$ (M = Fe, Ru, and Os)[9] done in our group showed very good agreement with experiment, the HF approach was tried for $Ru(CO)_4(HFB)$. Table 5-3 compares the HF geometry to DFT and shows that the metal-carbon distances have the largest differences. Even though the overall differences are not that significant, it was decided it would be more appropriate to include electron correlation, especially since the effects due to the breaking of bonds were to be studied.

Table 5-3. Comparison Between DFT and HF on $Ru(CO)_4HFB$

Parameter	Experiment[a]	Basis 3		HF – B3LYP
		B3LYP	HF	
Bond Length (Å)				
M-C_{ax}	1.967(5)	2.006	2.101	0.095
M-C_{eq}	1.966(5)	2.007	2.096	0.089
M-C	2.125(4)	2.120	2.095	-0.025
C≡C	1.276(6)	1.302	1.286	-0.016
CO_{ax}	1.130(6)	1.150	1.118	-0.032
CO_{eq}	1.129(6)	1.155	1.121	-0.034
C-CF_3	1.469(6)	1.439	1.445	0.006
C-F	1.321(5)	1.504	1.455	-0.049
C-F[a]	1.331(5)	1.486	1.441	-0.045
Angle (°)				
C_{ax}-M-C_{ax}	172.7(19)	174.9	173.3	-1.6
C_{eq}-M-C_{eq}	98.7(18)	91.6	92.1	0.5
C-M-C	35.0(16)	35.8	35.8	0.0
M-C-CF_3	145.4(3)	141.7	144.2	2.5
C_{ax}-M-C	86.5(17)	87.6	86.8	-0.8
C_{eq}-M-C	113.2(17)	111.7	112.0	0.3

[a] bond is in the plane of the acetylinic carbons and ruthenium

The hessian for the C_{2v} structure of $Ru(CO)_4(HFB)$ (CF_3's eclipsed) had two imaginary frequencies (a second order saddle point). The vibrational modes, visualized with MOLDEN[10], associated with these frequencies involve the torsion of the CF_3 groups, and are very soft modes. Lowering the symmetry to C_s and C_1 and reoptimizing produced the ground state structure(s) but, as Table 5-4 shows, the energy difference between the different symmetry structures is negligible. Looking specifically at the C≡C, CO, and CF_3 torsion regions, the mode ordering between the different symmetry structures is identical and the wavenumbers for each mode are practically the same. This is true for the remaining modes (not shown) as well. The C_{2v} structure was used in all subsequent calculations in order to exploit computational savings due to higher symmetry.

Table 5-4. Selected Vibrational Modes for $Ru(CO)_4(HFB)$ (cm^{-1})

Mode	Expt.[11]	C_1	C_s	C_{2v}	Assignment[a]
1	---	21.3	20.2	15.7*i*	sym CF_3 torsion
2	---	22.3	21.3	13.9*i*	asym CF_3 torsion
47	1855.7, 1818.0	2027.9	2028.0	2028.1	C≡C alkyne stretch
48	2041.8	2101.8	2101.8	2101.8	asym equatorial CO stretch
49	2071.7	2125.4	2125.4	2125.4	sym eq. CO and ax. CO stretch out of phase
50	2071.7	2134.8	2134.8	2134.8	asym axial CO stretch
51	2143.1	2197.4	2197.4	2197.4	all sym CO stretch
Rel. Energy (kcal/mol)		0.002	0	0.011	

[a] vibrational mode representations shown in Figure 5–1

5.2.2 CO Dissociation From $Ru(CO)_4(HFB)$

The ability of the alkyne ligand to enhance CO lability in group 8 $M(CO)_4(alkyne)$, (M = Fe, Ru, Os) complexes is now firmly established and quantified on the basis of CO substitution kinetics[12,13]. A comparison between $Os(CO)_4(HFB)$ and $Os(CO)_4(C_2H_2)$ shows that the alkyne ligand has only a small, but anticipated, effect on CO lability; $\Delta H^{\ddagger}$ is ~ 2 kcal/mol less for the better π - donor alkyne, acetylene[13]. In the substitution reaction it is assumed that it is the axial CO that dissociates based on the smaller amount of ligand rearrangement necessary to achieve the $M(CO)_3(alkyne)$ intermediate[14] and because of the cis-labilization due to the alkyne[12]. Theoretical studies on related systems with π - donor ligands support cis labilization[15] and calculations done on $M(CO)_4(C_2H_2)$, (M = Fe, Ru, Os)[16], also substantiate this claim with the energy difference between axial and equatorial CO dissociation being 18.6 kcal/mol for Fe. Since, as described above, changing the alkyne ligand does not have a major effect on the lability of CO, it can be assumed that the general shape of the CO dissociation curve calculated for $Ru(CO)_4(HFB)$ will be similar to those in the $M(CO)_4(C_2H_2)$ (M = Fe, Ru, Os) compounds and that the conclusion, preferential axial CO

Figure 5-1. Vibrational Modes of $Ru(CO)_4(HFB)$

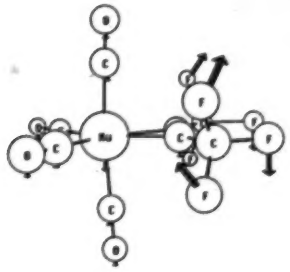

Mode 1

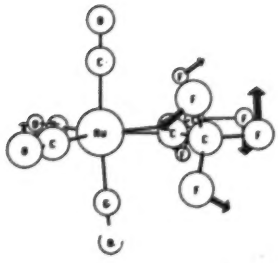

Mode 2

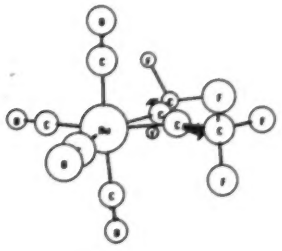

Mode 47

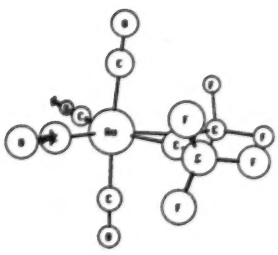

Mode 48

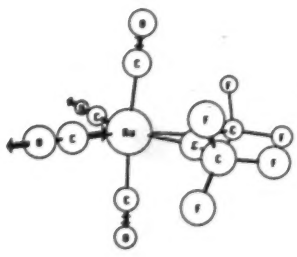

Mode 49

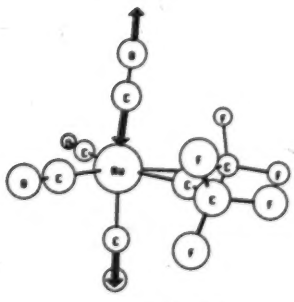

Mode 50

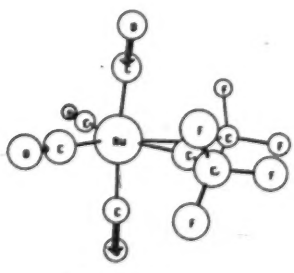

Mode 51

dissociation, will hold as well. It is with this assumption that the energetics for the reaction

$$Ru(CO)_4(HFB) \longrightarrow Ru(CO)_3(HFB) + CO$$

were calculated.

Figure 5-2 shows the optimized structure for both ruthenium complexes, while the structural differences calculated with both functionals, B3LYP and B3PW91, are listed in Table 5-5. The shortening of the metal-alkyne distance upon CO dissociation is accompanied by a lengthening of the alkyne bond, which is expected as the alkyne goes from $2e^-$ to $4e^-$ donation in order to stabilize the otherwise $16e^-$ intermediate. Concurrent with this, the remaining carbonyls move closer to the metal center indicating they are getting more π - back donation as a result of the increased electron density at the metal center. Interestingly, the shortening of the M-CO bond is almost entirely localized on the axial carbonyl ligand, which was also observed for the osmium systems in Chapter 3. This stabilization from the alkyne is thought to be responsible for the increased lability of CO in the group 8 alkyne-carbonyl complexes[12].

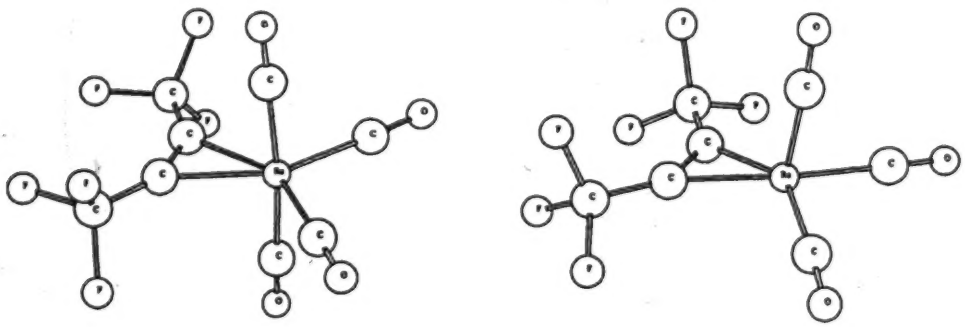

Figure 5-2. Optimized Geometry of $Ru(CO)_4(HFB)$ and $Ru(CO)_3(HFB)$

Table 5-5. Comparison of Structural Parameters for $Ru(CO)_4(HFB)$ and $Ru(CO)_3(HFB)$

Parameter	$Ru(CO)_4(HFB)$			$Ru(CO)_3(HFB)$		$Ru(CO)_3(HFB)$-$Ru(CO)_4(HFB)$	
	Expt.[8]	B3LYP/ Basis 3	B3PW91/ Basis 3	B3LYP/ Basis 3	B3PW91/ Basis 3	B3LYP/ Basis 3	B3PW91/ Basis 3
Bond Length (Å)							
$M-C_{ax}$	1.967(5)	**2.006**	1.988	**1.883**	1.864	**-0.123**	-0.124
$M-C_{eq}$	1.966(5)	**2.007**	1.983	**2.006**	1.984	**-0.001**	0.001
M-C	2.125(4)	**2.120**	2.107	**2.025**	2.015	**-0.095**	-0.092
C≡C	1.276(6)	**1.302**	1.302	**1.331**	1.330	**0.029**	0.028
CO_{ax}	1.130(6)	**1.150**	1.149	**1.160**	1.159	**0.010**	0.010
CO_{eq}	1.129(6)	**1.155**	1.155	**1.155**	1.154	**0.000**	-0.001
$C-CF_3$	1.469(6)	**1.439**	1.437	**1.448**	1.446	**0.009**	0.009
C-F	1.321(5)	**1.504**	1.496	**1.509**	1.502	**0.005**	0.006
C-F[a]	1.331(5)	**1.486**	1.479	**1.490**	1.482	**0.004**	0.003
Angle (°)							
$C_{ax}-M-C_{ax}$	172.7(19)	**174.9**	175.1	---	---	---	---
$C_{eq}-M-C_{eq}$	98.7(18)	**100.8**	100.9	**99.4**	99.6	**-1.4**	-1.3
C-M-C	35.0(16)	**35.8**	36.0	**38.4**	38.5	**2.6**	2.5
$M-C-CF_3$	145.4(3)	**141.7**	141.7	**146.8**	146.7	**5.1**	5.0
$C_{ax}-M-C$	86.5(17)	**87.6**	87.7	**107.0**	106.8	**19.4**	19.1
$C_{eq}-M-C$	113.2(17)	**111.7**	111.6	**108.9**	109.0	**-2.8**	-2.6

[a] bond lies in the plane of the acetylinic carbons and ruthenium

Charge Decomposition Analysis (CDA) for the $Ru(CO)_4(C_2H_2)$/ $Ru(CO)_3(C_2H_2)$ system showed that the alkyne was donating extra electron density upon CO dissociation[16]. Molecular orbital pictures, as visualized using MOLDEN[10], for the important Ru-HFB interactions in the $Ru(CO)_4(HFB)$/ $Ru(CO)_3(HFB)$ system are shown in Figures 5-3 and 5-4. The shape of the molecular orbitals is analogous to those described in Chapter 3. As expected, the orbital interactions in $Ru(CO)_4(HFB)$ are consistent with the Dewar-Chatt-Duncanson bonding model. Interestingly, the molecular orbital pictures for $Ru(CO)_3(HFB)$ show the same orbital mixing observed with the $Os(CO)_3(alkyne)$ systems in Chapter 3. This similarity in orbital interactions

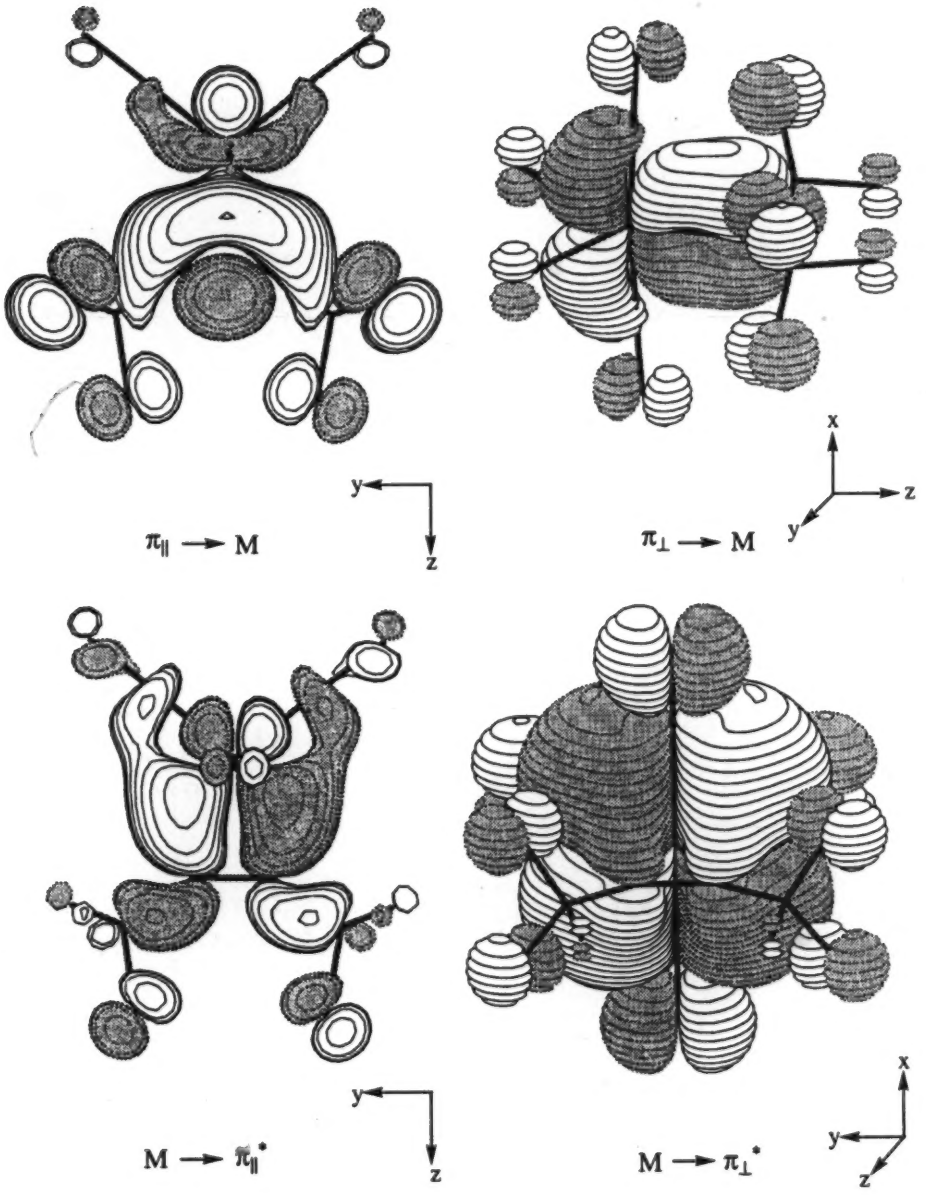

Figure 5-3. Molecular Orbitals for $Ru(CO)_4(HFB)$

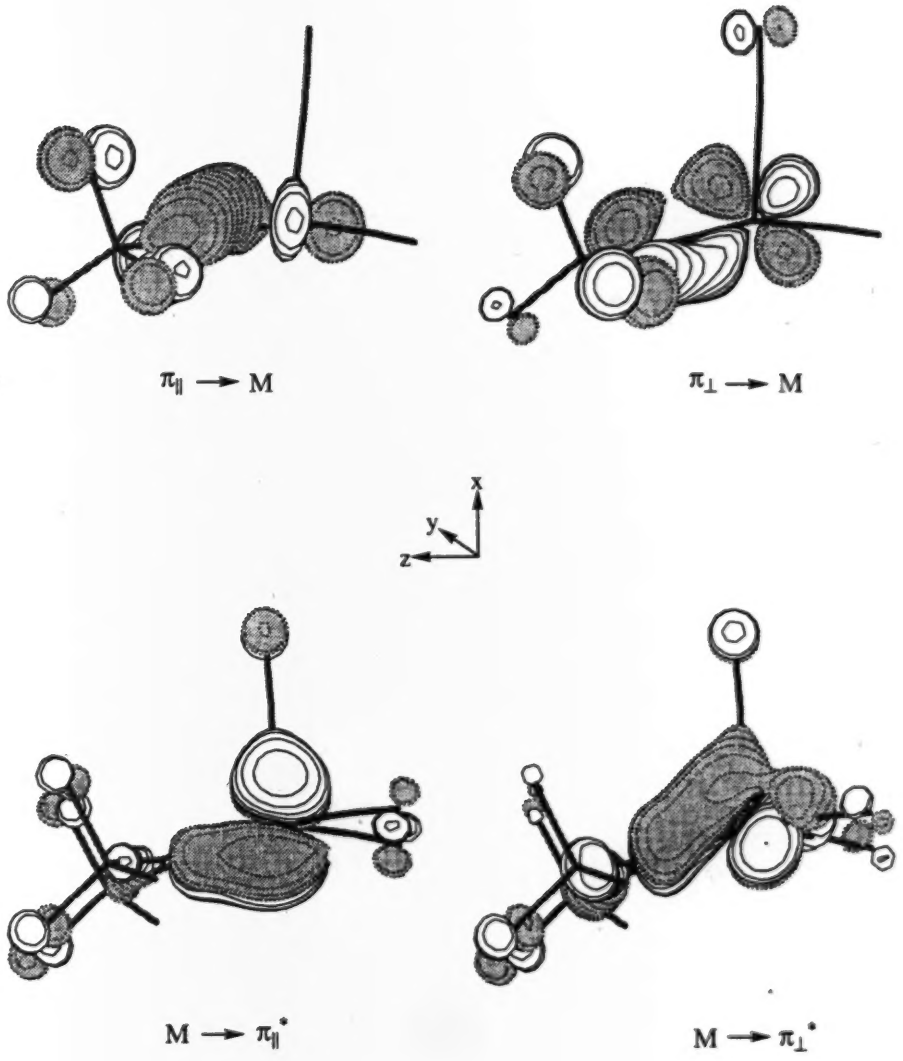

Figure 5-4. Molecular Orbitals for $Ru(CO)_3(HFB)$

shows that HFB also utilizes 4e⁻ donation to stabilize the CO dissociated intermediate.

The calculated energy for CO dissociation from $Ru(CO)_4(HFB)$ is similar to the experimentally determined value (Table 5-6), although the two quantities do not measure the same process. The calculated ΔE is the change in energy going from reactant to the intermediate, while the experimentally determined ΔE is from the reactant to the transition state, ΔH* (Figure 5-5). The comparison of the two quantities is, however, still valid, since the reaction path for CO dissociation in $Ru(CO)_4(C_2H_2)$ has been shown to be very endothermic, with the transition state being close to the energy of the $Ru(CO)_3(C_2H_2)$ intermediate (as depicted in Figure 5-5). A similar situation is expected for the HFB system. In principle, the transition state could be located on the potential energy surface in order to calculate the same ΔE as found from experiment. However, on the basis of the previous work with the acetylene ligand[14], this would only increase the calculated value by about 2 kcal/mol.

Table 5-6. CO Dissociation Energies from $Ru(CO)_4(HFB)$ (kcal/mol)

	B3LYP ΔE	B3PW91 ΔE	Experiment[12] ΔH*
	23.9	26.5	25.0±0.6
ZPE corrected[a]	25.7	28.4	

[a] ZPE = Zero-Point Energy

5.2.3 Reaction of $Ru(CO)_4(HFB)$ with $Os(CO)_5$

The condensation reaction of $Ru(CO)_4(HFB)$ with $Os(CO)_5$ is thought to proceed by attack of $Os(CO)_5$ on the CO dissociated intermediate $Ru(CO)_3(HFB)$ followed by CO migration to give the intermediate bimetallic compound

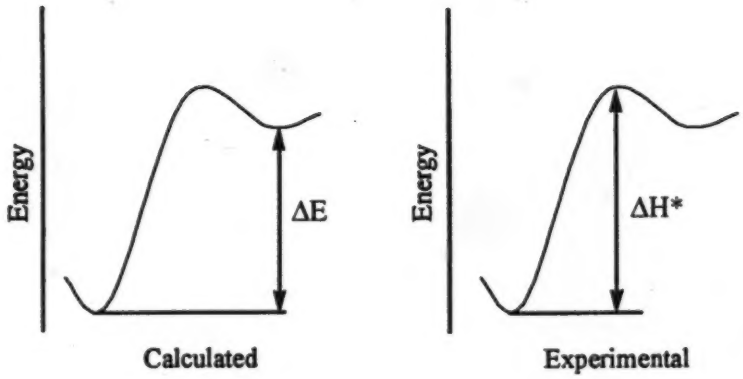

Figure 5-5. Nature of the Calculated and Experimental M-CO Dissociation Energies

Scheme 5-1. Reaction of $Ru(CO)_4(HFB)$ with $Os(CO)_5$

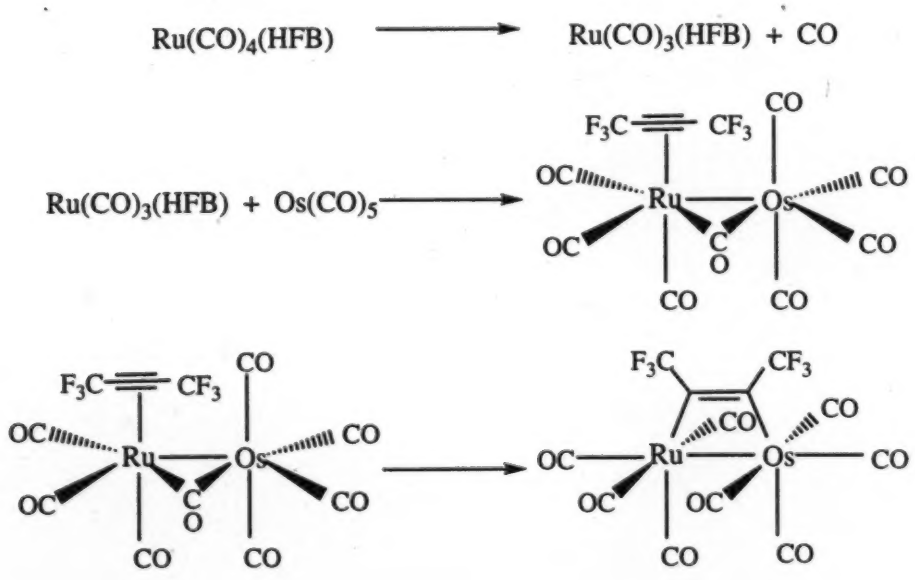

$[Ru(CO)_3(HFB)(\mu\text{-}CO)Os(CO)_4]$. Subsequent breaking of one of the Ru-HFB bonds and transfer to osmium, as the bridging CO moves to a terminal position on ruthenium, produces the bimetallacycle (Scheme 5-1).

The reactants and final bimetallacyclic product involved in this process were optimized and hessians calculated to characterize the stationary points. The C_{2v} symmetry used for the bimetallacyclobutene enabled the hessian to be calculated, otherwise the size of the molecule would have made the calculation impossible on the machines available.

Table 5-7 shows bond distances and the CO stretching frequencies for $Os(CO)_5$ which agree reasonably with experiment at this level of theory. The structure and IR features of the bimetallacyclic product are compared to experiment in Table 5-8.

Table 5-7. Bond Lengths (Å) and CO Stretching Frequencies (cm^{-1}) in $Os(CO)_5$

Parameter	B3LYP	Experiment[17]
$M\text{-}C_{ax}$	1.982	1.982(20)
$M\text{-}C_{eq}$	1.971	1.937(19)
CO_{ax}	1.159	1.130(4)
CO_{eq}	1.166	1.130(4)

Mode	Experiment[18]	B3LYP	Intensity (D^2/Da $Å^2$)	Assignment[a]
23	1993.0	2036.9	34	asym CO_{eq} stretch
24	1993.0	2036.9	34	sym CO_{eq} stretch
25	---	2067.5[b]	0	(sym CO_{ax}) asym to (sym CO_{eq})
26	2035.3	2078.7	39	asym CO_{ax} CO stretch
27	---	2164.9[b]	0	all sym CO stretch

[a] vibrational mode representations shown in Figure 5-6

[b] not IR active

Figure 5-6. Vibrational Modes of $Os(CO)_5$

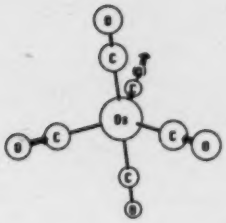

Mode 23

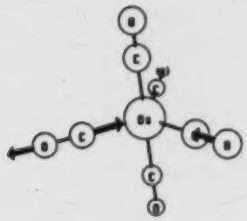

Mode 24

Mode 25

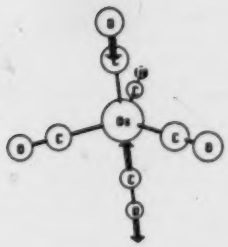

Mode 26

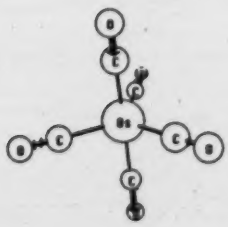

Mode 27

The energy changes for the overall reaction between $Ru(CO)_4(HFB)$ and $Os(CO)_5$ (Scheme 5-1) are -23.4 kcal/mol and -23.5 kcal/mol, ZPE corrected.

Table 5-8. Structure and Characteristic IR Bands of $RuOs(CO)_8(HFB)$

Parameter	B3LYP	Experiment[19] Molecule #1	Experiment[19] Molecule #2
Bond Length (Å)			
Ru-C_{ax}	1.991	1.952(15)	1.947(14)
Ru-C_{eq1}	1.994	1.903(14)	1.928(15)
Ru-C_{eq2}	2.000	1.953(14)	1.976(15)
Os-C_{ax}	1.981	1.960(13)	1.949(14)
Os-C_{eq1}	1.954	1.911(15)	1.917(14)
Os-C_{eq2}	1.980	1.972(15)	1.974(14)
Ru-C	2.144	2.126(14)	2.141(13)
Os-C	2.127	2.156(12)	2.156(12)
C-C	1.354	1.327(18)	1.318(18)
Ru-Os	2.954	2.877(1)	2.885(1)
Angle (°)			
C_{ax}-Ru-C_{ax}	173.4	175.9(6)	169.6(6)
C_{eq}-Ru-C_{eq}	94.7	97.4(6)	95.5(7)
C_{ax}-Os-C_{ax}	170.3	173.1(7)	175.3(6)
C_{eq}-Os-C_{eq}	94.9	96.8(6)	97.0(6)
Ru-C-CF_3	123.3	121.8(10)	122.6(10)
Os-C-CF_3	119.2	121.1(9)	119.9(9)

Mode	B3LYP (cm^{-1})	Experiment[11] (cm^{-1})	Assignment[a]
1	68.2*i*	---	sym CF_3 torsion
2	35.7*i*	---	asym CF_3 torsion
70	1705.8	1602.0	C≡C stretch
71	2068.5	2019.6	Ru(asym eq.) asym to Os(asym eq.)
72	2079.0	---	Ru(asym axial) asym to Os(asym axial)
73	2094.9	2041.8	Ru(sym axial asym to sym eq.) asym to Os(sym axial asym to sym eq.)
74	2100.6	2047.8	see Figure 5-8
75	2110.8	2056.3	asym axial (sym metals)
76	2117.5	---	sym axial asym to sym eq.
77	2143.2	2097.7	Ru CO's asym to Os CO's
78	2185.5	2138.3	all sym CO stretch

[a] vibrational modes shown in Figure 5-8, axial and equatorial CO's are assigned with HFB positioned as shown in Figure 5-8, with equatorial CO's in the HFB plane.

Attempts to optimize intermediates in the reaction were limited by the computer resources available. An initial structure for the proposed intermediate $[Ru(CO)_3(HFB)(\mu\text{-}CO)Os(CO)_3]$ (Figure 5-7) was attempted to be optimized; however, in the process of optimization the system dissociated to reactants. This suggested that the structure could be optimized to a transition state if the initial geometry had one imaginary frequency (which would be followed up to the transition state structure). However, the C_1 symmetry of the structure prohibited the required initial hessian from being calculated in a reasonable amount of time. Lack of third row transition metal parameters also prevented the study from being completed with semi-empirical methods and, at this point, the study was stopped. However, with the available computer resources on the rise, this area can be re-investigated at a later time.

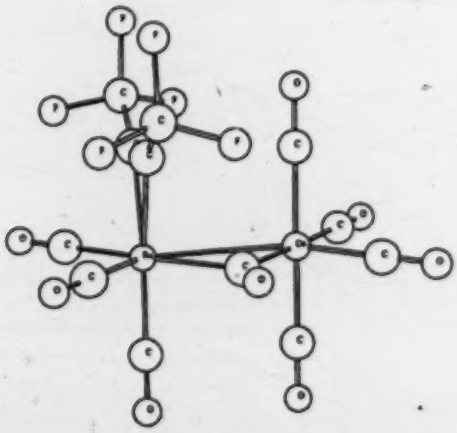

Figure 5-7. Initial Structure of the Proposed Intermediate $[(CO)_3Ru(HFB)(\mu\text{-}CO)Os(CO)_4]$

Figure 5-8. Vibrational Modes of $RuOs(CO)_8(HFB)$

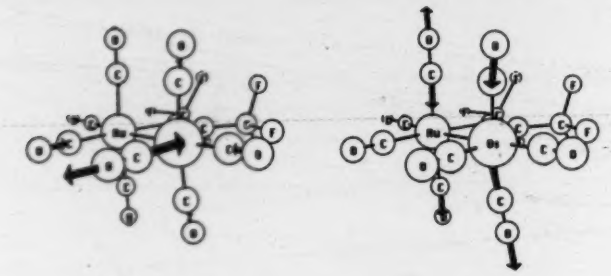

Mode 71 Mode 72

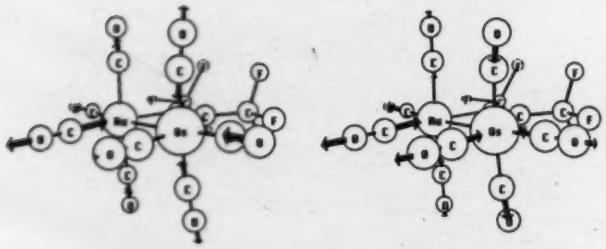

Mode 73 Mode 74

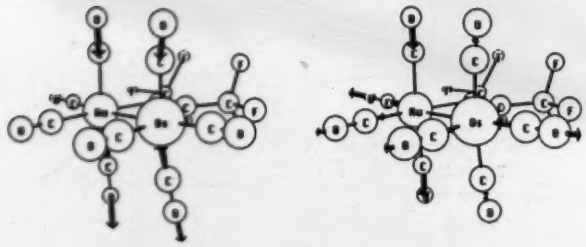

Mode 75 Mode 76

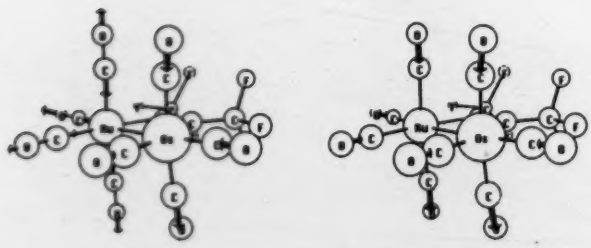

Mode 77 Mode 78

5.3 Conclusions

DFT works quite well for this system, but as shown earlier, accuracy depends drastically on the functional chosen rather than on which basis set is used. This was advantageous for the study, however, as a smaller basis set helped to complete the calculations within a reasonable amount of time.

The major limitation in this study was the size of the system. Nevertheless, it is encouraging that, from the attempts to calculate the intermediate, it seems that the proposed mechanism could be correct. It will be very interesting to complete this study once the computing resources are available.

5.4 References

1. *The Challenge of d and f Electrons: Theory and Computation*; Salahub, D. R.; Zerner, M. C., Eds.; American Chemical Society: Washington, DC, 1989.

2. *Density Functional Methods in Chemistry*; Andzelm, J. W.; Labanowski, J. K., Eds.; Springer-Verlag: New York, 1991.

3. Gaussian 94, Revision D.3, Frisch, M. J.; Trucks, J. W.; Schlegel, H. B.; Gill, P. M. W.; Johnson, B. G.; Robb, M. A.; Cheeseman, J. R.; Keith, T.; Petersson, G. A.; Montgomery, J. A.; Raghavachari, K.; Al-Laham, M. A.; Zakrzewski, V. G.; Ortiz, J. V.; Foresman, J. B.; Cioslowski, J.; Stefanov, B. B.; Nanayakkara, A., Challacombe, M.; Peng, C. Y.; Ayala, P. Y.; Chen, W.; Wong, M. W.; Andres, J. L.; Replogle, E. S.; Gomperts, R.; Martin, R. L.; Fox, D. J.; Binkley, J. S.; Defrees, D. J.; Baker, J.; Stewart, J. P.; Head-Gordon, M.; Gonzalez, C.; and Pople, J. A. Gaussian, Inc., Pittsburgh PA, 1995.

4. Becke, A. D. *J. Chem. Phys.* **1993**, *98*, 5648.

5. Lee, C.; Yang, W.; Parr, R. G. *Phys. Rev. B* **1988**, *37*, 785.

6. Perdew, J. P.; Wang, Y. *Phys. Rev. B* **1992**, *45*, 13244.

7. (a) Stevens, W. J.; Basch, H.; Krauss, M. *J. Chem. Phys.* **1984**, *81*, 6026. (b) Stevens, W. J.; Krauss, M.; Basch, H.; Jasien, P. G. *Can. J. Chem.* **1992**, *70*, 612.

8. Marinelli, G.; Steib, W. E.; Huffman, J. C.; Caulton, K. G.; Gagné, M. R.; Takats, J.; Dartiguenave, M.; Chardon, C.; Jackon, S. A.; Eisenstein, O *Polyhedron* **1990**, *9*, 1867.

9. Stempien, C.; Klobukowski, M. unpublished results.

10. Schaftenaar, G. *QCPE Bulletin* **1992**, *12*, 3 (available from http://www.caos.kun.nl/~schaft/molden).

11. Gagné, M.; Takats, J. *Organometal.* **1988**, *7*, 561.

12. Pearson, J.; Cooke, J.; Takats, J.; Jordan, R. B. *J. Am. Chem. Soc.* **1998**, *120*, 1434.

13. Mao, T.-F.; Zhang, Z.; Washington, J.; Takats, J.; Jordan, R. B. *manuscript in preparation.*

14. Mao, T.-F. Ph.D. Thesis, University of Alberta, 1996.15. (a) Lichtenberger, D. L.; Brown, T. L. *J. Am. Chem. Soc.* **1978**, *100*, 366. (b) Davy, R. D.; Hall, M. B. *Inorg. Chem.* **1989**, *28*, 3524.

16. Decker, S. A.; Klobukowski, M. *J. Am. Chem. Soc.* in press.

17. Huang, J.; Hedberg, K.; Pomeroy, R. K. *Organometal.* **1988**, *7*, 2049.

18. Rushman, P.; van Buuren, G. N.; Shiralian, M.; Pomeroy, R. K. *Organometal.* **1983**, *2*, 693.

19. Gagné, M.; Takats, J.; Day, V. unpublished results.

Chapter Six
Isotope Effects in the Electrophilic Bromination of Cyclohexene

6.1 Introduction

Isotope effects are widely studied in organic chemistry, with growing use in inorganic (organometallic) chemistry, as a tool to look into reaction mechanisms[1], specifically at the bonding changes in the rate-limiting step[2]. The effects arise from changes in the reaction rate when an atom is isotopically substituted in a reactant and are expressed as the ratio of the light/heavy rates (e.g. k_H/k_D) (EIEs are expressed as K_H/K_D, the ratio of equilibrium constants). Changes in the rates (or equilibrium constants) are a direct result of the differences in zero point energy (ZPE) for the light and heavy species. While other isotope pairs have been used, H and D are by far the most common[1] due to the large effects observed (D is twice the mass of H).

Isotope effects (EIE or KIE) are divided into primary and secondary effects. Primary isotope effects occur when the atom that is involved in the bond formation (or bond breaking) is isotopically substituted. An example is the hydrogenation of ethylene where the reactant hydrogen is substituted with D_2.

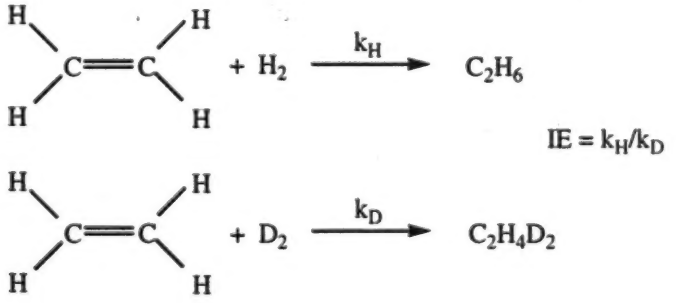

Secondary isotope effects are produced when the spectator atoms in a reaction are isotopically substituted. In the hydrogenation of ethylene this occurs when the ethylene hydrogens are substituted. These effects are generally smaller in magnitude compared to primary isotope effects.

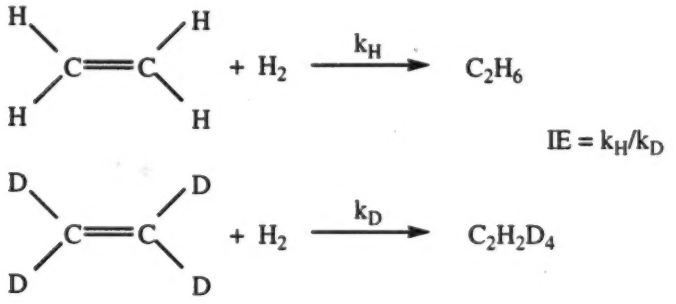

Secondary isotope effects are further classified according to the relative position of the isotopically substituted atom with respect to the reactive center. In the reaction of bromine with cyclohexene, the reactive center is the double bond involving C_1 and C_2 (see Figure 6-1).

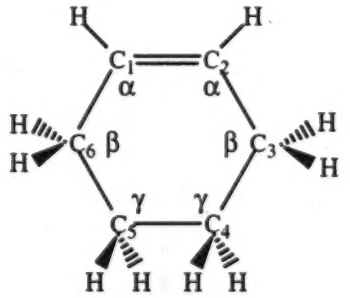

Figure 6-1. Labeling of Cyclohexene

Isotopic substitution of the hydrogens at the α, β, and γ carbons will result in α -, β -, and γ - secondary isotope effects, respectively. The ordering of the effects is usually $\alpha > \beta > \gamma$.

Generally, primary effects are quite large (2 to 7) while secondary effects are a lot closer to unity[1]. However, in the electrophilic bromination of cyclohexene, the experimentally observed secondary KIE is $\frac{k_D}{k_H} = 1.9 \pm 0.15$ (inverse) in acetic acid at 25 °C [3]. Because the isotope effect was so large, it was of interest, first, to see if theory could reproduce the experimental values and, second, to determine the origin of the inverse effect. The results presented in this chapter have already been published[4].

6.2 Computational Details

Density Functional Theory was the principal method used in the calculations, as found in the Gaussian 94 program[5]. Becke's exchange (B)[6] and Becke's 3-parameter exchange (B3)[7] were combined with the correlation functionals of Lee, Yang, and Parr (LYP)[8] and Perdew (P86)[9] to produce three functional combinations. The chosen functionals are non-local (or gradient corrected), which have been shown to be very successful in studies of isotope effects[10]. Restricted Hartree-Fock calculations were also done for comparison with the DFT results. The compact effective core potentials (ECP) of Stevens *et al.*[11] were used to help reduce the computational effort. The basis sets were used with double - ζ contraction (DZV) on the carbon atoms and quadruple - ζ contraction (QZV) on the bromine atom, along with the (31) basis set for the hydrogens obtained from Huzinaga's (4s)[13] expansion. Single polarization functions were added: d-type on all heavy atoms and p-type on hydrogens. Polarization functions were included in the hydrogen basis set since it is the effect of the hydrogen atoms on the vibrational structure and the proximity and interactions of hydrogens with the reaction site which are important in this study. C_1 symmetry was used in all of the calculations allowing for the maximum number of degrees of freedom in the structures calculated.

6.3 Development of the System to be Studied Computationally

The experimentally observed isotope effects (KIE) reflect the change in the reaction rate, going from the reactants C_6R_{10} (R = H, D) + Br_2 to the transition state, upon isotopic substitution, but the calculated bridged bromonium complex used in this study is a minimum rather than being a transition state. In solution, it is presumed that the transition state resembles the ion pair of $C_6H_{10}Br^+$ and bromide. However, the true transition state for the process cannot be calculated in the gas phase due to the prohibitive endothermicity associated with charge separation. Indeed, it is well known that electrophilic bromination does not occur in the gas phase for the same reason. It may be assumed that the cyclohexenyl bromonium ion resembles the transition state more than the reactants do based on the Hammond postulate[14]. Therefore, the bromonium ion can be used as a qualitative substitute for the actual transition state in the gas phase calculations. The calculations were done for the equilibrium isotope effect (EIE) in the equilibrium involving the formation of the reaction intermediate $[C_6H_{10}Br]^+$:

$$C_6H_{10} + Br^+ \rightleftharpoons [C_6H_{10}Br]^+$$

For the equilibrium:

$$R \rightleftharpoons P$$

the EIE was calculated in the gas phase, rigid rotor, harmonic oscillator approximation according to equation (1-43) of Chapter One, which is written here as:[14]

$$\frac{K_H}{K_D} = \frac{Q_P}{Q_R}\frac{Q_{R'}}{Q_{P'}} e^{-(\delta E_o^P - \delta E_o^R)/RT} = F_Q \cdot F_{ZPE} \qquad (6\text{-}1)$$

where δE_o^R is the difference between the total molar vibrational zero-point energies for the light and heavy reactant compounds R and R′, δE_o^P is the difference between the total molar vibrational zero-point energies for the light and heavy product compounds P and P′, and Q is the total molar partition function. The

factors, F_Q and F_{ZPE}, refer to the partition function and exponential terms, respectively.

6.4 Results

The two conformers of the reactant cyclohexene, twist (TR) and boat (BR), along with the three conformers of the product cyclohexenyl bromonium ion, twist (TP), boat up (BU), and boat down (BD), were calculated using all three density functionals (Figure 6-2). Table 6-1 lists the relative energies of the conformers for each functional and the RHF method. With both cyclohexene and the bromonium ion the twist conformer is the most stable, but the differences in energy between the conformers are relatively small: BR is ~5 kcal/mol higher than TR while BD is only 2 kcal/mol less stable. As well, the bromonium ion is about 130 kcal/mol more stable than the reactants Br^+ and C_6H_{10}. All three functionals give practically identical results. The RHF results are comparable to DFT with conformer energy spacings that are ~1 kcal/mol larger and a reaction exothermicity that is 30-40 kcal/mol smaller.

Table 6-1. Relative Energies (kcal/mol) of the Conformers

System	RHF	BP86	BLYP	B3LYP
Cyclohexene				
TR	0	0	0	0
BR	6.2	5.1	5.0	5.3
Cyclohexenyl Bromonium Ion				
TP	0	0	0	0
BD	2.8	1.4	1.6	1.8
BU	5.7	4.5	4.5	4.8
$\Delta E_{reaction}$[a] (kcal/mol)	-93.8	-131.9	-124.6	-123.3

[a] the reaction is $C_6H_{10} + Br^+ \rightleftharpoons [C_6H_{10}Br]^+$

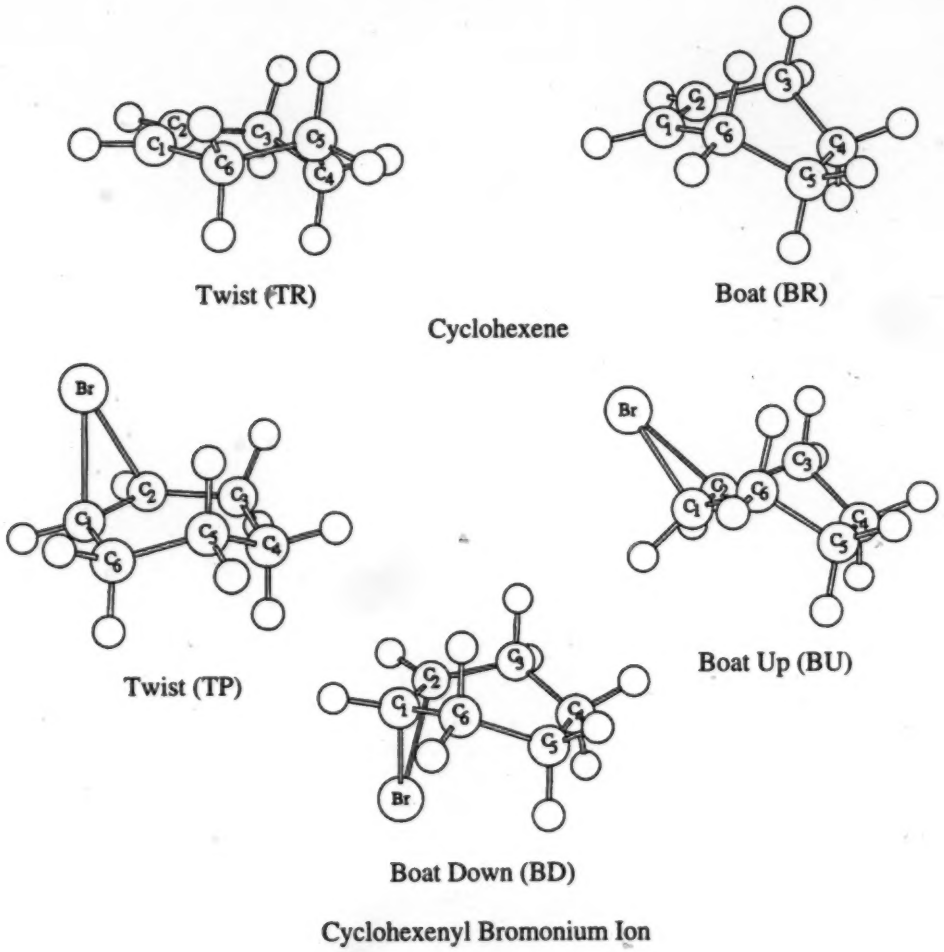

Figure 6-2. Structures of the Cyclohexene and Cyclohexenyl Bromonium Ion Conformations

Table 6-2 lists the B3LYP-calculated structural parameters for the systems studied, with the results from RHF and the remaining functionals available in the Appendix. The DFT bond lengths are longer than the RHF ones due to the lack of electron correlation in Hartree-Fock theory, with the three DFT functionals producing similar structures. The B3LYP functional, which contains Hartree-Fock exchange (see Chapter One), gives shorter bond lengths. The bond lengths differ by about 0.04 Å and there is a 0.6° variance in the angles. The C_1-C_2 bond

lengthens upon bromination from 1.36 Å to 1.47Å, forming almost a single bond. The C-C bonds are also longer in the boat conformations when compared to the twist structures.

Table 6-2. Geometry of the Conformers Calculated Using B3LYP

Parameter[a]	Cyclohexene		Cyclohexenyl Bromonium Ion		
	TR	BR	TP	BD	BU
Bond Length (Å)					
C_1 - C_2	1.364	1.363	1.447	1.473	1.475
C_2 - C_3	1.525	1.522	1.523	1.507	1.514
C_3 - C_4	1.548	1.560	1.556	1.552	1.573
C_4 - C_5	1.547	1.568	1.546	1.567	1.569
C_5 - C_6	1.548	1.560	1.545	1.552	1.572
C_6 - C_1	1.525	1.522	1.511	1.507	1.515
C_1 - H	1.108	1.107	1.104	1.104	1.104
C_6 - H	1.112	1.115	1.108	1.120	1.105
C_1 - Br			2.127	2.129	2.120
Angle (°)					
C_2 - C_1 - C_6	123.3	118.4	120.7	118.5	116.2
C_1 - C_6 - C_5	111.9	111.0	113.8	115.6	105.7
C_6 - C_5 - C_4	110.9	113.4	110.6	115.6	113.3
C_6 - C_1 - H	117.5	120.3	118.4	118.9	120.1
C_1 - C_6 - H	109.5	109.1	110.0	110.2	110.9
C_6 - C_1 - Br			114.6	116.3	117.3
C_2 - C_1 - Br			70.2	69.8	69.6

[a] parameter definitions are given in Figure 6-1

Table 6-3 compares the calculated cyclohexene structure to experiment; the cyclohexenyl bromonium ion has not been experimentally characterized. There is good agreement between the experimental and calculated results. The calculated bond lengths are longer by 0.02 Å, which can most likely be attributed to an insufficiently flexible set of polarization functions within the basis sets.

The experimental cyclohexene infrared spectrum is compared to the calculated spectra for the twist conformer in Figure 6-3. There is remarkable agreement between the two and all of the major bands can be assigned unambiguously. The calculated harmonic vibrational modes with significant

Table 6-3. Comparison of Experimental and Calculated Geometry for the Twist Conformer of Cyclohexene

Parameter	B3LYP	Experiment[15]
Bond Length (Å)		
C_1 - C_2	1.364	1.334
C_2 - C_3	1.525	1.502
C_3 - C_4	1.548	1.515
C_4 - C_5	1.547	1.537
C_5 - C_6	1.548	1.515
C_6 - C_1	1.525	1.502
C_1 - H	1.108	1.1
C_6 - H	1.112	1.1
Angle (°)		
C_2 - C_1 - C_6	123.3	123.4
C_1 - C_6 - C_5	111.9	111.9
C_6 - C_5 - C_4	110.9	110.9
C_6 - C_1 - H	117.5	118.3
C_1 - C_6 - H	109.5	110.3
C_1 - C_2 - H	119.2	118.3

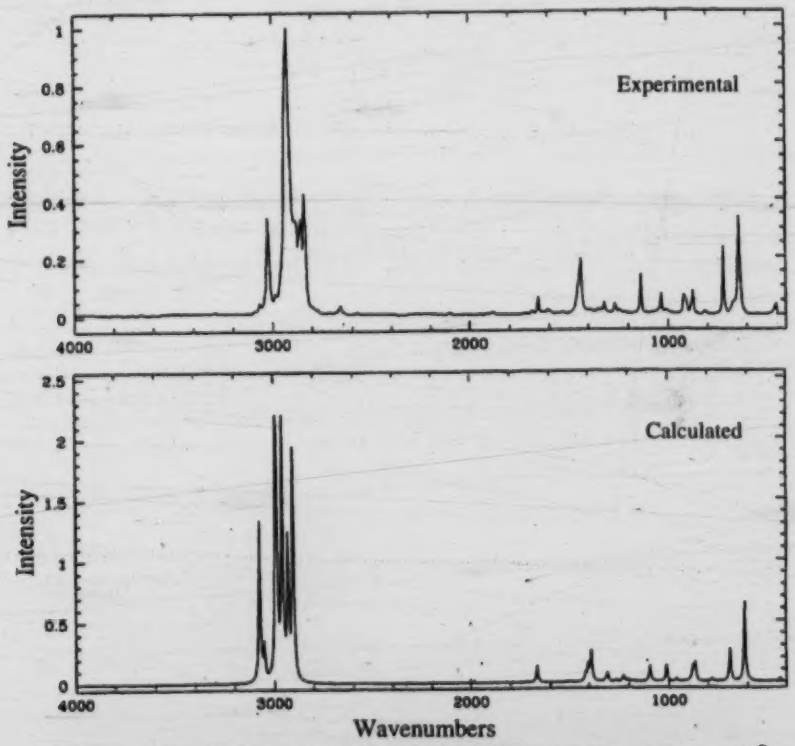

Figure 6-3. Calculated (unscaled BP86) and Experimental (neat) IR Spectra of Cyclohexene. Intensity units are $D^2Da^{-1}Å^{-2}$ for the calculated spectrum and arbitrary units for the experimental spectrum.

intensities were visualized using MOLDEN[16] and MacMolPlt[17] and the resulting assignment is given in Table 6-4. It must be stressed here, as it will prove important in the analysis of the isotope effects, that apart from the ten modes corresponding to CH stretches (eight of which are listed in Table 6-4), all other vibrations present a complex mixture of CH_2 bends and CC stretches leading to the ring puckering motion.

Table 6-4. Vibrational Assignment of the Major IR Bands in Cyclohexene's Twist Conformer (cm^{-1})

Mode	Expt.[18]	BP86[a]	Assignment
1	642	614	out-of-plane CH bending at C_1, C_2
2	720	689	out-of-plane CH bending at C_1, C_2
3	875	865	ring deformation: C_1C_6 and C_5C_6 stretch, C_2C_3 and C_3C_4 shorten
4	918	878	rocking CH_2 at C_3, C_6, twisting CH_2 at C_4, C_5
5	1036	1012	ring deformation: C_1C_6 and C_3C_4 stretch, C_2C_3 and C_5C_6 shorten
6	1137	1095	twisting CH_2 at C_3-C_6
7	1267	1227	twisting CH_2 at C_3-C_6
8	1322	1310	twisting CH_2 at C_3-C_6
9	1439	1389	out-of-phase CH_2 scissoring at C_3, C_6
10		1405	out-of-phase CH_2 scissoring (sym) at C_4, C_5
11		1418	in-phase CH_2 scissoring (sym) at C_4, C_5
12	1654	1664	C=C stretch
13	2841	2904	out-of-phase CH_2 stretching (sym) at C_3, C_6
14	2859	2930	in-phase CH_2 stretching (sym) at C_4, C_5
15		2931	out-of-phase CH_2 stretching (sym) at C_4, C_5
16	2889	2959	stretching CH_2 (asym) at C_3, C_6
17	2928	2987	stretching CH_2 (asym) at C_4, C_5 out of phase
18		2993	stretching CH_2 (asym) at C_4, C_5 in phase
19	3025	3049	out-of-phase stretching CH at C_1, C_2
20		3073	in-phase stretching CH at C_1, C_2

[a] frequencies are unscaled

Using the most stable conformers, TR and TP, equilibrium isotope effects were calculated at 298.15 K and 1 atm pressure using equation (6-1) for the following isotopomers: D_{10}, D_8, D_4, D_2, D_1, D_2-syn and D_2-anti (Scheme 6-1). Table 6-5 lists the calculated results and the experimentally determined KIEs for the bromination of cyclohexene in methanol at 25 °C. There is good agreement

between theory and experiment, supporting the validity of the Hammond postulate in the bromination of cyclohexene. Again, the DFT functionals show little variance in the results produced. However, the RHF calculations produce results that are, in most cases, significantly different from both experiment and DFT results.

Table 6-5. Calculated EIE (K_D/K_H) for the Bromination of Cyclohexene

System[a]	K_D/K_H				k_D/k_H
	RHF	BP86	BLYP	B3LYP	Expt.[4]
D_{10}	2.78	1.41	1.41	1.48	1.45(0.18)
D_8	1.96	1.14	1.15	1.18	1.10(0.15)
D_4	1.37	1.02	1.01	1.04	0.97(0.15)
D_2	1.37	1.23	1.23	1.25	1.31(0.17)
D_1	1.15	1.11	1.11	1.12	1.18(0.15)
D_2 syn	1.15	1.05	1.05	1.05	
D_2 anti	1.15	1.07	1.07	1.07	

[a] defined in Scheme 6-1

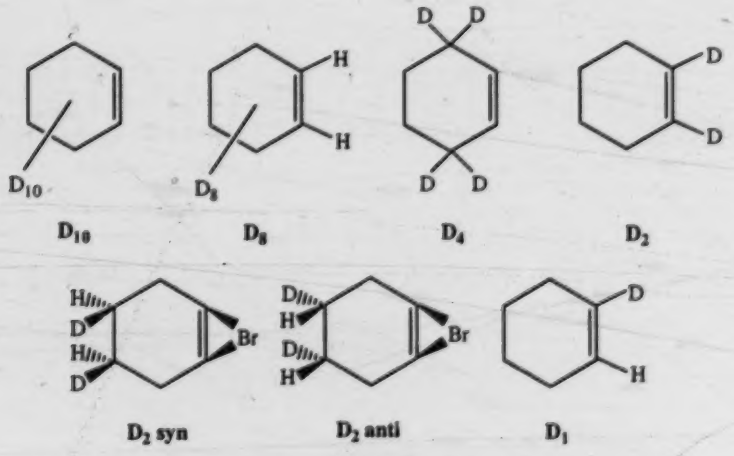

Scheme 6-1. Isotopomers of Cyclohexene

The perdeuterated isotopomer, D_{10}, gives the largest EIE both in the calculation and experiment. By comparing the remaining isotopomers, the major contributors to this large isotope effect can be established. Substitution of the two

hydrogens at the vinyl α-carbons produces the largest contribution, with K_D/K_H = 1.25. This contribution is followed by the D_8 isotopomer's K_D/K_H = 1.18 where all of the methylene hydrogens are substituted. A modest inverse isotope effect of K_D/K_H = 1.04 is calculated for the D_4 isotopomer where the hydrogens of the β-carbons are substituted, while the experimental effect is normal, but very minor. Interestingly, the isotope effect calculated when the hydrogens on the γ-carbons are substituted, K_D/K_H = 1.12 (BP86, not shown in Table 6-5), is comparable to the D_8 isotopomer's effect which involves both the β- and γ-carbons. This effect was investigated further to determine if there was a steric origin. Two deuteriums were substituted in the syn positions (with respect to bromine), D_2-syn, and in the anti positions, D_2-anti, and the calculated equilibrium isotope effects are shown in Table 6-5. The EIEs are essentially equivalent with all of the methods employed, ruling out a steric origin of the γ-isotope effect.

The magnitude of the experimentally determined KIE varies with the solvent that is used: $k_D/k_H = 1.9 \pm 0.15$ in acetic acid and $k_D/k_H = 1.45 \pm 0.18$ in methanol, both at 25 °C. However, both experiment and theory predict similar trends in the magnitude of the isotope effects: from experiment, $D_{10} > D_2 > D_1 \approx D_8 > D_4$, whereas calculations show $D_{10} > D_2 > D_8 > D_1 > D_4$.

One of the goals of this study was to investigate the origin of the isotope effect by identifying the vibrational mode(s) responsible for the unusually large, inverse EIE. However, the cyclohexene ring structure gives rise to numerous soft vibrational modes in which the ring puckering vibrations are mixed with the rocking, twisting, and wagging vibrations of the methylene units, making it difficult to establish a one-to-one correspondence between the reactant and product vibrations. The analysis does indicate that the partition function component, F_Q, in equation (6-1) is very close to unity; therefore, the zero-point energy component, F_{ZPE}, (the exponential term in eq. (6-1)) controls the EIE. The

ZPE component is a relative measure of how the zero-point energy changes upon deuteration for the reactant and product species.

While a unique mapping of vibrational modes from reactant to product could not be developed, the modes could be separated into stretching and bending vibrations, and the values of δE and F_{ZPE} decomposed accordingly. All of the ten C-H stretches (ten modes) could be unambiguously identified and were separated from the remaining modes, which were mainly bends but also included coupling to stretches of the C-C bonds in the cyclohexene ring. For each group of vibrations, contributions to the overall EIE were evaluated separately, as shown in Table 6-6. Since the F_Q factor is close to unity, the value of F_{ZPE} directly determines the nature of the isotope effect and is related to the magnitude of $\delta E_o^Y - \delta E_o^X$, equation (6-1). When $F_{ZPE} > 1$ the effect is normal and when $F_{ZPE} < 1$ the effect is inverse; the equilibrium constant is not affected upon deuteration when $F_{ZPE} \cong 1$.

Table 6-6. Bending and Stretching Contributions to the BP86 Calculated EIE

System	F_Q	δE_o^{bend}	$\delta E_o^{stretch}$	δE_o [a]	F_{ZPE}^{bend}	$\delta E_{ZPE}^{stretch}$	F_{ZPE} [b]	K_H/K_D	K_D/K_H
D_{10}	1.13	0.67	0.48	1.15	0.76	0.82	0.63	0.71	1.41
D_8	1.03	-0.02	0.43	0.41	1.01	0.84	0.85	0.87	1.14
D_4	1.02	-0.10	0.21	0.10	1.04	0.92	0.96	0.98	1.02
D_2	1.10	0.70	0.05	0.75	0.75	0.98	0.74	0.81	1.23
D_1	1.05	0.35	0.02	0.37	0.87	0.99	0.86	0.90	1.11
D_2 syn	1.00	0.01	0.12	0.12	1.00	0.95	0.95	0.96	1.05
D_2 anti	1.01	0.07	0.11	0.18	0.97	0.96	0.93	0.94	1.07

[a] $\delta E_o = \delta E_o^{bend} + \delta E_o^{stretch}$

[b] $F_{ZPE} = F_{ZPE}^{bend} \cdot F_{ZPE}^{stretch}$

The results shown in Table 6-6 indicate that there are practically no bending contributions to the EIE for the D_8 and D_4 isotopomers with the isotope effect arising solely from changes in the stretching vibrational frequencies. However, with the D_1 and D_2 isotopomers, the situation is reversed with the bending vibrations being responsible for the effect. To look closer at the EIE, the stretching vibrations of the D_8 isotopomer were individually analyzed.

In Table 6-7, the calculated vibrational frequencies for the hydrogenated and deuterated reactant and product species are given. While the wavenumber difference between the light and heavy species is substantial (~800 cm^{-1}), there is a much smaller change between the reactant and product differences, $\Delta(\Delta\nu)$. This latter difference forms the contribution to the overall F_{ZPE} factor with $\delta E_o = \frac{1}{2}\sum_i \Delta(\Delta\nu_i)$ and $F_{ZPE} = e^{-hc\,N_A(\delta E_o)/RT}$.

Table 6-7. Analysis of the BP86 Calculated Stretching Modes (cm^{-1}) in the D_8 Isotopomer

Cyclohexene			Cyclohexenyl Bromonium Ion			$\Delta(\Delta_\nu)^b$
$\nu(C_6H_{10})$	$\nu(D_8\text{-}C_6H_{10})$	$\Delta_\nu(R)^a$	$\nu(C_6H_{10}Br^+)$	$\nu(D_8\text{-}C_6H_{10}Br^+)$	$\Delta_\nu(P)^a$	
2903	2117	786	2894	2115	779	-7
2904	2117	787	2948	2150	798	11
2929	2139	790	2960	2162	798	8
2931	2134	797	2968	2164	804	7
2959	2189	770	2995	2216	779	9
2959	2190	769	3011	2224	787	18
2987	2214	773	3033	2248	785	12
2993	2220	773	3039	2253	786	13
3049	3049	---	3066	3066	---	---
3073	3073	---	3077	3077	---	---

[a] $\Delta_\nu = \nu - \nu(D_8)$

[b] $\Delta(\Delta_\nu) = \Delta_\nu(P) - \Delta_\nu(R)$, in cm^{-1}.

Interestingly, while the C-H stretches are indeed responsible for the isotope effect (Table 6-7) there is not any particular vibrational mode that is exclusively responsible for the effect. In conclusion, it must be stressed that the isotope effects in the cyclohexene system result from complex interactions between all vibrational modes, in contrast with the simplified picture often presented in textbooks.

6.5 Models of the Origin of Isotope Effects

The origin of α - effects has been explained using two different models depending on reaction characteristics. The more common model, proposed by Streitwieser[19], states that the effect arises from the change in C-H bending modes

due to the rehybridization of carbons from sp^2 to sp^3. The second model, developed by Strausz, attributes the α - effect to the creation of new, isotopically sensitive modes in the transition state[20]. After studying the bromination of cyclohexene, it still could not be determined which model applies to this system. In the reactant geometry, the α - carbons in cyclohexene are sp^2 hybridized with the angles around each olefinic carbon summing to 360°. However, in the bromonium ion, the sum of the angles is 356°, a small change from sp^2 hybridization (the angles sum to 330° for sp^3 hybridization). There are three new vibrational modes in the bromonium ion, all of which are associated with the CCBr ring and occur at very low wavenumbers (90-400 cm^{-1}). These modes are also coupled to motion within the cyclohexene ring, complicating the analysis. It is not apparent from this study, due to the inability to map the modes from cyclohexene to the bromonium ion, if these modes are indeed responsible for the observed inverse effect.

6.6 Conclusions

The magnitude of the calculated isotope effects agrees well with the experimentally observed isotope effects for all of the isotopomers studied, giving more credibility to the DFT method in calculating isotope effects.

While cyclohexene is not considered a large system to work with experimentally, the complex nature of the associated vibrational frequencies drastically hinders the theoretical study. Although the origin of the isotope effect cannot be attributed to a single vibrational mode, this study does isolate groups of modes that together produce the effect. For the D_8 and D_4 isotopomers, the C-H stretching vibrations alone are responsible for the effect in contrast to the D_1 and D_2 isotopomers where the remaining modes generate the effect.

6.7 References

1. Lowry, T. H.; Richardson, K. S. *Mechanism and Theory in Organic Chemistry*, 3rd ed.; Harper and Row: New York, 1987; p 232-241.

2. Carroll, F. A. *Perspectives on Structure and Mechanism in Organic Chemistry*, Brooks/Cole: Pacific Grove, CA, 1998; p 349-365.

3. Slebocka-Tilk, H.; Zheng, C. Y.; Brown, R. S. *J. Am. Chem. Soc.* **1993**, *115*, 1347.

4. Slebocka-Tilk, H.; Neverov, A.; Motallebi, S.; Brown, R. S.; Donini, O.; Gainsforth, J. L.; Klobukowski, M. *J. Am. Chem. Soc.* **1998**, *120*, 2578.

5. Gaussian 94, Revision D.3, Frisch, M. J.; Trucks, J. W.; Schlegel, H. B.; Gill, P. M. W.; Johnson, B. G.; Robb, M. A.; Cheeseman, J. R.; Keith, T.; Petersson, G. A.; Montgomery, J. A.; Raghavachari, K.; Al-Laham, M. A.; Zakrzewski, V. G.; Ortiz, J. V.; Foresman, J. B.; Cioslowski, J.; Stefanov, B. B.; Nanayakkara, A., Challacombe, M.; Peng, C. Y.; Ayala, P. Y.; Chen, W.; Wong, M. W.; Andres, J. L.; Replogle, E. S.; Gomperts, R.; Martin, R. L.; Fox, D. J.; Binkley, J. S.; Defrees, D. J.; Baker, J.; Stewart, J. P.; Head-Gordon, M.; Gonzalez, C.; and Pople, J. A. Gaussian, Inc., Pittsburgh PA, 1995.

6. Becke, A. D. *Phys. Rev. A* **1988**, *38*, 3098.

7. Becke, A. D. *J. Chem. Phys.* **1993**, *98*, 5648.

8. Lee, C.; Yang, W.; Parr, R. G. *Phys. Rev. B* **1986**, *37*, 785.

9. Perdew, J. P. *Phys. Rev. B* **1986**, *33*, 8822.

10. Wiest, O.; Black, K. A.; Houk, K. N. *J. Am. Chem. Soc.* **1994**, *116*, 10336.

11. (a) Stevens, W. J.; Basch, H.; Krauss, M. *J. Chem. Phys.* **1984**, *81*, 6026. (b) Stevens, W. J.; Krauss, M.; Basch, H.; Jasien, P. G. *Can. J. Chem.* **1992**, *70*, 612.

12. Huzinaga, S. *J. Chem. Phys.* **1965**, *42*, 1293.

13. Ruasse, M.-F.; Motallebi, S. *J. Phys. Org. Chem.* **1991**, *4*, 527.

14. Maskill, H. *The Physical Basis of Organic Chemistry*; Oxford University Press: New York, 1985. Also see: van Hook, W. A. In *Isotope Effects in Chemical Reactions*; Collins, C. J.; Bowman, N. S., Eds.; Van Nostrand: New York, 1970.

15. Geise, H. J.; Buys, H. R. *Recl. Trav. Chim. Pays-Bas* **1970**, *89*, 1147.

16. Schaftenaar, G. *QCPE Bulletin* **1992**, *12*, 3 (available from http://www.caos.kun.nl/~schaft/molden).

17. MacMolPlt is available from http://www.msg.ameslab.gov/GAMESS/Graphics/MacMolPlt.html.

18. C6H10 vibrational modes experimental numbers

19. Streitwieser, A.; Jagow, R. H.; Fehey, R. C.; Suzuki, S. *J. Am. Chem. Soc.* **1958**, *80*, 2326.

20. Strausz, O. P.; Safarik, I.; O'Callaghan, W. B.; Gunning, H. E. . *J. Am. Chem. Soc.* **1972**, *94*, 1828.

6.8 Appendix : Calculated Structural Parameters

Table 6-A1. Structural Parameters for Twist Cyclohexene

Parameter[a]	RHF[b]	BP86[b]	BLYP[b]	B3LYP
Bond Length (Å)				
C_1 - C_2	-0.017	0.009	0.010	1.364
C_2 - C_3	-0.005	0.001	0.008	1.525
C_3 - C_4	-0.010	0.003	0.011	1.548
C_4 - C_5	-0.011	0.003	0.011	1.547
C_5 - C_6	-0.010	0.003	0.011	1.548
C_6 - C_1	-0.005	0.001	0.028	1.525
C_1 - H	-0.014	0.008	0.007	1.108
C_6 - H	-0.013	0.008	0.008	1.112
Angle (°)				
C_2 - C_1 - C_6	0.1	-0.1	0.0	123.3
C_1 - C_6 - C_5	-0.2	0.1	0.1	111.9
C_6 - C_5 - C_4	0.1	0.0	0.0	110.9
C_6 - C_1 - H	-0.1	0.1	0.0	117.5
C_1 - C_6 - H	-0.1	0.1	0.1	109.5

[a] parameters are defined in Figure 6-1

[b] difference from B3LYP geometry: Method - B3LYP, Method = RHF, BP86, BLYP

Table 6-A2. Structural Parameters for Boat Cyclohexene

Parameter[a]	RHF[b]	BP86[b]	BLYP[b]	B3LYP
Bond Length (Å)				
C_1 - C_2	-0.018	0.009	0.010	1.363
C_2 - C_3	-0.003	0.001	0.008	1.522
C_3 - C_4	-0.013	0.004	0.012	1.560
C_4 - C_5	-0.010	0.002	0.012	1.568
C_5 - C_6	-0.013	0.004	0.012	1.560
C_6 - C_1	-0.003	0.001	0.008	1.522
C_1 - H	-0.013	0.008	0.007	1.107
C_6 - H	-0.014	0.008	0.008	1.115
Angle (°)				
C_2 - C_1 - C_6	0.3	-0.2	0.1	118.4
C_1 - C_6 - C_5	0.0	0.0	0.1	111.0
C_6 - C_5 - C_4	0.3	-0.1	0.0	113.4
C_6 - C_1 - H	-0.3	0.2	-0.1	120.3
C_1 - C_6 - H	-0.1	0.0	0.1	109.1

[a] parameters are defined in Figure 6-1

[b] difference from B3LYP geometry: Method - B3LYP, Method = RHF, BP86, BLYP

Table 6-A3. Structural Parameters for Twist Cycylohexenyl Bromonium Ion

Parameter[a]	RHF[b]	BP86[b]	BLYP[b]	B3LYP
Bond Length (Å)				
C_1 - C_2	-0.021	0.012	0.012	1.477
C_1 - Br	-0.025	-0.006	0.036	2.127
C_2 - C_3	0.004	-0.002	0.005	1.523
C_3 - C_4	-0.012	0.003	0.012	1.556
C_4 - C_5	-0.010	0.003	0.011	1.546
C_5 - C_6	-0.008	0.002	0.011	1.545
C_6 - C_1	0.004	-0.001	0.006	1.511
C_1 - H	-0.015	0.009	0.007	1.104
C_6 - H	-0.014	0.008	0.007	1.108
Angle (°)				
C_2 - C_1 - C_6	0.4	-0.3	-0.1	120.7
C_1 - C_6 - C_5	-0.4	0.1	0.2	113.8
C_6 - C_5 - C_4	0.0	0.1	0.1	110.6
C_6 - C_1 - H	-0.3	0.1	0.1	118.4
C_1 - C_6 - H	-0.5	0.2	0.2	110.0
C_6 - C_1 - Br	-0.5	0.1	0.2	114.6
C_2 - C_1 - Br	0.3	-0.2	0.4	70.2

[a] parameters are defined in Figure 6-1

[b] difference from B3LYP geometry: Method - B3LYP, Method = RHF, BP86, BLYP

Table 6-A4. Structural Parameters for Boat-down Cyclohexenyl Bromonium Ion

Parameter[a]	RHF[b]	BP86[b]	BLYP[b]	B3LYP
Bond Length (Å)				
C_1 - C_2	-0.021	0.011	0.011	1.473
C_1 - Br	-0.023	-0.004	0.039	2.129
C_2 - C_3	0.003	-0.001	0.005	1.507
C_3 - C_4	-0.009	0.002	0.011	1.552
C_4 - C_5	-0.010	0.002	0.011	1.567
C_5 - C_6	-0.010	0.002	0.011	1.552
C_6 - C_1	0.003	-0.001	0.005	1.507
C_1 - H	-0.015	0.009	0.007	1.104
C_6 - H	-0.017	0.009	0.009	1.120
Angle (°)				
C_2 - C_1 - C_6	0.1	-0.1	0.1	118.5
C_1 - C_6 - C_5	-0.4	0.2	0.3	115.6
C_6 - C_5 - C_4	0.1	0.0	0.0	115.6
C_6 - C_1 - H	0.0	0.1	0.1	118.9
C_1 - C_6 - H	0.6	-0.3	-0.4	101.2
C_6 - C_1 - Br	-0.6	0.2	0.2	116.3
C_2 - C_1 - Br	0.1	-0.2	0.2	69.8

[a] parameters are defined in Figure 6-1

[b] difference from B3LYP geometry: Method - B3LYP, Method = RHF, BP86, BLYP

Table 6-A5. Structural Parameters for Boat-up Cyclohexenyl Bromonium Ion

Parameter[a]	RHF[b]	BP86[b]	BLYP[b]	B3LYP
Bond Length (Å)				
C_1 - C_2	-0.021	0.012	0.012	1.475
C_1 - Br	-0.021	-0.008	0.037	2.120
C_2 - C_3	0.004	-0.001	0.005	1.514
C_3 - C_4	-0.018	0.004	0.016	1.573
C_4 - C_5	-0.009	0.002	0.010	1.569
C_5 - C_6	-0.018	0.004	0.016	1.572
C_6 - C_1	0.004	-0.001	0.005	1.515
C_1 - H	-0.015	0.009	0.007	1.104
C_6 - H	-0.013	0.009	0.008	1.105
Angle (°)				
C_2 - C_1 - C_6	0.1	-0.2	0.2	116.2
C_1 - C_6 - C_5	0.8	-0.6	-0.3	105.7
C_6 - C_5 - C_4	0.2	0.0	0.1	113.3
C_6 - C_1 - H	0.2	-0.2	0.0	120.1
C_1 - C_6 - H	-0.6	0.4	0.3	110.9
C_6 - C_1 - Br	-1.2	0.6	0.4	117.3
C_2 - C_1 - Br	0.2	-0.2	0.3	69.6

[a] parameters are defined in Figure 6-1

[b] difference from B3LYP geometry: Method - B3LYP, Method = RHF, BP86, BLYP

Chapter Seven
Isotope Effects in the
Electrophilic Bromination of Ethylene

7.1 Introduction

Using statistical mechanics as developed in Chapter One, it is possible to study the origin of the isotope effect of a particular reaction. However, the ability to isolate vibrational modes that are responsible for the observed effect is dependent on the system being studied. As shown in Chapter Six, the system must be small and simple enough so that the vibrational modes can be mapped from reactant to product (or transition state). Once such one-to-one correspondence between reactant and product modes is made, the isotope effect can be factored into individual vibrational mode contributions which should indicate the origin of the effect. The electrophilic bromination of ethylene, like cyclohexene, has a fairly large inverse isotope effect and, in addition, its vibrational modes are easier to interpret. Therefore, the isotope effects for the electrophilic bromination of ethylene were studied in detail with focus on determining the origin of the observed effect. The results presented in this Chapter have already been published[1].

7.2 Computational Methods

7.2.1 Methodological Details

A computational study was undertaken to examine the equilibrium isotope effect (EIE) for the equilibrium involving the formation of the ethylene bromonium ion from ethylene plus Br^+. The isotope effects were modeled using results obtained with the Density Functional Theory (DFT) as found in the Gaussian 94 program[2]. Gradient-corrected (non-local) functionals are very successful in kinetic isotope effect studies[3] and work on the cyclohexene system (Chapter Six) has shown that various functionals produce quite similar results. Therefore, only one set of gradient-corrected functionals was used in this work:

Becke's 3-parameter exchange[4] functional was combined with the Lee, Yang, and Parr correlation[5] functional, denoted as B3LYP. To minimize the computational effort, the compact effective core potentials (ECP) of Stevens *et al.*[6] were used. The basis set for carbon was used in the original double-ζ contraction (31/31) while that for bromine was modified to give a quadruple-ζ contraction (2111/2111). A single d-type polarization function was added to carbon (α_d = 0.80) and bromine (α_d = 0.389). The (31) basis set from Huzinaga's (4s) expansion[7] was used for the hydrogens with a single p-type polarization function (α_p = 1.1) added. As the present study focuses on the effect of hydrogens on the vibrational structure and on the proximity and interactions of hydrogens with the reaction site, the addition of polarization functions on hydrogens is necessary to get a better description of these atoms.

7.2.2 System Studied

The ethylene bromonium ion is not a transition state in the bromination reaction, but rather a minimum. In solution, as expected, the transition state is calculated to be an ion pair with bromide having either C_2 or C_{2v} symmetry depending on the solvent[8] (Figure 7-1). In the gas phase, a transition state has been reported[9], but at the RHF/3-21G level, its imaginary frequency does not correspond to Br^- dissociation; reoptimized at the RHF/6-31G(d) level, it is a minimum. Since the transition state in solution comprises the developing ions, the likelihood of finding a gas-phase transition state is small due to the lack of conditions that would facilitate charge separation in this environment.

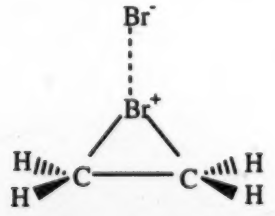

Figure 7-1. Transition State for the Bromination of Ethylene

Rivail and co-workers looked at the first step of ethylene bromination in water in a recent molecular dynamics study using the novel QC/MM MD method[8]. Their results confirm that the reaction has a late transition state, with the ions already formed. According to the Hammond principle[10], one can make the assumption that the transition state resembles the ethylene bromonium ion more than it does the ethylene and bromine reactants, as shown in Figure 7-2. The

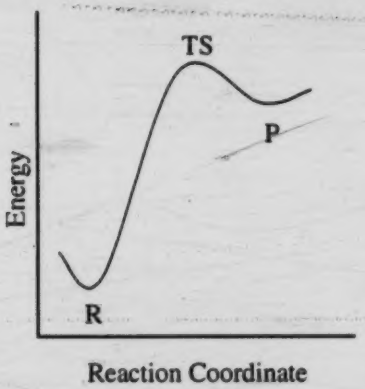

Figure 7-2. Schematic of a Late Transition State (TS ≈ P)

structure of the ethylene bromonium ion can then be used as an adequate representation of the genuine transition state. In the present study, the calculations were done for the equilibrium isotope effect (EIE) for the equilibrium involving the formation of the reaction intermediate $[C_2H_4Br]^+$

$$Br^+ + C_2H_4 \rightleftharpoons H_2C\!-\!\overset{Br^+}{\overset{\wedge}{}}\!-\!CH_2$$

Extending the discussion in Chapters One and Six by taking into consideration tunnelling, for the equilibrium

$$R \rightleftharpoons P$$

the EIE is calculated in the gas phase, rigid rotor, harmonic oscillator approximation according to[10]:

$$\frac{K_H}{K_D} = \frac{\kappa_H}{\kappa_D} \bullet \frac{\sigma_H}{\sigma_D} \bullet \frac{Q^{P_H/R_H}}{Q^{P_D/R_D}} e^{-(\delta E_o^R - \delta E_o^P)/RT} \qquad (7\text{-}1)$$

where κ is the tunnelling transmission coefficient, σ is the symmetry number, δE_o^R is the difference between the total molar vibrational zero-point energies for the light and heavy reactant compounds R_H and R_D, δE_o^P is the difference between the total molar vibrational zero-point energies for the light and heavy product compounds P_H and P_D, and Q is the total molar partition function. The Br^+ contribution to the partition functions cancels in the term $\frac{Q^{P_H/R_H}}{Q^{P_D/R_D}}$ and will not be addressed further.

7.3 Results and Discussion

The structural parameters for ethylene and the ethylene bromonium ion are collected in Table 7-1 and compared with available experimental data. For ethylene, the DFT bond lengths are longer than experimental ones by about 0.02 Å, possibly due to the use of either ECPs and their associated basis sets or the B3LYP combination of functionals. The structure of the ethylene bromonium ion has not been characterized experimentally.

The harmonic vibrational modes calculated for ethylene and ethylene bromonium ion were visualized using MOLDEN[12] and MacMolPlt[13] and the mode assignments were done for both the hydrogenated and deuterated species. Table 7-2 lists the assignment for ethylene comparing the unscaled calculated frequencies to experimental ones[14]. With the exception of the CC stretch, all the modes are underestimated with DFT by an average of ca. 40 cm^{-1}.

Table 7-1. Geometry of Ethylene and the Ethylene Bromonium Ion

Parameter	Ethylene		Ethylene Bromonium Ion
	DFT	Experimental[11] (r_z, θ_z)[a]	DFT
Bond Length (Å)			
C-C	1.364	1.339	1.472
C-H	1.107	1.087	1.104
C-Br			2.062
Angle (°)			
H-C-H	117.4	117.3	108.0
C-C-H	121.3	121.3	119.7
H-C-Br			118.5

[a] r_z (= r_α^0) the distance between the average nuclear positions (ground vibrational state); θ_z is the angle defined by a set of three average nuclear positions (ground vibrational state)

Table 7-2. Assignment of the Harmonic Vibrational Modes of Ethylene

Mode	Symmetry[a]	DFT	Expt.[14]	Assignment
1	b_{2u}	793	843	CH_2 sym rock
2	b_{2g}	900	959	CH_2 sym wag
3	b_{3u}	939	969	CH_2 asym wag
4	a_u	1021	1044	CH_2 asym twist
5	b_{3g}	1167	1245	CH_2 asym rock
6	a_g	1342	1370	CH_2 sym scissors
7	b_{1u}	1413	1473	CH_2 asym scissors
8	a_g	1692	1655	C-C stretch
9	b_{1u}	3122	3147	CH stretch asym (CH_2 sym)
10	a_g	3134	3153	CH stretch sym (CH_2 sym)
11	b_{3g}	3202	3232	CH stretch asym (CH_2 asym)
12	b_{2u}	3229	3234	CH stretch sym (CH_2 asym)

[a] Ethylene is located in the yz plane, with the CC bond along the z axis

For the analysis of the origins of the isotope effects it is convenient to factor equation (7-1); setting the tunnelling transmission coefficient κ to unity, the equation may be written as follows:

$$\frac{K_H}{K_D} = \eta\left(\frac{\sigma_H}{\sigma_D}\right) \qquad (7\text{-}2)$$

where $\sigma_B = \left(\frac{s_B^R}{s_B^P}\right)$, B = H or D, is the ratio of symmetry numbers for products (s^P) and reactants (s^R) and η is the per-site isotope effect. Assuming the separation of rotations and vibrations, the isotope effect η may be factored as[15]

$$\eta = \eta_{trans} \cdot \eta_{rot} \cdot \eta_{vib} \cdot \zeta_{vib} \tag{7-3}$$

where η_X denotes the ratio of the partition functions (X = translational, rotational, or vibrational) for light (H) and heavy (D) products (P) and reactants (R)

$$\eta_X = \frac{Q_X^{P_H} / R_H}{Q_X^{P_D} / R_D} \tag{7-4}$$

and ζ_{vib} represents the effect of the isotopic change on the separation of the zero-point energies:

$$\zeta_{vib} = \exp^{-(\Delta_{ZPE}^P - \Delta_{ZPE}^R)/RT}. \tag{7-5}$$

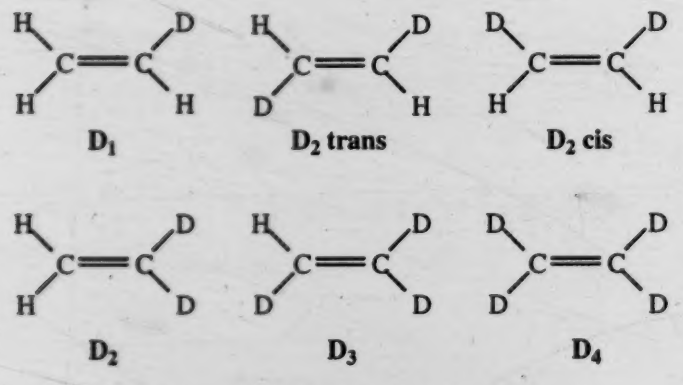

D_1 D_2 trans D_2 cis

D_2 D_3 D_4

Scheme 7-1. Deuterated Ethylenes

Several deuterated ethylenes (Scheme 7-1) and their associated bromine adducts were studied. The contributions of various factors to the overall values of the isotope effects, calculated in the gas phase at 298.15 K and 1 atm, are shown in Table 7-3. The rotational contribution increases by 30% from D_1 to D_4 and, multiplied by the slowly varying translational factor, works toward a normal

isotope effect. The effect of isotopic substitution on the vibrational energy levels appears in two ways: through the ratio of the vibrational partition functions in the vibrational factor η_{vib} and through the change in the zero-point energies, contained in ζ_{vib}. As Table 7-3 shows, η_{vib} contributes almost a unity to the overall effect making ζ_{vib} responsible for the inverse isotope effect η. The overall vibrational contribution, $\eta_{vib} \cdot \zeta_{vib}$, decreases by 50% from D_1 to D_4 and brings about a significant inverse isotope effect. Considering that the harmonic vibrational frequencies were not scaled, the η value for the perdeuterated system D_4, η = 0.630, is nicely bracketed by the experimentally determined values of the kinetic isotope effect k_H/k_D = 0.664 ± 0.05 in methanol and 0.572 ± 0.048 in dichloroethane. Changing the nucleophilicity of the solvent does not affect the kinetic isotope effect in a major way; extending this to the gas-phase limit, the isotope effect again should not change much, thus leading to good agreement between the calculated and experimental values.

Table 7-3. Contributions to the Per-Site Secondary Isotope Effects[a]

System	η_{trans}	η_{rot}	$\eta_{trans}\eta_{rot}$	η_{vib}	ζ_{vib}	$\eta_{vib}\zeta_{vib}$	η	η^{-1}
D_1	1.040	1.111	1.155	0.980	0.784	0.768	0.888	1.126
D_2-trans	1.079	1.206	1.301	0.965	0.631	0.609	0.792	1.263
D_2-cis	1.079	1.223	1.320	0.963	0.622	0.598	0.790	1.266
D_2	1.079	1.232	1.329	0.962	0.617	0.594	0.789	1.267
D_3	1.118	1.328	1.485	0.948	0.500	0.475	0.705	1.418
D_4	1.157	1.435	1.660	0.935	0.406	0.380	0.630	1.587

[a] The contributions η_{trans}, η_{rot}, η_{vib}, and ζ_{vib} to the per-site isotope effect η are defined in equations (7-2) to (7-5)

The ethylene-bromine system is simple enough to allow for a detailed study of the origin of the inverse isotope effects, and such a study was carried out for the D_4 system. Since the modes of all four species involved could be assigned and no vibrations were degenerate, modes could be easily correlated between the species. As Table 7-4 shows, deuteration of ethylene and the ethylene bromonium ion results in only minor changes in the ordering of the vibrational modes.

Both the η_{vib} and ζ_{vib} factors contain multiplicative contributions from each of the vibrational modes listed in Table 7-4; as a result, the vibrational contribution to the overall isotope effect $\eta_{vib} \cdot \zeta_{vib}$ may be easily factored into contributions corresponding to individual vibrational modes:

$$\zeta_{vib} \cdot \eta_{vib} = \prod_{i=1}^{15} \eta_{vib,i} \zeta_{vib,i} \tag{7-6}$$

where the contribution of the *i*th mode to $\zeta_{vib,i}$ may be written as

$$\zeta_{vib,i} = \exp^{-[\Delta\Delta\nu_i]/2RT} \tag{7-7}$$

with $\Delta\Delta\nu_i = \Delta\nu_i(R) - \Delta\nu_i(P)$ denoting the overall change in the zero-point energies (in kJ/mol) due to the mode *i* in the reactant and product. The contributions from the individual vibrational modes are collected in Table 7-5. The effects due to the vibrational partition function ratio are negligible (close to unity) for all modes except the new modes 13-15 created by the addition of bromine to ethylene. For a vibrational mode to contribute significantly to the total isotope effect via ζ_{vib},

Table 7-4. Mapping of Calculated Harmonic Frequencies for Ethylene (D_{2h} symmetry) and the Ethylene Bromonium Ion (C_{2v} symmetry)

Mode	C_2R_4			$C_2R_4Br^+$			Assignment
	symm	R=H	R=D	symm	R=H	R=D	
1	b_{2u}	793	570	b_1	808	573	CH_2 sym rock
2	b_{2g}	900	743	b_2	1063	817	CH_2 sym wag
3	b_{3u}	939	711	a_1	1071	803	CH_2 asym wag
4	a_u	1021	723	a_2	883	630	CH_2 asym twist
5	b_{3g}	1167	950	a_2	1169	929	CH_2 asym rock
6	a_g	1342	971	a_1	1481	1264	CH_2 sym scissors
7	b_{1u}	1413	1047	b_2	1414	1045	CH_2 asym scissors
8	a_g	1692	1580	a_1	1176	945	CC stretch
9	b_{1u}	3122	2243	b_2	3120	2255	CH stretch asym (CH_2 sym)
10	a_g	3134	2321	a_1	3120	2278	CH stretch sym (CH_2 sym)
11	b_{3g}	3202	2389	a_2	3234	2424	CH stretch asym (CH_2 asym)
12	b_{2u}	3229	2405	b_1	3247	2423	CH stretch sym (CH_2 asym)
13				b_2	434	412	CBr asym stretch
14				a_1	450	432	CBr sym stretch
15				b_1	844	619	CH_2 sym twist

Table 7-5. Contributions of Various Modes to ζ_{vib} and η_{vib}

Mode	$\eta_{vib,i}$	$\Delta\nu_i(R)$	$\Delta\nu_i(P)$	$\Delta\Delta\nu_i$	$\zeta_{vib,i}$	$\eta_{vib,i}\cdot\zeta_{vib,i}$
1	1.000	223	234	11	0.973	0.973
2	1.001	157	247	90	0.805	0.806
3	1.007	229	268	39	0.909	0.915
4	0.989	299	254	-44	1.116	1.103
5	0.999	218	240	22	0.948	0.947
6	1.006	371	217	-153	1.449	1.458
7	1.000	365	369	4	0.991	0.991
8	0.993	112	230	118	0.751	0.746
9	1.000	868	865	-2	1.007	1.007
10	1.000	813	842	29	0.933	0.933
11	1.000	813	810	-2	1.008	1.008
12	1.000	824	824	0	0.999	0.999
13	0.984		22	22	0.948	0.933
14	0.988		18	18	0.958	0.947
15	0.966		225	225	0.581	0.561
Total	0.935[a]			373[b]	0.406[c]	0.380[d]

[a] $\prod_{i=1}^{15}\eta_{vib,i}$, [b] $\sum_{i=1}^{15}\Delta\Delta\nu_i$ (in cm^{-1}), [c] $\prod_{i=1}^{15}\zeta_{vib,i}$, [d] $\prod_{i=1}^{15}\eta_{vib,i}\cdot\zeta_{vib,i}$

the change in the harmonic frequency upon isotopic substitution in the reactant and products ought to be different: $\Delta\nu(R) \neq \Delta\nu(P)$. There are two such modes in the ethylene portion of the ethylene bromonium ion system: CH_2 symmetric scissors (mode 6) contributing to a normal isotope effect and the CC stretch (mode 8) contributing to the inverse effect. (There is a significant motion of the substituents on the carbon atoms during the CC stretch.) Despite large isotopic changes in all remaining modes (for example, the CH stretches, modes 9-12), their contribution to the overall isotopic effect is negligible because $\Delta\nu(R) \approx \Delta\nu(P)$. The largest contribution from an individual mode is due to the CH_2 symmetric twist (mode 15 in Tables 7-4 and 7-5; see Figure 7-3), and it adds to the magnitude of the inverse effect. However, Table 7-5 clearly shows that the CH_2 symmetric twist (mode 15), while dominant, is not the only contributor to the effect. Nevertheless, it plays a very important role: when the isotope effect is calculated

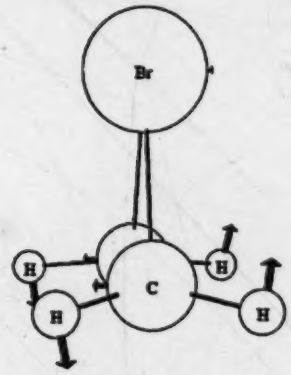

Figure 7-3. Vibrational Mode 15: CH_2 Symmetric Twist

in the absence of mode 15, the inverse effect of $\eta = 0.630$ is replaced by a normal effect of $\eta = 1.12$.

As mentioned in Chapter Six, two models were proposed to explain the origin of the secondary α - isotope effect: the older interpretation suggested by Streitwieser *et al.*[16] and a more recent, alternative explanation by Strausz *et al.*[17]. Bender and co-workers have recently shown that, for equilibrium binding of ethylene to $Os_2(CO)_8$[18] and equilibrium H_2/D_2 binding in the $W(CO)_3(PCy_3)_2(\eta^2\text{-}H_2)$[19] complex, the zero-point energy components associated with the creation of new vibrational modes in the complexes contribute most to the inverse EIEs. In the reversible binding of ethylene to $Os_2(CO)_8$, the EIE calculated from the vibrational modes of the species involved (K_H/K_D=0.7110) agrees well with that observed experimentally (K_H/K_D=0.7(1)). The largest contribution to the inverse effect was found to arise from the b_2-symmetry-twisting mode of the CH_2 groups in diosmacyclobutane, which lacks a vibrational counterpart in ethylene, making its contribution inverse in nature. In the case of bromination of ethylene, there is strong evidence in support of the model put forth by Strausz *et al.*, namely that the inverse isotope effect arises from the creation of the CH_2 symmetric twist mode rather than it being due to a rehybridization of the carbons from sp^2 and sp^3. It

must be added here that there is little rehybridization at the carbon atoms upon the addition of bromine: the sum of the three angles C-C-H, H-C-H, and C-C-H is about 353.7°, very close to the sum of 360°, characteristic of the sp^3 hybrid.

As a representation of the first step toward charge separation in the bromination of ethylene, the charge-transfer complex equilibrium

$$C_2H_4 + Br_2 \rightleftharpoons C_2H_4{:}Br_2$$

was studied and the isotope effects were evaluated. Table 7-6 compares the DFT geometry with the one calculated at the MP2 level[20]. Assignments of the vibrational modes in the CTC are listed in Table 7-7. The absence of imaginary frequencies indicates that the CTC is a minimum on the potential energy surface.

Table 7-6. Bond Lengths (Å) in the CTC

Bond	DFT	MP2[a]
Br-Br	2.389	2.354
Br-C	2.868	3.021
C-C	1.370	1.343

[a] Br(16s11p5d/5s4p2d), C(10s6p1d/4s3p1d), and H(5s1p/2s1p)[20]

A substantial inverse isotope effect of $\eta = 0.89$ is found; however, it is small when compared with the effect found in the bromonium ion. In contrast to the ethylene bromonium ion, there is no single mode responsible for the isotopic effect in the charge-transfer complex.

7.4 Conclusions

The DFT calculations of the EIE for the equilibrium $Br^+ + C_2H_4 \rightleftharpoons [C_2H_4Br]^+$ confirm the validity of Strausz's model[17] where the creation of a new isotopically sensitive mode is responsible for the isotope effect. The ethylene system is small enough to allow for unambiguous identification of vibrational

Table 7-7. Assignment of Harmonic Vibrational Modes for the CTC (cm^{-1})

Mode	Symmetry[a]	DFT	Assignment
1	b_1	74	Br-Br-C_2H_4 def. (front to back)
2	b_2	74	Br-Br-C_2H_4 def. (right to left)
3	a_1	112	Br_2-C_2H_4 stretch
4	b_2	155	C_2H_4 twist or Br-C asym stretch
5	a_1	262	Br-Br stretch
6	b_1	293	CH_2 sym twist
7	b_1	800	CH_2 sym rock
8	b_2	928	CH_2 asym wag
9	a_1	972	CH_2 sym wag
10	a_2	1005	CH_2 asym twist
11	a_2	1180	CH_2 asym rock
12	a_1	1336	CH_2 sym scissors
13	b_2	1420	CH_2 asym scissors
14	a_1	1649	C-C stretch
15	b_2	3132	CH stretch sym (CH_2 asym)
16	a_1	3141	CH stretch sym (CH_2 sym)
17	a_2	3219	CH stretch asym (CH_2 asym)
18	b_1	3245	CH stretch asym (CH_2 sym)

[a] CTC was assumed to have C_{2v} symmetry, with Br_2 aligned along the z-axis and the CC bond parallel to the y axis.

modes in all the species involved leading to the identification of a single mode - CH_2 symmetric twist - that is undoubtedly responsible for the inverse EIE[18,19]. The good agreement between the experimental and calculated isotope effects indicates that DFT is a useful tool for studying the nature of secondary isotope effects which cannot be resolved experimentally.

7.5 References

1. Koerner, T.; Brown, R. S.; Gainsforth, J. L.; Klobukowski, M. *J. Am. Chem. Soc.* **1998**, *120*, 5628.

2. Gaussian 94, Revision D.3, Frisch, M. J.; Trucks, J. W.; Schlegel, H. B.; Gill, P. M. W.; Johnson, B. G.; Robb, M. A.; Cheeseman, J. R.; Keith, T.; Petersson, G. A.; Montgomery, J. A.; Raghavachari, K.; Al-Laham, M. A.; Zakrzewski, V. G.; Ortiz, J. V.; Foresman, J. B.; Cioslowski, J.; Stefanov, B. B.; Nanayakkara, A., Challacombe, M.; Peng, C. Y.; Ayala, P. Y.; Chen, W.; Wong, M. W.; Andres, J. L.; Replogle, E. S.; Gomperts, R.; Martin, R. L.; Fox, D. J.; Binkley, J. S.; Defrees, D. J.; Baker, J.; Stewart, J. P.; Head-Gordon, M.; Gonzalez, C.; and Pople, J. A. Gaussian, Inc., Pittsburgh PA, 1995.

3. Wiest, O.; Black, K. A.; Houk, K. N. *J. Am. Chem. Soc.* **1994**, *116*, 10336.

4. Becke, A. D. *J. Chem. Phys.* **1993**, *98*, 5648.

5. Lee, C.; Yang, W.; Parr, R. G. *Phys. Rev. B* **1988**, *37*, 785.

6. (a) Stevens, W. J.; Basch, H.; Krauss, M. *J. Chem. Phys.* **1984**, *81*, 6026. (b) Stevens, W. J.; Krauss, M.; Basch, H.; Jasien, P. G. *Can. J. Chem.* **1992**, *70*, 612.

7. Huzinaga, S. *J. Chem. Phys.* **1965**, *42*, 1293.

8. Strnad, M.; Martins-Costa, M. T. C.; Millot, C.; Tuñón, I.; Ruiz-López, M. F.; Rivail, J. L. *J. Chem. Phys.* **1997**, *106*, 3643.

9. Yamabe, S.; Minato, T.; Inagaki, S. *J. Chem. Soc., Chem. Commun.* **1988**, 532.

10. Maskill, H. In *The Physical Basis of Organic Chemistry*; Oxford University Press: New York, 1985. See also: van Hook, W. A. In *Isotope Effects in Chemical Reactions*; Collins, C. J., Bowman, N. S., Eds.; Van Norstrand: New York, 1970.

11. Hirota, E.; Endo, Y.; Saito, S.; Yoshida, K; Yamaguchi, I.; Machida, K. *J. Mol. Spectrosc.* **1980**, *89*, 223.

12. Schaftenaar, G. *QCPE Bull.* **1992**, *12*, 3 (available from http://www.caos.kun.nl/~schaft/molden).

13. MacMolPlt is available from http://www.msg.ameslab.gov/GAMESS/Graphics/MacMolPlt.html.

14. Duncan, D. L.; McKean, D. C.; Makkison, P. D. *J. Mol. Spectrosc.* **1973**, *45*, 221.

15. (a) Lu, D.-h.; Maurice, D.; Truhlar, D. G. *J. Am. Chem. Soc.* **1990**, *112*, 6206. (b) Zhao, X. G.; Tucker, S. C.; Truhlar, D. G. *J. Am. Chem. Soc.* **1991**, *113*, 826.

16. Streitweiser, A., Jr.; Jagow, R. H.; Fahey, R. C.; Suzuki, S. *J. Am. Chem. Soc.* **1958**, *80*, 2326.

17. (a) Strausz, O. P.; Safarik, I.; O'Callaghan, W. B.; Gunning, H. E. *J. Am. Chem. Soc.* **1972**, *94*, 1828. (b) Safarik, I.; Strausz, O. P. *J. Phys. Chem.* **1972**, *76*, 3613.

18. Bender, R. B. *J. Am. Chem. Soc.* **1995**, *117*, 11239.

19. Bender, R. B.; Kubas, G. J.; Jones, L. H.; Swanson, J. E.; Capps, K. B.; Hoff, C. D. *J. Am. Chem. Soc.* **1997**, *119*, 9179.

20. Assfeld, X.; Garapon, J.; Rinaldi, D.; Ruiz-López, M. F.; Rivail, J.-L. *Theochem* **1996**, *371*, 107.

Chapter Eight

Isotope Effects in the Addition of Sulfur and Selenium to Ethylene

8.1 Introduction

α - secondary isotope effects are the more easily understood of the secondary isotope effects with models being developed to help understand and predict these effects. The one model that is predominantly cited in organic chemistry textbooks[1,2,3] to describe the origin for the α - effects was proposed by Streitwieser[4]. This model states that when the hybridization of the carbon changes (i.e., $sp^2 \rightarrow sp^3$) as the reaction proceeds, the C-H and C-D bending modes are affected and result in the observed isotope effect. It is also believed that β - effects arise from changes in these same bending modes due to hyperconjugation[4]. Another, but less commonly cited, model was developed by Strausz[5] who postulated that the isotope effect is a result of the ZPE contributions from new, isotopically sensitive modes in the transition state. These modes are created from rotational degrees of freedom in the reactants being converted into internal degrees of freedom in the transition state.

Strausz developed this model a quarter of a century ago during the gas phase study of the kinetic isotope effects for the addition of sulfur to ethylene[5]. Using the Bigeleisen equation (shown in its abbreviated form)[6]

$$KIE = k_H/k_D = MMI \cdot EXC \cdot ZPE \qquad (8\text{-}1)$$

and two models for the transition state, intense quantum-chemical calculations were used to get individual mode contributions from vibrational frequencies and force constants. A single new, isotopically sensitive mode responsible for the effect led to the conclusion that the Streitwieser model was not valid for ethylene addition reactions.

The original calculations on C_2H_4 + S, done 25 years ago, were very limited due to a lack of software and hardware that is now available, prompting a reinvestigation into the sulfur addition using modern techniques. The similarity of the contributions to the KIE with those seen in the bromination of ethylene was encouraging, but a lack of knowledge about the transition state structure and its associated vibrational frequencies in the earlier work was a major limitation. Since both the symmetric and asymmetric transition state models could be fit to the experimental data, it could not be determined which model was favored on the basis of the study. Today, both transition states can be optimized (and vibrational frequencies calculated) with the lower energy structure being chosen; this removes some of the ambiguity present in the earlier work. Since vibrational frequencies are available for both the reactants and the transition state, individual mode contributions to the KIE can be looked at in more detail. Extending the study down the chalcogen series, the KIEs for the addition of selenium to ethylene are also calculated.

8.2 Computational Details

The KIEs for the addition of S and Se to ethylene were modeled using results obtained with DFT contained within the Gaussian 94[7] program. For sulfur, Becke's exchange (B)[8] and Becke's 3-parameter exchange (B3)[9] were combined with the correlation functionals of Lee, Yang, and Parr (LYP)[10] and Perdew and Wang (PW91)[11] to give 3 combinations: BLYP, B3LYP, and B3PW91. Only the B3PW91 combination was used with the selenium system.

The extended basis set 6-311++G(3df,2p) (Basis 1) was used for the all-electron calculations in the sulfur system. A mixed all-electron/ECP basis (Basis 2) was built for the study of the chalcogen series. Carbon and hydrogen were described with the 6-311++G(3d,2p) basis. The f polarization function in Basis 1 was omitted because Gaussian 94 does not allow f polarization functions in ECP

calculations. For sulfur and selenium, the effective core potential of Stevens *et al.*[12] was used with modified basis sets: the original basis set was completely uncontracted and two d polarization functions[13] were added.

The calculations were done for the kinetic isotope effect for the reaction

$$C_2H_4 + L \rightarrow C_2H_4\text{-}L \quad L = S, Se \tag{8-2}$$

which proceeds through an asymmetric transition state.

The KIE is calculated in the gas phase, rigid rotor, harmonic oscillator approximation according to equation (7-1), written here again for convenience[14]:

$$\frac{k_H}{k_D} = \frac{\kappa_H}{\kappa_D} \bullet \frac{\sigma_H}{\sigma_D} \bullet \frac{Q^{A_H / R_H}}{Q^{A_D / R_D}} e^{-(\delta E_O^A - \delta E_O^R)/RT} \tag{8-3}$$

where: κ is the tunnelling transmission coefficient, σ is the symmetry number, δE_O^R is the difference between the total molar vibrational zero-point energies for the light and heavy reactant compounds R_H and R_D, δE_O^A is the difference between the molar vibrational zero-point energies for the light and heavy transition states A_H and A_D, and Q is the total molar partition function. As was the case with the bromination reactions, Chapters Six and Seven, the contributions to the partition coefficient from S and Se are cancelled out in the term $\frac{Q^{A_H / R_H}}{Q^{A_D / R_D}}$ and will not be addressed further.

8.3 Results and Discussion

The structural parameters for ethylene, thiirane, and selenirane are collected in Tables 8-1 and 8-2 and compared with available experimental data. The selenium analogue has not been experimentally characterized. For ethylene, the DFT bond lengths are shorter than experimental ones with the average deviation being 0.012 Å for the C-C bond and 0.003 Å for the C-H bond which is longer

than experiment. The BLYP geometry agrees with prior studies of DFT performance on ethylene[18] when the basis set size is taken into account (i.e., shorter bond lengths with larger basis sets). This functional gives the longest bond lengths which is expected since it lacks the HF component to the exchange that is included in B3. Switching from the LYP correlation functional to PW91 does not change the parameters any more than adding the f polarization function to carbon (Basis 1 versus Basis 2). Overall, the B3 combinations produce very similar geometries and only the B3PW91 results with both basis sets will be shown. All other results will be discussed where important and are available in the Appendix.

Table 8-1. Ethylene Geometry

Parameter	Expt. #1[15]	BLYP Basis 1	B3LYP Basis 1	B3PW91 Basis 1	B3PW91 Basis 2
Bond Length (Å)					
C-C	1.339	1.334	1.325	1.324	1.326
C-H	1.087	1.089	1.083	1.084	1.084
Angle (°)					
C-C-H	121.3	121.8	121.7	121.7	121.7
H-C-H	117.3	116.3	116.5	116.5	116.6

The structure calculated for thiirane is compared to experiment (Table 8-2) as a basis for the description of sulfur in this study rather than looking at the triplet ground state structure which is not known experimentally. The C-C bonds are shorter by about 0.012Å while the C-S bonds are longer by the same amount. While there is overall good agreement between the B3 combinations, the B3PW91/Basis 1 C-S bond length is at least 0.01Å shorter than the others, making it shorter than experiment.

The geometry of the transition state is of C_s symmetry and is shown in Table 8-3. For sulfur, changing the electron correlation functional from LYP to PW91 has a larger effect on the geometry than going from B to B3, which is not

the case for ethylene and thiirane. This indicates that electron correlation is very important to the description of the transition state, most likely due to its weakly bound nature. As is expected, for sulfur and selenium the C-L bond is longer and the C-C-L angle has opened to give an asymmetric geometry (L = S, Se).

Table 8-2. Thiirane and Selenirane Geometry

Parameter	Thiirane (L=S)				Selenirane (L=Se)
	Expt. #1[16]	Expt. #2[17]	B3PW91 Basis 1	B3PW91 Basis 2	B3PW91 Basis 2
Bond Lengths (Å)					
C-C	1.492	1.484	1.478	1.477	1.466
C-L	1.820	1.815	1.809	1.826	1.977
C-H	1.078	1.083	1.083	1.082	1.081
Angles (°)					
L-C-H	114.9	---	115.3	115.0	113.5
C-C-H	117.8	---	118.2	118.2	118.5
C-L-C	---	48.3	48.2	47.7	43.5
C-C-L	---	65.9	65.9	66.1	68.2

Table 8-3. Calculated Transition State Geometry

Parameter	L=Sulfur		L=Selenium
	B3PW91 Basis 1	B3PW91 Basis 2	B3PW91 Basis 2
Bond Length (Å)			
C-L	2.492	2.469	2.402
C-C	1.350	1.354	1.373
C-H	1.083 1.083	1.082 1.082	1.083 1.082
Angle (°)			
C-C-L	97.0	97.8	102.5
C-C-H	121.4 121.4	121.3 121.4	120.3 121.2

The harmonic vibrational modes calculated for both species were visualized using MOLDEN[19] with mode assignments being done for both the hydrogenated and perdeuterated species. Table 8-4 lists the assignment for ethylene comparing the unscaled calculated frequencies to experiment. The BLYP frequencies are consistently smaller than the B3 combinations and experiment. The B3 combinations overestimate and fall short of experiment but lack an obvious pattern. Therefore, there is no uniform scaling factor that would give good agreement with experiment.

Table 8-4. IR Frequencies (in cm^{-1}) of Ethylene

Assignment	B3PW91 Basis 1	B3PW91 Basis 2	EXPT.[20.a]
CH_2 sym rock	827	827	843
CH_2 sym wag	976	972	959
CH_2 asym wag	982	974	969
CH_2 asym twist	1063	1062	1044
CH_2 asym rock	1237	1236	1245
CH_2 sym scissors	1378	1376	1370
CH_2 asym scissors	1466	1468	1473
CC stretch	1692	1690	1655
CH stretch sym (CH_2 asym)	3129	3129	3147
CH stretch all sym	3145	3145	3153
CH stretch all asym	3204	3205	3232
CH stretch asym (CH_2 sym.)	3232	3233	3234

[a] harmonic vibrational frequencies

The harmonic vibrational frequencies of thiirane, unlike those of ethylene, are overestimated by the B3 combinations (Table 8-5) and could be scaled uniformly to agree with experiment. The qualitative assignment given for the experimental bands[21] agrees with the calculated vibrational modes.

Table 8-5. IR Frequencies (in cm^{-1}) of Thiirane and Selenirane

Assignment	Thiirane (L = S)		Selenirane (L = Se)	
	EXPT.[21a]	B3PW91 Basis 1	B3PW91 Basis 2	B3PW91 Basis 2
CL sym stretch	627.3	653.3	647.1	505.2
CL asym stretch		699.5	682.6	586.5
CH_2 sym rock	824.3	834.1	835.0	831.8
CH_2 asym twist		899.9	897.2	846.5
CH_2 sym twist	945.2	959.7	955.9	876.7
CH_2 sym wag	1024.0	1041.9	1041.3	1013.0
CH_2 asym wag	1050.8	1074.8	1068.4	1028.4
CC stretch	1109.9	1150.8	1151.2	1134.9
CH_2 asym rock		1188.5	1192.4	1201.9
CH_2 asym scissors	1435.9	1464.2	1466.8	1459.1
CH_2 sym scissors	1456.8	1488.6	1493.6	1491.5
CH stretch sym (CH_2 asym)	3013.0	3122.1	3128.2	3140.8
CH stretch all sym	3013.5	3123.6	3130.2	3143.5
CH stretch all asym		3203.4	3211.3	3226.3
CH stretch asym (CH_2 sym)	3088.0	3217.9	3225.9	3243.1

[a] anharmonic vibrational frequencies

As indicated in Chapters Six and Seven, for the analysis of the origins of the isotope effects it is convenient to factor equation (8-3). Setting the tunnelling transmission coefficient κ equal to unity, equation (8-3) may be written as follows:

$$k_H/k_D = \eta(\sigma_H/\sigma_D) \qquad (8\text{-}4)$$

where $\sigma_B = (s^R_B/s^A_B)$, B=H or D, is the ratio of the symmetry numbers for reactants (s^R) and transition states (s^A), and η is the per-site isotope effect. Assuming the separation of rotations and vibrations, the isotope effect η may be factored as:[22]

$$\eta = \eta_{trans} \cdot \eta_{rot} \cdot \eta_{vib} \cdot \zeta_{vib} \qquad (8\text{-}5)$$

where η_X denotes the ratio of the partition functions (X= translational, rotational, or vibrational) for light (H) and deuterated (D) reactants (R) and transition states (A):

$$\eta_X = \frac{Q_X^{A_H} / R_H}{Q_X^{A_D} / R_D} \tag{8-6}$$

and ζ_{vib} represents the effect of the isotopic change on the separation of the zero-point energies:

$$\zeta_{vib} = \exp^{-(\Delta^A_{ZPE} - \Delta^B_{ZPE})/RT}. \tag{8-7}$$

The contribution from the single imaginary frequency at the transition state is ignored.

The contributions of various factors to the overall value of the isotope effect, calculated at 298.15 K and 1 atm in the gas phase, are shown in Table 8-6. For the sulfur system, as the functional/basis is changed, the factors change very little (η_{trans} doesn't change), but, as η_{rot} increases, both η_{vib} and ζ_{vib} decrease. The rotational and translational factors contribute towards a large normal isotope effect with η_{rot} being 30% larger than η_{trans}. The effect of isotopic substitution on the vibrational energy levels appears in two ways: through the ratio of the vibrational partition functions in the vibrational factor η_{vib} and through the change in the zero-point energies contained in ζ_{vib}. Both factors have similar contributions, making them almost equally responsible (ζ_{vib} more than η_{vib}) for the observed inverse effect. The total vibrational contribution just cancels out the rotational and translational's large normal effect to give a small inverse effect.

Table 8-6. Contributions to the Per-Site Isotope Effect

Functional	η_{trans}	η_{rot}	$\eta_{trans} \cdot \eta_{rot}$	η_{vib}	ζ_{vib}	$\eta_{vib} \cdot \zeta_{vib}$	η	η^{-1}
Sulfur								
BLYP/Basis 1	1.1095	1.4728	1.6341	.7984	.7633	.6094	.9958	1.0042
B3LYP/Basis 1	1.1095	1.4720	1.6331	.8027	.7615	.6112	.9982	1.0018
B3PW91/Basis 1	1.1095	1.4825	1.6448	.7960	.7510	.5978	.9832	1.0171
B3PW91/Basis 2	1.1095	1.4806	1.6427	.7977	.7486	.5971	.9809	1.0195
Selenium								
B3PW91/Basis 2	1.1576	1.4469	1.6749	.7969	.7567	.6030	1.0100	.9901

The contributions to the KIE in the addition of selenium to ethylene, see Table 8-6, are very similar to sulfur's. The η_{trans} factor is larger, reflecting the difference in the mass of the system (Se > S) and η_{rot} decreases by a smaller amount to give a larger product $\eta_{trans} \cdot \eta_{rot}$. Since the vibrational factors are the same for both heteroatoms, a slight normal isotope effect arises.

The calculated KIEs for sulfur addition are smaller than that observed experimentally ($k_D/k_H = 1.14$)[5] but do predict the effect to be inverse. Uniform scaling of the calculated frequencies by 1.10 (BLYP), 1.11 (B3LYP), 1.07 (B3LYP, B3PW91) and recalculation of the KIE reproduces the experimental ratio, but this is not at all appropriate. Studies done for scaling factors on DFT frequency calculations[23] show that the scaling factor should be less than 1 (0.95-0.99), which would make the calculated inverse KIE even smaller. The change in the imaginary frequency of the transition state upon deuteration is small (about 5 cm^{-1} for B3PW91/Basis 1) making the Wigner tunneling correction negligible. (See reference 24 for discussion of the tunneling corrections). It must be noted here that the present study is semi-quantitative, focused more on the origin of the inverse KIE and the behaviour of DFT for these systems. To get the best agreement with experiment, it is suggested that direct dynamic calculations be done where distinct hypersurfaces for the light and heavy species are considered[24].

The vibrations associated with the addition of a chalcogen to ethylene are simple enough to be assigned and mapped between the species. This allows for an in-depth study of the origin of the isotope effect, which was done for each functional. Tables 8-7 and 8-8 list the mapping for the B3PW91 calculations. In all cases, the ordering of the modes does not change much upon deuteration, addition of the heteroatom or changing the heteroatom. In fact, there are more changes between the functionals for sulfur than there is between sulfur and selenium.

Table 8-7. Mode Mapping for Sulfur Addition to Ethylene (B3PW91/Basis 1 Calculation)

Mode	C_2R_4			C_2R_4S			Assignment
	symm	R=H[a]	R=D	symm	R=H[b]	R=D	
1	b_{2u}	827	594	a"	816	587	CH_2 sym rock
2	b_{3u}	976	738	a'	966	716	CH_2 sym wag
3	b_{2g}	982	813	a'	927	749	CH_2 asym wag
4	a_u	1063	752	a"	990	701	CH_2 asym twist
5	b_{3g}	1237	1008	a"	1228	997	CH_2 asym rock
6	a_g	1378	998	a'	1325	986	CH_2 sym scissors
7	b_{1u}	1466	1086	a'	1462	1083	CH_2 asym scissors
8	a_g	1692	1578	a'	1595	1458	CC stretch
9	b_{1u}	3129	2260	a'	3145	2272	CH stretch sym (CH_2 asym)
10	a_g	3145	2331	a'	3154	2318	CH stretch all sym
11	b_{3g}	3204	2388	a"	3220	2400	CH stretch all asym
12	b_{2u}	3232	2406	a"	3251	2420	CH stretch asym (CH_2 sym)
13				a'	161	146	CCS bend
14				a"	335	243	CH_2 sym twist
15				a'	140*i*	135*i*	CS stretch

[a] BLYP: modes 2 and 3 are swapped

[b] B3LYP: modes 2 and 4 are swapped

Table 8-8. Mode Mapping for Selenium Addition to Ethylene (B3PW91/Basis 2 Calculation)

Mode	C_2R_4			C_2R_4Se			Assignment
	symm	R=H	R=D	symm	R=H	R=D	
1	b_{2u}	827	594	a"	796	573	CH_2 sym rock
2	b_{3u}	972	735	a'	943	681	CH_2 sym wag
3	b_{2g}	974	806	a'	851	693	CH_2 asym wag
4	a_u	1062	751	a"	953	678	CH_2 asym twist
5	b_{3g}	1236	1007	a"	1226	989	CH_2 asym rock
6	a_g	1376	998	a'	1260	969	CH_2 sym scissors
7	b_{1u}	1468	1087	a'	1459	1081	CH_2 asym scissors
8	a_g	1690	1574	a'	1550	1370	CC stretch
9	b_{1u}	3129	2260	a'	3141	2271	CH stretch sym (CH_2 asym)
10	a_g	3145	2329	a'	3153	2305	CH stretch all sym
11	b_{3g}	3205	2389	a"	3211	2390	CH stretch all asym
12	b_{2u}	3233	2407	a"	3253	2423	CH stretch asym (CH_2 sym)
13				a'	190	172	CCSe bend
14				a'	378	274	CH_2 sym twist
15				a'	216*i*	212*i*	CSe stretch

Both the η_{vib} and ζ_{vib} factors contain multiplicative contributions from each of the vibrational modes listed in Tables 8-7 and 8-8; as a result, the vibrational contribution to the overall isotope effect $\zeta_{vib} \cdot \eta_{vib}$ may be easily factored into contributions corresponding to individual vibrational modes:

$$\zeta_{vib} \cdot \eta_{vib} = \prod_{i=1,14} \eta_{vib,i} \cdot \zeta_{vib,i} \qquad (8\text{-}8)$$

where contributions of the *i*-th mode to $\zeta_{vib,i}$ may be written as:

$$\zeta_{vib,i} = \exp \{ - [\Delta\Delta\nu_i]/2RT \} \qquad (8\text{-}9)$$

with $\Delta\Delta\nu_i = \Delta\nu_i(R) - \Delta\nu_i(A)$ denoting the overall change in the zero-point energies (in kJ/mol) due to the mode *i* in the reactant and product. The contributions from the individual vibrational modes are collected in Tables 8-9 and 8-10. For $\eta_{vib,i}$, $\zeta_{vib,i}$, and $\eta_{vib,i} \cdot \zeta_{vib,i}$ the product of each mode contribution is shown for the total while the $\Delta\Delta\nu_i$'s are summed The imaginary frequency associated with the transition state does not contribute to the isotope effect and is not included in the individual mode breakdown (i.e., 14 modes instead of 15). The effects of the

Table 8-9. Individual Mode Contributions for Sulfur Addition to Ethylene (B3PW91/Basis 1)

Mode	$\eta_{vib,i}$	$\Delta\nu_i(R)$[a]	$\Delta\nu_i(A)$[a]	$\Delta\Delta\nu_i$[a]	$\zeta_{vib,i}$	$\eta_{vib,i} \cdot \zeta_{vib,i}$
1	.999	233	229	3	1.008	1.007
2	.997	238	249	11	.9731	.970
3	.995	170	178	8	.9800	.975
4	.995	311	289	-23	1.056	1.051
5	1.000	228	231	2	.994	.994
6	1.000	380	339	-41	1.104	1.104
7	1.000	380	379	-1	1.002	1.002
8	1.000	114	137	23	.946	.946
9	1.000	869	873	4	.990	.990
10	1.000	815	836	21	.951	.951
11	1.000	816	820	5	.989	.989
12	1.000	826	830	4	.990	.990
13	.938		14	14	.966	.906
14	.861		93	93	.800	.688
Total	.796			119	.751	.598

[a] in cm^{-1}. For conversion to kJ/mol, use $\Delta\Delta\nu_i \cdot h \cdot c \cdot N_A$.

vibrational partition function ratio are all close to unity except for the two new modes (imaginary frequency ignored) resulting from the addition of the chalcogen. To see a significant contribution to the overall isotope effect from an individual vibrational mode, the frequency change upon isotopic substitution should be different for the reactants compared to the transition state, $\Delta\nu(R) \neq \Delta\nu(A)$.

Table 8-10. Individual Mode Contributions for Selenium Addition to Ethylene (B3PW91/Basis 2)

Mode	$\eta_{vib,i}$	$\Delta\nu_i(R)^a$	$\Delta\nu_i(A)^a$	$\Delta\Delta\nu_i^a$	$\zeta_{vib,i}$	$\eta_{vib,i}*\zeta_{vib,i}$
1	.996	233	223	-10	1.024	.020
2	.992	237	262	25	.940	.933
3	.992	169	157	-11	1.028	1.020
4	.993	311	275	-35	1.089	1.081
5	.999	229	237	8	.980	.979
6	1.000	378	291	-87	1.233	1.233
7	1.000	380	379	-2	1.004	1.004
8	1.000	115	179	64	.857	.856
9	1.000	869	869	0	1.000	1.000
10	1.000	816	847	31	.927	.927
11	1.000	816	821	5	.988	.988
12	1.000	826	830	4	.991	.991
13	.937		19	19	.856	.895
14	.875		104	104	.779	.681
Total	.797			116	.757	.603

[a] in cm^{-1}

In the sulfur addition reaction, there is a significant contribution from mode 6 (CH_2 symmetric scissors) as well as mode 8 (CC stretch) for some of the functionals. The CH_2 symmetric scissors provides the largest contribution to a normal isotope effect which is almost cancelled out by the inverse contribution from the CC stretch. The remaining modes belonging to the ethylene fragment have small contributions but are not significant to the overall isotope effect. The CH_2 symmetric twist (mode 14) has the largest contribution which leads to an inverse isotope effect. While it is not the only mode adding to the inverse,

calculating the KIE without mode 14 results in a large normal effect of k_H/k_D = 1.43, showing the importance of the CH_2 symmetric twist in the overall effect.

The case for selenium addition (Table 8-10) is analogous to sulfur. Once again the CH_2 symmetric twist (mode 6) and CC stretch (mode 8) have significant competing contributions and are overshadowed by the large contribution from the CH_2 symmetric twist. The remaining new mode (CCS bend - mode 13) also has a reasonable contribution to the inverse effect which is not seen in the case of sulfur. Removing the contribution from the CH_2 symmetric twist mode increases the normal effect to k_H/k_D = 1.48.

For the addition of chalcogens to ethylene, the calculations show that the new mode (CH_2 symmetric twist) created upon addition is responsible for the effect. As was the case with the bromination of ethylene, the carbons experience little rehybridization at the transition state rendering the Streitwieser model invalid for these systems. In the transition state, the sum of the angles around carbon is 357-359° for sulfur and 355° for selenium, which is very close to the sp^2 value of 360°.

8.4 Conclusions

The new CH_2 symmetric twist mode is responsible for the inverse KIE observed for the addition of sulfur to ethylene, reproducing Strausz's results of 25 years ago which used less-sophisticated techniques. While the KIE calculated (k_D/k_H = 1.02) underestimates experiment (k_D/k_H = 1.14) it is close to Strausz's value of k_D/k_H = 1.04. Better agreement could be realized using direct dynamic calculations but it was not a concern for this study.

As the chalcogen series is descended (sulfur to selenium), there are very small changes in geometry, frequencies, and individual mode contributions to the

isotope effect for the addition to ethylene. The selenium KIE is calculated to be normal ($k_D/k_H = 0.99$) but in light of how low the values calculated for sulfur are, it is expected that the experimental KIE would be inverse and smaller than that for the sulfur addition.

Out of the DFT functional combinations used, the B3 combinations gave overall better agreement than the BLYP combination. Of the B3 combinations, B3PW91 was chosen primarily because the three parameters in the Becke-3 exchange functional were optimized with the PW91 correlation functional. The ECP used for sulfur produced results comparable to the all-electron basis giving confidence to the results for the selenium system.

While DFT may not be able to reproduce experiment when the observed isotope effect is small (close to unity), the semi-quantitative and qualitative information that is available from this method is very useful for the understanding of the origins of isotope effects that cannot be resolved by experiment alone.

8.5 References

1. Lowry, T. H.; Richardson, K. S. *Mechanism and Theory in Organic Chemistry, 3rd ed.*; Harper and Row: New York, 1987; p 232-241.

2. Carroll, F. A. *Perspectives on Structure and Mechanism in Organic Chemistry*; Brooks/Cole: Pacific Grove, CA, 1998; p 349-365.

3. March, J. *Advanced Organic Chemistry : Reactions, Mechanisms, and Structure, 4th ed.*; John Wiley & Sons: New York, 1992; p 226-230.

4. Streitwieser, A.; Jagow, R. H.; Fehey, R. C.; Suzuki, S. *J. Am. Chem. Soc.* **1958**, *80*, 2326.

5. Strausz, O. P.; Safarik, I.; O'Callaghan, W. B.; Gunning, H. E. . *J. Am. Chem. Soc.* **1972**, *94*, 1828.

6. Bigeleisen, J.; Goeppert Mayer, M. *J. Chem. Phys.* **1947**, *15*, 261. A nice overview of Bigeleisen's contribution to isotope effects is given in the December 22, 1997 issue of *Chemical and Engineering News*, p 38.

7. Gaussian 94, Revision D.3, Frisch, M. J.; Trucks, J. W.; Schlegel, H. B.; Gill, P. M. W.; Johnson, B. G.; Robb, M. A.; Cheeseman, J. R.; Keith, T.; Petersson, G. A.; Montgomery, J. A.; Raghavachari, K.; Al-Laham, M. A.; Zakrzewski, V. G.; Ortiz, J. V.; Foresman, J. B.; Cioslowski, J.; Stefanov, B. B.; Nanayakkara, A., Challacombe, M.; Peng, C. Y.; Ayala, P. Y.; Chen, W.; Wong, M. W.; Andres, J. L.; Replogle, E. S.; Gomperts, R.; Martin, R. L.; Fox, D. J.; Binkley, J. S.; Defrees, D. J.; Baker, J.; Stewart, J. P.; Head-Gordon, M.; Gonzalez, C.; and Pople, J. A. Gaussian, Inc., Pittsburgh PA, 1995.

8. Becke, A. D. *Phys. Rev. A* **1988**, *38*, 3098.

9. Becke, A. D. *J. Chem. Phys.***1993**, *98*, 5648.

10. Lee, C.; Yang, W.; Parr, R. G. *Phys. Rev. B* **1988**, *37*, 785.

11. Perdew, J. P.; Wang, Y. *Phys. Rev. B* **1992**, *45* , 13244.

12. (a) Stevens, W. J.; Basch, H.; Krauss, M. *J. Chem. Phys.* **1984**, *81*, 6026. (b) Stevens, W. J.; Krauss, M.; Basch, H.; Jasien, P. G. *Can. J. Chem.* **1992**, *70*, 612.

13. Andzelm, J.; Klobukowski, M.; Radzio-Andzelm, E.; Sakai, Y.; Huzinaga, S. (Ed.); Tatewaki, H. *Gaussian Basis set for Molecular Calculations*; Elsevier: Amsterdam, 1984.

14. Maskill, H. In *The Physical Basis of Organic Chemistry*; Oxford University Press: New York, 1995. See also: van Hook, W. A. In *Isotope Effects in Chemical Reactions*; Collins, C. J., Bowman, N. S., Eds.; Van Norstrand: New York, 1970.

15. Hirota, E.; Endo, Y.; Saito, S.; Yoshida, K.; Yamaguchi, I.; Machida, K. *J. Mol. Spectrosc.* **1981**, *89*, 223.

16. (a) Cunningham, G. L., Jr.; Boyd, A. W.; Myers, R. J.; Gwinn, W. D.; Le Van, W. I. *J. Chem. Phys.* **1951**, *19*, 676. (b) Okiye, K.; Hirose, C.; Lister, D. G.; Sheridan, J. *Chem. Phys. Lett.* **1974**, *24*, 111.

17. *CRC Handbook of Chemistry and Physics, 75th ed.*; Lide, D. R., Ed.; CRC Press: Boca Raton, 1994; p 9-31.

18. (a) Oliphant, N.; Bartlett, R. J. *J. Chem. Phys.* **1994**, *100*, 6550. (b) Johnson, B. G.; Gill, P. M. V.; Pople, J. A. *J. Chem. Phys.* **1993**, *98*, 5612. (c) Baker, J.; Muir, M.; Andzelm, J. *J. Chem. Phys.* **1995**, *102*, 2063. (d) Handy, N. C. In *Lecture Notes in Quantum Chemistry II*, Roos, B. O., Ed.; Springer-Verlag: Berlin, 1994.

19. Schaftenaar, G. *QCPE Bulletin* **1992**, *12*, 3 (available from http://www.caos.kun.nl/~schaft/molden).

20. Duncan, D. L.; McKean, D. C.; Makkison, P. D. *J. Mol. Spectrosc.* **1973**, *45*, 221.

21. Allen, W. D.; Bertie, J. E.; Falk, M. V.; Hess, B. A., Jr.; Mast, G. B.; Othen, D. A.; Schaad, L. J.; Schaefer, H. F., III *J. Chem. Phys.* **1986**, *84*, 4211.

22. (a) Lu, D-h.; Maurice, D.; Truhlar, D. G. *J. Am. Chem. Soc.* **1990**, *112*, 6206. (b) Zhao, X. G.; Tucker, S. C.; Truhlar, D. G. *J. Am. Chem. Soc.* **1991**, *113*, 826.

23. (a) Scott, A. P.; Radom, L. *J. Phys. Chem.* **1996**, *100*, 16502. (b) Wong, M. W. *Chem Phys. Lett.* **1996**, *256*, 391.

24. Lu, D-h.; Maurice, D.; Truhlar, D. G. *J. Am. Chem. Soc.* **1990**, *112*, 6206.

8.6 Appendix: Complete Basis Set Results

Table 8-A1. Thiirane Geometry

Parameter	Expt. #1[20]	Expt. #2[21]	BLYP Basis 1	B3LYP Basis 1	B3PW91 Basis 1	B3PW91 Basis 2
Bond Length (Å)						
C-C	1.492	1.484	1.487	1.479	1.478	1.477
C-S	1.820	1.815	1.847	1.823	1.809	1.826
C-H	1.078	1.083	1.088	1.082	1.083	1.082
Angle (°)						
S-C-H	114.9	---	114.9	115.2	115.3	115.0
C-C-H	117.8	---	118.4	118.3	118.2	118.2
C-S-C	---	48.3	47.5	47.8	48.2	47.7
C-C-S	---	65.9	66.3	66.1	65.9	66.1

Table 8-A2. Sulfur Transition State Geometry

Parameter	BLYP Basis 1	B3LYP Basis 1	B3PW91 Basis 1	B3PW91 Basis 2
Bond Length (Å)				
C-S	2.379	2.359	2.492	2.469
C-C	1.376	1.366	1.350	1.354
C-H	1.088 1.087	1.081 1.081	1.083 1.083	1.082 1.082
Angle (°)				
C-C-S	101.2	101.7	97.0	97.8
C-C-H	120.8 121.4	120.7 121.3	121.4 121.4	121.3 121.4

Table 8-A3. IR Frequencies (in cm^{-1}) of Ethylene

Assignment	BLYP B4	B3LYP B4	B3PW91 B4	B3PW91 B7	EXPT.[20]
CH_2 sym rock	818	837	827	827	843
CH_2 sym wag	945	979	976	972	959
CH_2 asym wag	942	987	982	974	969
CH_2 asym twist	1034	1063	1063	1062	1044
CH_2 asym rock	1215	1246	1237	1236	1245
CH_2 sym scissors	1348	1381	1378	1376	1370
CH_2 asym scissors	1445	1480	1466	1468	1473
CC stretch	1635	1689	1692	1690	1655
CH stretch sym (CH_2 asym)	3047	3128	3129	3129	3147
CH stretch all sym	3060	3141	3145	3145	3153
CH stretch all asym	3111	3196	3204	3205	3232
CH stretch asym (CH_2 sym.)	3141	3224	3232	3233	3234

Table 8-A4. IR Frequencies (in cm^{-1}) of Thiirane

Assignment	BLYP Basis 1	B3LYP Basis 1	B3PW91 Basis 1	B3PW91 Basis 2	EXPT.[25]
CS sym stretch	588.0	624.4	653.3	647.1	627.3
CS asym stretch	619.5	667.6	699.5	682.6	
CH_2 sym rock	817.2	838.3	834.1	835.0	824.3
CH_2 asym twist	871.9	900.6	899.9	897.2	
CH_2 sym twist	923.5	957.3	959.7	955.9	945.2
CH_2 sym wag	1013.1	1046.0	1041.9	1041.3	1024.0
CH_2 asym wag	1039.4	1080.6	1074.8	1068.4	1050.8
CC stretch	1100.2	1139.3	1150.8	1151.2	1109.9
CH_2 asym rock	1165.3	1197.2	1188.5	1192.4	
CH_2 asym scissors	1439.4	1475.7	1464.2	1466.8	1435.9
CH_2 sym scissors	1456.6	1497.5	1488.6	1493.6	1456.8
CH stretch sym (CH_2 asym)	3038.8	3116.1	3122.1	3128.2	3013.0
CH stretch all sym	3038.5	3117.3	3123.6	3130.2	3013.5
CH stretch all asym	3112.0	3193.7	3203.4	3211.3	
CH stretch asym (CH_2 sym)	3127.3	3208.5	3217.9	3225.9	3088.0

Table 8-A5. Calculated Frequencies (in cm^{-1}) of the C_2H_4 + S Transition State

Assignment	BLYP Basis 1	B3LYP Basis 1	B3PW91 Basis 1	B3PW91 Basis 2
CS stretch	191.6*i*	255.2*i*	139.6*i*	163.4
CCS bend	192.6	198.8	160.6	167.6
CH_2 sym twist	353.6	361.9	335.1	343.0
CH_2 sym rock	792.3	812.3	816.1	814.1
CH_2 asym wag	853.6	885.4	927.1	911.2
CH_2 sym wag	939.5	966.2	965.5	957.7
CH_2 asym twist	922.1	960.6	989.6	983.0
CH_2 asym rock	1204.3	1235.8	1228.1	1226.4
CH_2 sym scissors	1249.8	1280.3	1324.8	1313.7
CH_2 asym scissors	1437.4	1471.8	1462.5	1463.3
CC stretch	1521.5	1563.5	1595.0	1587.7
CH stretch sym (CH_2 asym)	3062.5	3139.0	3145.1	3146.2
CH stretch all sym	3070.8	3146.4	3154.2	3154.5
CH stretch all asym	3124.6	3205.4	3220.4	3222.1
CH stretch asym (CH_2 sym)	3162.7	3241.9	3250.6	3253.0

Chapter Nine
Conclusions

9.1 Metal-Alkyne Chemistry

The study of the phosphine substitution reaction of $W(CO)_5$(BTMSA) revealed that the labilizing effect of the alkyne ligand, initially observed for group 8 $M(CO)_4(\eta^2$-alkyne) (M = Fe, Ru, Os) compounds[1], extends to group 6 metals as well. The product of the reaction is $W(CO)_4(PMe_3)$(BTMSA), the CO dissociated species. However, the compound is not as thermally stable as the analogous osmium derivative, $Os(CO)_3(PMe_3)$(BTMSA). Subsequent phosphine substitution results in loss of the alkyne ligand, presumably due to a combination of the effects of $4e^-$ destabilization and steric factors. The phosphine substitution in $Os(CO)_4$(BTMSA) is analogous to previous cases. Qualitatively, the substitution of a second PMe_3 ligand is slower than the first. There is no evidence for CO insertion into the metal-alkyne bond, which was observed with the other electron rich alkynes[2]. $Os(CO)_4$(BTMSA) is less reactive than other $Os(CO)_4$(alkyne) complexes, another indication that steric effects are also important in determining the effectiveness of alkyne ligands on CO labilization.

Theoretical investigation of the metal-alkyne interaction in $Os(CO)_4$(alkyne) and $W(CO)_5$(alkyne) complexes shows the ability of the alkyne to stabilize the CO dissociated product via four-electron donation. The calculated geometry of the intermediate [$W(CO)_4$(alkyne)] is trigonal-bipyramidal with the alkyne lying perpendicular to the equatorial plane, a geometry conducive for the alkyne to donate from both of its π sets of orbitals[3]. Extended Hückel fragment molecular orbital analysis on the osmium and tungsten HFB and butyne complexes is consistent with the nature of the two alkynes; π-back donation is stronger with the more π-acidic HFB ligand.

Kinetic analysis on the reaction of $Ru(CO)_4(HFB)$ with $Os(CO)_5$, $Cp^*M(CO)_2$ (M = Rh, Ir) shows that the reactivity sequence is Rh >> Ir > Os. However, the rate determining step with $Cp^*Rh(CO)_2$ appears to be different from that of the remaining complexes. With $Os(CO)_5$ and $Cp^*Ir(CO)_2$, there is an equilibration step causing intermolecular exchange of CO with $Ru(CO)_4(HFB)$, with bimetallic product formation being rate limiting. Labeling experiments corroborated this. Reaction between $Ru(^{13}CO)_4(HFB)$ and $Os(CO)_5$ was seen to occur by enrichment of $Os(CO)_5$ prior to product formation[4] (see Scheme 4-4 in Chapter Four). The much faster reaction with $Cp^*Rh(CO)_2$ could be due to the greater propensity of rhodium (second row transition metal) for bridging carbonyl formation, promoting HFB migration. To resolve this question, it is proposed that ^{13}CO labeling experiments be carried out between $Ru(^{13}CO)_4(HFB)$ and $Cp^*M(CO)_2$ (M = Rh, Ir).

The proposed intermediate in the condensation reaction of $Ru(CO)_4(HFB)$ with $Os(CO)_5$ was studied with Density Functional Theory. From preliminary work the proposed mechanism does appear to be viable. However, due to limitations in computing power, optimized geometries were unattainable and the study had to be postponed.

9.2 Isotope Effects

Equilibrium isotope effects were calculated for the bromination of both cyclohexene[5] and ethylene[6]. A breakdown of the inverse effect observed in the cyclohexene system into individual mode contributions was difficult due to the complexity of the vibrations. Thus, a single mode was not uncovered as the source of the inverse EIE. From the calculated geometries, the hybridization at the olefinic carbon does not deviate from sp^2 upon addition of Br^+ (sum of the angles around carbon is 356° versus 360° for ideal sp^2). On the basis of calculations, it was not possible to distinguish between the models of Streitwieser[7] and Strausz[8].

In the smaller system of $C_2H_4 + Br^+$, the vibrational analysis was less complicated and individual mode contributions to the isotope effect were calculated. Just as in the $Os_2(CO)_8 + C_2H_4$ system studied by Bender[9], there is a single mode responsible for the inverse EIE which is the CH_2 symmetric twist, created upon bromine addition. This indicates that the Strausz model is applicable to these systems and since the new mode responsible for the inverse EIE is the same in both cases, it is reasonable to expect similar findings in other ethylene addition/complexation reactions. Both in the case of $C_6H_{10} + Br^+$ and in $C_2H_4 + Br^+$, it would be worthwhile to study the role of the solvent effects.

The reinvestigation of the addition of sulfur to ethylene verifies Strausz's original calculations[8] and shows that the transition state for the reaction is indeed asymmetrical. While the agreement with experiment is poor compared to that found in the bromination reactions, calculations do provide a qualitative understanding of the origin of the isotope effect. As with the bromination of ethylene, the origin of the inverse isotope effect in the addition of sulfur and selenium to ethylene is the CH_2 symmetric twist. Better agreement with experiment could be realized with dynamic tunnelling corrections.

9.3 References

1. Pearson, J.; Cooke, J.; Takats, J.; Jordan, R. B. *J. Am. Chem. Soc.* **1998**, *120*, 1434.

2. Mao, T.-F. PhD. Thesis, University of Alberta, 1996.

3. Wink, D. J.; Creagan, B. T. *J. Am. Chem. Soc.* **1990**, *112*, 8585.

4. Gagné, M. R.; Takats, J. *Organometal.* **1988**, 7, **561.**

5. Slebocka-Tilk, H.; Neverov, A.; Motallebi, S.; Brown, R. S.; Donini, O.; Gainsforth, J. L.; Klobukowski, M. *J. Am. Chem. Soc.* **1998**, *120*, 2578.

6. Koerner, T.; Brown, R. S.; Gainsforth, J. L.; Klobukowski, M. *J. Am. Chem. Soc.* **1998**, *120*, 5628.

7. Streitwieser, A., Jr.; Jagow, R. H.; Fahey, R. C.; Suzuki, S. *J. Am. Chem. Soc.* **1958**, *80*, 2326.

8. (a)Strausz, O. P.; Safarik, I.; O'Callaghan, W. B.; Gunning, H. E. *J. Am. Chem. Soc.* **1972**, *94*, 1828. (b) Safarik, I.; Strausz, O. P. *J. Phys. Chem.* **1972**, *76*, 3613.

9. Bender, R. B. *J. Am. Chem. Soc.***1995**, *117*, 11239.